Development of advanced technologies for enhancing obstacle-negotiation capabilities in mobile robots

Original Citation:
Development of advanced technologies for enhancing obstacle-negotiation capabilities in mobile robots / Pappalettera, Antonio. - ELETTRONICO. - (2025).

Publisher: Politecnico di Bari

DEPARTMENT OF MECHANICS, MATHEMATICS AND MANAGEMENT

MECHANICAL AND MANAGEMENT ENGINEERING
PH.D. PROGRAM

SSD: ING-IND/13 - APPLIED MECHANICS

Final dissertation

Development of Advanced Technologies for Enhancing Obstacle-Negotiation Capabilities in Mobile Robots

---

Antonio PAPPALETTERA

Supervisors:

Prof. Giacomo MANTRIOTA

Prof. Giulio REINA

Prof. Francesco BOTTIGLIONE

Coordinator of the PhD Program:
Prof. Giuseppe CASALINO

Course XXXVII, 01/11/2021 - 01/11/2024

La ricerca è stata realizzata con il cofinanziamento dell'Unione europea - **POC Puglia 2014-2020 – Asse X - Azione 10.4 "Interventi volti a promuovere la ricerca e per l'istruzione universitaria". Approvazione Avviso pubblico n. 1/POC/2021 "Dottorati di ricerca in Puglia XXXVII Ciclo"**.

LIBERATORIA PER L'ARCHIVIAZIONE DELLA TESI DI DOTTORATO

Al Magnifico Rettore
del Politecnico di Bari

Il/la sottoscritto/a Antonio Pappalettera nato/a a Trani il 02-07-1994

residente a Trani in via Marsala 43 e-mail antonio.pappalettera@poliba.it

iscritto al 3° anno di Corso di Dottorato di Ricerca in Ingegneria Meccanica e Gestionale ciclo 37°

ed essendo stato ammesso a sostenere l'esame finale con la prevista discussione della tesi dal titolo:

Development of Advanced Technologies for Enhancing Obstacle-Negotiation Capabilities in Mobile Robots

DICHIARA

1) di essere consapevole che, ai sensi del D.P.R. n. 445 del 28.12.2000, le dichiarazioni mendaci, la falsità negli atti e l'uso di atti falsi sono puniti ai sensi del codice penale e delle Leggi speciali in materia, e che nel caso ricorressero dette ipotesi, decade fin dall'inizio e senza necessità di nessuna formalità dai benefici conseguenti al provvedimento emanato sulla base di tali dichiarazioni;
2) di essere iscritto al Corso di Dottorato di ricerca Ingegneria Meccanica e Gestionale ciclo 37°, corso attivato ai sensi del "*Regolamento dei Corsi di Dottorato di ricerca del Politecnico di Bari*", emanato con D.R. n.286 del 01.07.2013;
3) di essere pienamente a conoscenza delle disposizioni contenute nel predetto Regolamento in merito alla procedura di deposito, pubblicazione e autoarchiviazione della tesi di dottorato nell'Archivio Istituzionale ad accesso aperto alla letteratura scientifica;
4) di essere consapevole che attraverso l'autoarchiviazione delle tesi nell'Archivio Istituzionale ad accesso aperto alla letteratura scientifica del Politecnico di Bari (IRIS-POLIBA), l'Ateneo archivierà e renderà consultabile in rete (nel rispetto della Policy di Ateneo di cui al D.R. 642 del 13.11.2015) il testo completo della tesi di dottorato, fatta salva la possibilità di sottoscrizione di apposite licenze per le relative condizioni di utilizzo (di cui al sito http://www.creativecommons.it/Licenze), e fatte salve, altresì, le eventuali esigenze di "embargo", legate a strette considerazioni sulla tutelabilità e sfruttamento industriale/commerciale dei contenuti della tesi, da rappresentarsi mediante compilazione e sottoscrizione del modulo in calce (Richiesta di embargo);
5) che la tesi da depositare in IRIS-POLIBA, in formato digitale (PDF/A) sarà del tutto identica a quelle **consegnate**/inviate/da inviarsi ai componenti della commissione per l'esame finale e a qualsiasi altra copia depositata presso gli Uffici del Politecnico di Bari in forma cartacea o digitale, ovvero a quella da discutere in sede di esame finale, a quella da depositare, a cura dell'Ateneo, presso le Biblioteche Nazionali Centrali di Roma e Firenze e presso tutti gli Uffici competenti per legge al momento del deposito stesso, e che di conseguenza va esclusa qualsiasi responsabilità del Politecnico di Bari per quanto riguarda eventuali errori, imprecisioni o omissioni nei contenuti della tesi;
6) che il contenuto e l'organizzazione della tesi è opera originale realizzata dal sottoscritto e non compromette in alcun modo i diritti di terzi, ivi compresi quelli relativi alla sicurezza dei dati personali; che pertanto il Politecnico di Bari ed i suoi funzionari sono in ogni caso esenti da responsabilità di qualsivoglia natura: civile, amministrativa e penale e saranno dal sottoscritto tenuti indenni da qualsiasi richiesta o rivendicazione da parte di terzi;
7) che il contenuto della tesi non infrange in alcun modo il diritto d'Autore né gli obblighi connessi alla salvaguardia di diritti morali od economici di altri autori o di altri aventi diritto, sia per testi, immagini, foto, tabelle, o altre parti di cui la tesi è composta.

Luogo e data Bari, 1-11-2024 Firma Antonio Pappalettera

Il/La sottoscritto, con l'autoarchiviazione della propria tesi di dottorato nell'Archivio Istituzionale ad accesso aperto del Politecnico di Bari (POLIBA-IRIS), pur mantenendo su di essa tutti i diritti d'autore, morali ed economici, ai sensi della normativa vigente (Legge 633/1941 e ss.mm.ii.),

CONCEDE

- al Politecnico di Bari il permesso di trasferire l'opera su qualsiasi supporto e di convertirla in qualsiasi formato al fine di una corretta conservazione nel tempo. Il Politecnico di Bari garantisce che non verrà effettuata alcuna modifica al contenuto e alla struttura dell'opera.
- al Politecnico di Bari la possibilità di riprodurre l'opera in più di una copia per fini di sicurezza, back-up e conservazione.

Luogo e data Bari, 1-11-2024 Firma Antonio Pappalettera

Unione europea
Fondo sociale europeo

REGIONE PUGLIA

PUGLIA FESR·FSE 2014/2020
Il futuro alla portata di tutti

Politecnico di Bari

Department of Mechanics, Mathematics and Management
MECHANICAL AND MANAGEMENT ENGINEERING
Ph.D. Program
SSD: ING-IND/13–APPLIED MECHANICS

Final Dissertation

Development of Advanced Technologies for Enhancing Obstacle-Negotiation Capabilities in Mobile Robots

---

by

Antonio PAPPALETTERA

Antonio Pappalettera

Supervisors:

Prof. Giacomo MANTRIOTA

Prof. Giulio REINA

Giulio Reina

Prof. Francesco BOTTIGLIONE

Referees:

Prof. Giovanni BOSCHETTI

Prof. Luca BRUZZONE

Coordinator of PhD Program:

Prof. Giuseppe CASALINO

Course XXXVII, 01/11/2021 - 01/11/2024

Abstract

Obstacle negotiation is one of the major challenges for mobile robots, particularly in environments where they must operate on uneven terrain or encounter physical barriers such as stairs, debris, or rough ground. Practical applications for such robots range from humanitarian assistance to logistics and inspection of hazardous or hard-to-reach environments. Although various technological approaches have been developed and successfully implemented, there is still a need to enhance robots' ability to adapt to a wide range of complex obstacles, ensuring greater operational efficiency and safety.

This thesis focuses on the analysis and development of innovative technologies to improve robots' ability to overcome different types of obstacles. The primary goal is to enhance the robots' capability to operate in challenging environments and ensure smooth and safe movement even in the presence of physical barriers, thus contributing to the advancement of mobile robotics.

The first part of the thesis presents a systematic review of the scientific and engineering literature on stair-climbing mechanisms is given. It provides concise descriptions of the mechanisms and operating methods, highlighting the advantages and disadvantages of various climbing platforms. To quantitatively assess system performance, several metrics are introduced. Using these metrics, it becomes possible to compare vehicles with different locomotion modes and characteristics, offering researchers and practitioners valuable insights into stair-climbing vehicles and enabling them to select the most suitable platform for transporting people and heavy loads up staircases.

The second part of the thesis aims to propose a rigorous analysis approach to study what happens when different kind of rubber belts or tires are in contact with a corner edge and what forces are exchanged between these two elements. A general introduction is given by mainly focusing on the scientific literature lack of a comprehensive wheel-obstacle contact model for the step-climbing problem. Then the importance of considering tire deformation has been emphasised and a novel approach to wheel-obstacle contact mechanics is given. A description of the test bench specifically developed for this work is provided along the experimental results for two cases of flat belt and tire patch.

The third part of the thesis presents experimental results on the behavior of a conventional pneumatic tire clearing a step-obstacle, alongside an analytical model developed to analyze the interaction between a deformable tire and the corner edge of a step-obstacle.

Finally, the "XXbot" concept is developed. The thesis proposes a specialized model that predicts how the system will move based on the terrain profile. Stair-climbing simulations were then performed using multibody simulation software MSC-Adams, and the results are presented to demonstrate the effectiveness of the proposed vehicle. The findings indicate that the robot can be adapted for various applications, such as stair-climbing wheelchair platforms.

Keywords: Stair-climbing vehicles, Mobile robotics, Step-obstacle negotiation, Rubber belts, Pneumatic tire, Wheels.

Contents

List of Figures

List of Tables

Introduction

In the era of drones and artificial intelligence, is it still relevant to discuss mobile robots? If you are reading this thesis, then probably yes. Mobile robots have come to embody a broad vision within modern engineering, where machines traverse complex environments autonomously, perform essential tasks, and even partner with humans in ways previously unimaginable. Despite the explosive growth of drones and AI-driven systems, mobile robots—particularly ground-based systems—have a unique role, filling gaps that aerial and digital counterparts cannot. This distinction drives the development of mobile robots, especially those capable of overcoming obstacles, ensuring stability, and negotiating uneven terrains, thus broadening their applications from confined industrial spaces to vast open terrains.

The advancement of mobile robots has surged in response to diverse applications: humanitarian aid, military logistics, infrastructure inspection, agricultural field and natural disaster response. However, each environment poses specific challenges, especially when robots must cross obstacles like steps, rubble, or irregular terrain. This is where obstacle-negotiation capabilities play a crucial role, demanding a continuous evolution in mobile robot design. Whether used in rescue missions or construction sites, such robots must operate reliably midst unpredictably harsh conditions, which requires robust mechanical structures, adaptive locomotion systems, and sophisticated control algorithms.

This thesis presents an innovative approach to mobile robot design, focusing on wheeled and tracked vehicles obstacle-negotiation capabilities. In fact, as we progress into an era that demands more versatile and resilient robots, this thesis positions mobile robotics as a vital field. The contributions presented here seek to inspire future research and innovations, paving the way for mobile robots that are truly prepared for the challenges of the modern world.

Chapter 1

Stair-climbing vehicles

1.1 Introduction

The number of people affected by any form of physical disability represents a significant part of the world population, from children to adults alike. It is estimated that approximately 131 million or 1.85 percent of people require wheelchairs in the world [1]. Almost 1 percent of United States population currently uses a wheelchair. Half of them must overcome steps to enter and exit their homes. A similar fraction report having difficulty entering or leaving the home [2]. In any case, there are also people without disabilities to consider. According to the National Center for Health Statistics (Hyattsville, MD, USA), only in the USA, the percent of adults aged 18 and over with any difficulty walking or climbing steps in 2020 is 18.0 percent, almost 60 million of people [3]. Despite that, the worldwide number of people who find it difficult to overcome architectural barriers daily has not yet been estimated. Because the world population is aging, the people mobility problems are of increasing importance. In Italy, many multi-story residential buildings are not accessible by people with disabilities or walking problems because in them there is no elevator (or similar) for connection to the upper floors. The situation in schools is no better. The ISTAT (The Italian National Institute of Statistics) sources reveal that only 32 percent of them are barrier-free. In 63 percent of cases, the reason for the lack of accessibility is the lack of an elevator or the presence of a lift that is not suitable for the transport of people with motor disabilities [4].

Ground vehicles can help to solve these problems [5, 6]. They face many challenges, including the negotiation of obstacles, stairs, and uneven terrain. Recently, much attention has been attracted by solutions that allow to overcome a series of steps towards stair-climbing platforms [7].

1.2 Categorization of stair-climbing vehicles

Many example of stair-climbing vehicles have been proposed and demonstrated. They can be divided into broad categories according to the scheme shown in Figure

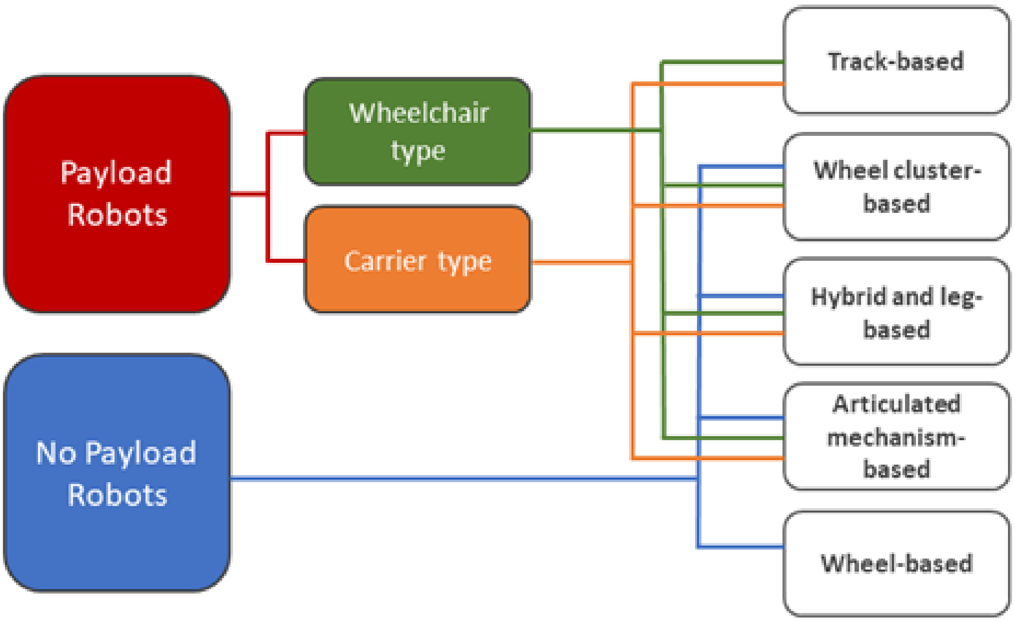

Figure 1.1: Categorization chart for stair-climbing vehicles

One of the main aspects to consider is whether the robot is designed to carry a payload. Therefore, the first main classification can be made by differentiating “payload robots” from “no payload robots”. In this classification, we consider payload may be people, animals or goods that should be carried safely by the robot through a desired path. On the contrary, equipment attached to the robot and not directly involved in the motion ability, such as additional sensors and cameras, robotic arms and tools, are not considered as payload but rather part of the robots itself. Payload robots can be further divided into wheelchair and carrier type. Wheelchair types are systems in which a wheelchair for the transport of a person is used. In carrier types, a container is used instead to allocate goods. ally, wheelchair type, carrier type and no payload robots can be divided according to the stair-climbing mechanism used. These mechanisms belong to five main categories: track-based, wheel cluster-based, articulated mechanism-based, hybrid and leg-based and wheel-based systems.

- **Track-based mechanisms** have the largest ground contact surface and are very stable due to a lower center of gravity. To facilitate the stair-climbing process, tracks can be equipped with teeth. Track-based mechanisms enable robots to climb up or down the stairs at a constant speed in a stable manner due to the interlocking effect between the track’s outer teeth and the steps’ sharp corner. There are no problems regarding the different length of rise, run, tread and noising of the stair steps’ shape. The track-based mechanisms are widely adopted.

- **Wheel cluster-based mechanisms:** A wheel cluster is a component with multiple wheels uniformly distributed in the same plane around a common center. While using a stair-climbing mechanism, the wheels rotate around the central axis of the wheel cluster and propel the robot up or down the stairs. Often, wheel cluster-based mechanism robots are not able to overcome all type of stair, so a range of available step lengths are given. Wheel cluster-based robots are characterized by speed fluctuation during the ascending and descending motion.

- **Articulated mechanism-based systems:** This type of stair-climbing robots uses an articulated mechanism in combination with wheels to accomplish the stair-climbing task.

- **Hybrid and leg-based mechanisms:** This type of stair-climbing mechanism originates from the imitation of humans' and animals' stair-climbing techniques, using legs and feet to walk on various steps. Theoretically they can adapt to all type of stairs provided that the control system is sufficiently developed.

- **Wheel-based mechanisms:**Two or more wheels are used to perform the stair-climbing task. They can be suspended respect to the robot's frame, using mechanical suspension, or not. Wheeled robots can reach high speeds with low power consumption.

1.2.1 Payload Robots

These types of vehicles are designed to carry a load during staircase negotiation. They can be divided into wheelchair type (please refer to Figure 1.2a), where the person transported is seen as a payload, or carrier type (see Figure 1.2b). Both families are described in detail in the remainder of this section.

Wheelchair Type Robots

Since the 1990s, many research results on wheelchair-type stair climbing robots have been achieved and a variety of commercial wheelchairs and prototypes have been developed [10]. Many examples of wheelchair-type stairs have been demonstrated at Cybathlon [11]. Cybathlon is a non-profit project of ETH Zurich (Zurich, Germany) who acts as a platform that challenges teams from all over the world to develop assistive technologies suitable for everyday use with and for people with disabilities. Different disciplines comprise the competitions. They apply the most modern powered devices such as prostheses, wearable exoskeletons, wheelchairs and functional electrical stimulation, as well as novel brain-computer interfaces to remove barriers between the public, people with disabilities and science. In the Powered wheelchair race competition, the most modern solutions compete with each other. Among the different tasks there is precisely that of overcoming a small series of steps.

Some examples of wheelchair type robots are now presented using classification shown in Figure1.1. Track-based robots are reported in Table 1.2.1. Most of the

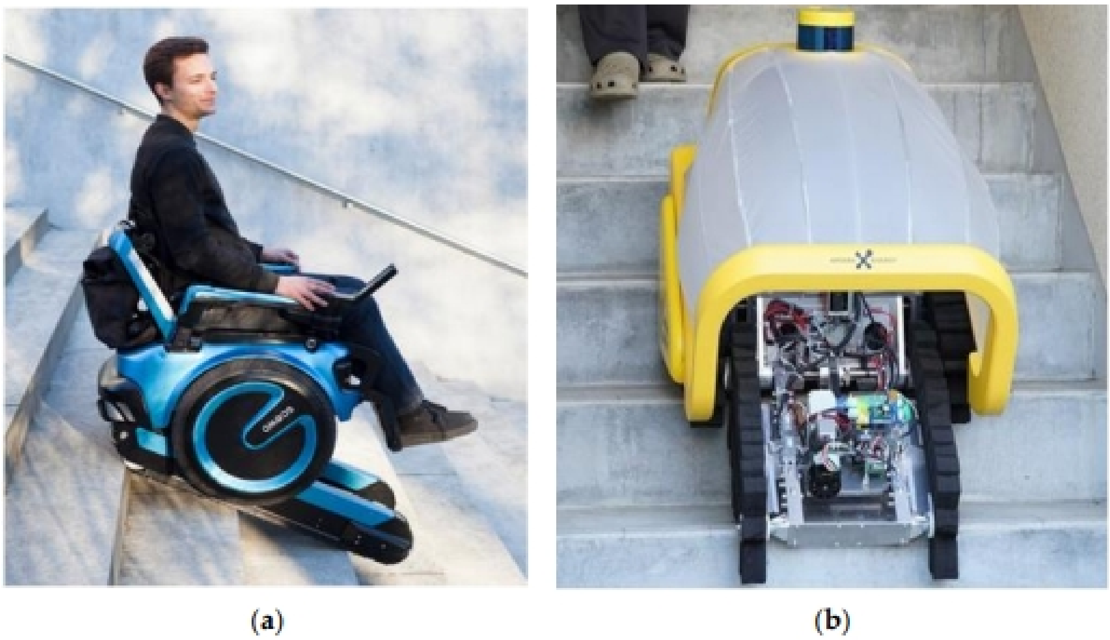

Figure 1.2: (a) Scewo wheelchair in action. Adapted with permission from ref. [8]. 2023 Preeta Chatterjee 24 September 2021; (b) Amoeba Go-1 in action [9].

solutions [8,12–15] use wheels as preferred locomotion mode on regular flat ground while the track-based system is stowed under the carriage. Obstacle negotiation is performed in track locomotion mode: the position of the tracks is changed so that they are lowered to the ground while wheels detach from the ground. Instead, in [16, 17] a reconfigurable track-based system is proposed to prepare the robot to negotiate stairs: in WT-Wheelchair internal linkages, positions are changed while front and rear flipper angulation are used in B-Free Ranger and Fortissimo. The wheelchair-type robots that participated in the Cybathlon are: Scewo Bro [8], B-Free Ranger [17], ZED evolution [18], Caterwil GTS5 Lux [19], Fortissimo [14], Hkust [14], All-Terrain Wheelchair [15].

The wheel cluster robots are reported in Table 1.2.1. Each solution has very different features from others. iBOT 4000 [21] has inverted pendulum-type dynamic stability control to go up and down stairs while holding the seat stable. Wheelchair.q [22] is composed of a pair of locomotion units and a retractable track that guarantees the rear support point. Finally, Castillo [23], uses four X-shaped wheels to climb and descend stairs while the seat angle of the wheelchair can be changed to hold the center of gravity close to the center of the supporting polygon.

Table 1.1: Track-based wheelchair type robots list.

Name	Solution	Features
Scewo Bro [8]		Commercial solution, automatic stair-climbing system, self-balancing software control, high safety
TopChair-S [12]		Commercial solution, automatic stair-climbing system, self-balancing software control
WT Wheelchair [16, 20]		Prototype solution, manual stair-climbing system, no self-balancing control system
Tao [13]		Prototype solution, manual stair-climbing system, self-balancing software control
B-Free Ranger [17]		Commercial solution, automatic stair-climbing system, self-balancing software control
ZED evolution [18]		Prototype solution, manual stair-climbing system, no self-balancing control system
Caterwil GTS5 Lux [19]		Commercial solution, automatic stair-climbing system, self-balancing software control, high speed
Fortissimo [14]		Prototype solution, manual stair-climbing system, no self-balancing control system
Hkust [14]		Prototype solution, manual control, no self-balancing control system
All-Terrain Wheelchair [15]. Adapted with permission ref. [15] 2017 Janez Podobnik		Prototype solution, automatic stair-climbing system, self-balancing software control, Chebyshev-based linkage mechanism for lifting and lowering the tracks

Table 1.2: Wheel cluster-based wheelchair type robots list.

Name	Solution	Features
iBOT 4000 [21,24]		Commercial solution, automatic stair-climbing system, self-balancing software control, good driving range
Wheelchair.q [22,25]. Adapted with permission from ref. [22] 2017 Giuseppe Quaglia, Matteo Nisi	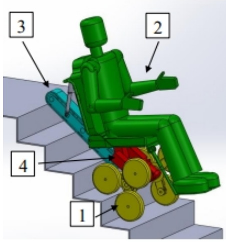	Prototype solution, manual control, no self-balancing control system, good performance
Castillo [23]. Adapted with permission from ref. [23] 2017 Basilio Dobras Castillo	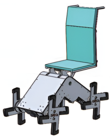	Prototype solution, manual control, self-balancing control system, low comfort

Hybrid and leg-based robots are reported in Table 1.2.1. Wang [26] and Zero Carrier [27,28] have chain-driven legs that move vertically and wheels at the end of each leg. Some are driven to provide forward locomotion while other are passive wheels. Lee wheelchair [29] (not shown in Table1.3) climbs stairs using the two 3-DOF legs with boomerang-shaped feet. The leg mechanisms are folded into the compact wheelchair body when the wheelchair moves over flat surfaces. JWCR-1 [30,31] and WL-16 II [32] simulate humanoid walking to going up and down stairs. The first uses 12-DOF mechanism to replicate a human leg while the second has 6-DOF parallel mechanism for each leg.

Articulated Mechanism-based robots are reported in Table 1.2.1. In general, they use a wheel or wheels mounted on a structure whose position changes during stair climbing. Chen [34] and TBW-I [35] use simple rotation to change the shape of the mechanism, Morales [36] and Lawn [37] use deployable rigid supports to lift the device and a secondary mechanism to place the wheels on the new support surface. Finally, RT-Mover PType WA [38] has two leg-like axle mechanism and a seat slider. Four wheels are mounted at the leg tips. Every leg-like mechanism possesses two shafts: one for roll adjustments and one for steering adjustment. RT-Mover PType WA wheelchair type robot participates at the 2020 Cybathlon edition.

Table 1.3: Hybrid and leg-based wheelchair type robots list.

Name	Solution	Features
Wang [26]. Adapted with permission from ref [26] 2014 Hongbo Wang	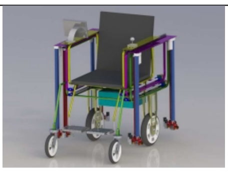	Prototype solution, manual stair-climbing system
Zero Carrier [27,28]. Adapted with permission from ref. [27] 2004 Jianjun Yuan	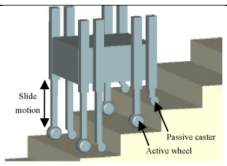	Prototype solution, automatic stair-climbing system, low speed
JWCR-1 [30,31]. Adapted with permission from ref. [31] 2007 Jiaoyan Tang		Prototype solution, manual control, low safety
WL-16 II [32,33]. Adapted with permission from ref. [32] 2006 Y. Sugahara		Prototype solution, manual control

Carrier Type Robots

One goal of robotics is to replace human operators in daily tasks. Mobile robots for goods delivery represent an important application area. The challenge that these robots must face is to climb a flight of stairs (up and down) of a building carrying a load. With reference to the classification proposed in Figure1.1, examples of carrier-type stair-climbing vehicles will be introduced and discussed.

Track-based carrier robots are reported in Table 1.2.1.

Yoneda [42] and Helios-VI [43] use traditional track solution. Solutions that adopt a reconfigurable track system with flippers are TAQT Carrier [44], Haulerbot [45] and iRobot 710 Kobra [46]. Amoeba Go-1 [9] does not use a traditional track, while it is equipped with a pair of soft crawlers in place of a classic track with grousers. Finally, Polibot [47] refers to an example of suspended tracked robot where the ground wheels can move with respect to the chassis using independent swing arms, showing remarkable mobility over challenging environments that include staircases.

Table 1.4: Articulated mechanism-based wheelchair type robots list.

Name	Solution	Features
RT-Mover PType WA [38–40]		Prototype solution, automatic stair-climbing system, self-balancing software control
Morales [36]	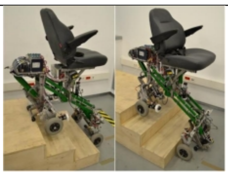	Prototype solution, automatic stair-climbing system, self-balancing software control, low speed
Lawn [37]. Adapted with permission from ref. [37] 2003 M.J. Lawn	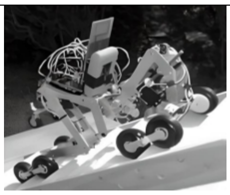	Prototype solution, automatic stair-climbing system, self-balancing software control
TBW-I [35]. Adapted with permission from ref. [35] 2010 Yusuke Sugahara		Prototype solution, manual control, no self-balancing control system
HELIOS-V [41]. Adapted with permission from ref. [41] 1999 Y. Uchida		Prototype solution, manual control, no self-balancing control system
Chen [34]. Adapted with permission from ref. [34] 2012 Chun-Ta Chen, Hoang-Vuong Pham		Prototype solution, manual control, no self-balancing control system, low stability

A wheel cluster-based carrier type robot is reported in Table 1.2.1. Deshmukh [48] has four wheel-cluster units to perform the stair climbing task. To hold the payload horizontally, a simple mechanism is used to raise and lower the platform.

Table 1.5: Track-based carrier type robots list.

Name	Solution	Features
Amoeba Go-1 [9]		Commercial solution, autonomous driving, self-balancing control system soft rubber tracks
Yoneda [42]	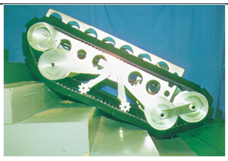	Prototype solution, manual control, no self-balancing control system
TAQT Carrier [44]. Adapted with permission from ref. [44] 1992 S. Hirose		Prototype solution, manual control, self-balancing system
HELIOS-VI [43]		Prototype solution, manual control, no self-balancing control system
Haulerbot [45]		Commercial solution, autonomous driving self-balancing control system high payload capacity
iRobot 710 Kobra [46]		Commercial solution, autonomous driving, self-balancing control system
Polibot [47]		Prototype solution, manual control, no self-balancing control system

Hybrid and leg-based carrier type robots are reported in Table 1.2.1. Wen [49] has driven legs which move vertically, and four wheels attached to the body frames. Finally, Peopler-II [50, 51] has perpendicularly oriented planetary legged wheels that are used to climb and descend stairs.

Table 1.6: Wheel cluster-based carrier type robots list.

Name	Solution	Features
Deshmukh [48]		Prototype solution, manual control, self-balancing control system

Table 1.7: Hybrid and leg-based carrier type robots list.

Name	Solution	Features
Wen [49]		Prototype solution, autonomous driving, automatic stair-climbing system
PEOPLER-II [50, 51]		Prototype solution, autonomous driving, no self-balancing control system

1.2.2 No Payload Robots

This type of robot has been designed without foreseeing any payload capacity. They usually employ less complicated systems to perform the ascent and descent of the flight of stairs. Referring to Fig.1.1, no payload robots can be categorized based on the specific climbing mechanism too. AZIMUT [52], shown in Fig. 1.3 and Krys [53], shown in Fig. 1.4, are example of no payload robots. Since in the following we will focus only on payload robots, a complete list of this type of robot is not given as it is outside the scope of this paper. A comprehensive discussion can be found in Pappalettera et al. [54].

1.3 Analysis and Comparison

In this section, various performance metrics are presented that consider allowable payload, maximum climbing speed, maximum crossable slope, transport ability and their combinations. By referring to these metrics, it is possible to compare vehicles with different locomotion modes and properties, highlighting the advantages and disadvantages of each. In the following we will refer to the Payload robots shown in the section 1.2.1.

1.3.1 Performance Metrics

Various metrics, suggested by Binnard [55], are introduced to quantitatively evaluate the performance of a given stair-climbing vehicle. Special attention has been

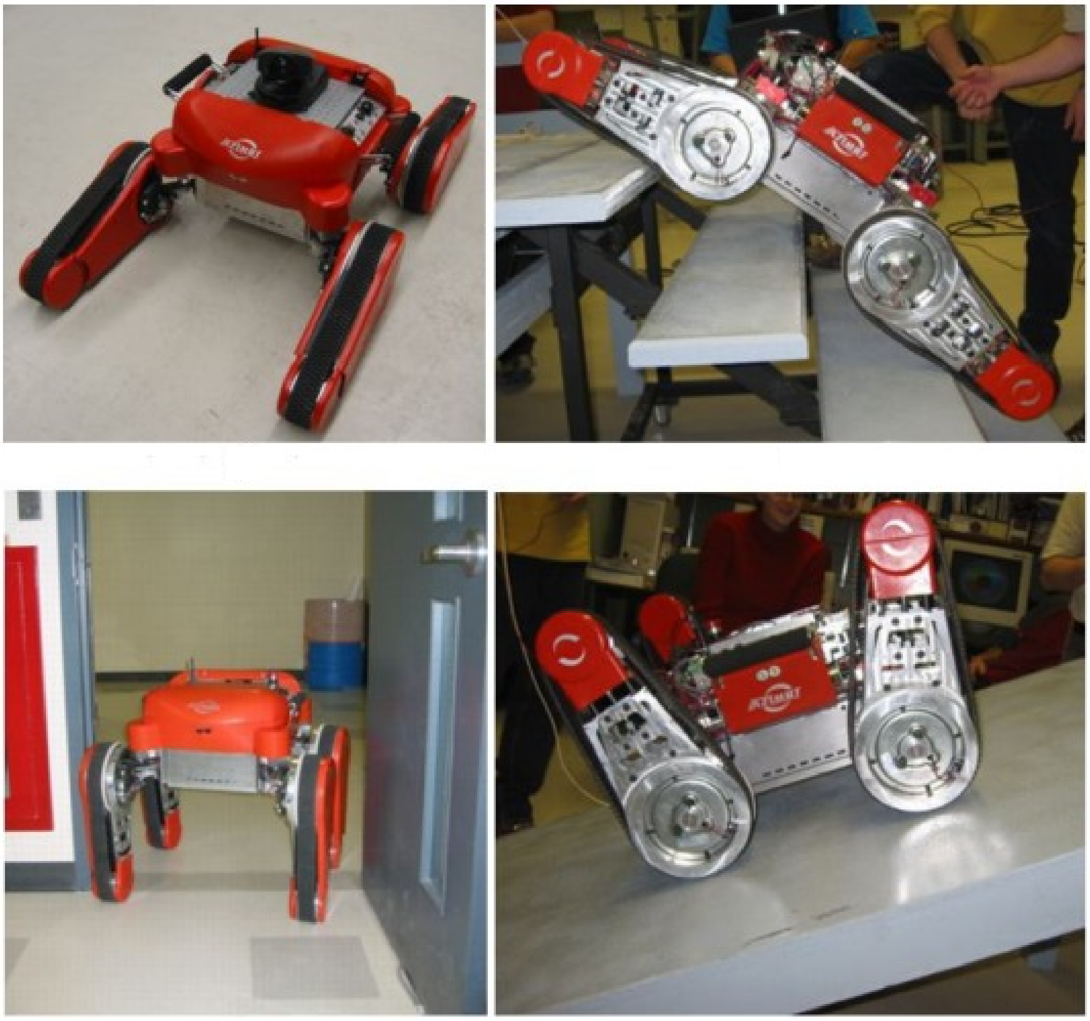

Figure 1.3: Azimut [52]. Adapted with permission from ref. [52] 2003 F.Michaud

given to the normalization of the metrics allowing heterogeneous platforms to be fairly compared. Metrics were estimated based on the specifications stated in related scientific papers or technical sheets. Where data are not available, corresponding metrics are not calculated.

The first performance metric is the payload capacity, PC, defined as the percentage ratio of the maximum payload mass to the robot mass:

$$PC = \frac{\text{payload mass}}{\text{robot net mass}} \times 100 \tag{1.1}$$

As a second metric, the normalized speed, NS, can be defined as the ratio of the robot maximum climbing speed to the robot body length.

$$NS = \frac{\text{Maximun Speed}}{\text{Body length}} \tag{1.2}$$

As an overall performance metric, the Normalized Work Capability, NWC, can

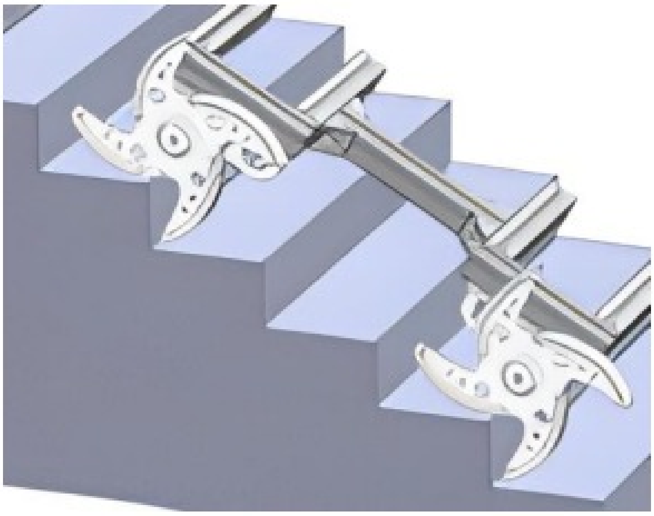

Figure 1.4: Krys stair climbing robot in action [53].

be considered. It is suggested by Binnard [55] and it is defined as the product of the Normalized Speed (NS) and Payload Capacity (PC).

$$NWC = PC \times NS \tag{1.3}$$

Figure 1.5 shows a bar chart where the Normalized Work Capability is estimated for the wheelchair type vehicles presented in Sections 1.2.1. Details can be found in the Appendix A where the numeric value of PC, NS and NWC are provided for each platform. Red refers to track-based, blue to wheel cluster-based, green to hybrid and leg-based and yellow to articulated mechanism-based robots. It can be said that NWC quantifies the robot general performance, as it considers both the ability to carry payload and the climbing speed. As seen from the bar charts, the NWC metric well defines the different robot categories: track-based, wheel cluster-based, hybrid and leg-based and articulated mechanism-based. In fact, each category has a characteristic range of NWC. Articulated mechanism-based robots are mainly concentrated in the range of values that varies between 0 and $3\,[\,\mathrm{s}^{-1}]$. Even legged robots have low NWC values, ranging between 0 and $5\,[\,\mathrm{s}^{-1}]$. Wheel cluster-based robots have high NWC values and are mostly concentrated in the range between 5 and $15\,[\,\mathrm{s}^{-1}]$. Finally, the track-based stair-climbing robots are distributed evenly over the entire range of NWC values, where the most recent robots have NWC values ranging from 6 to $18\,[\,\mathrm{s}^{-1}]$. The NWC of carrier type robots is presented in Fig. 1.6.

Normalized Work Capability is not the only metric to measure the performance of payload stair-climbing robots. To evaluate the versatility of use of one robot compared to another, the maximum crossable step height and stair slope are also used as performance metrics. Maximum crossable step height and stair slope are reported in Appendix A for each existing vehicle. A graphical representation of the maximum crossable height and slope is given below. Figure 1.7 refers to

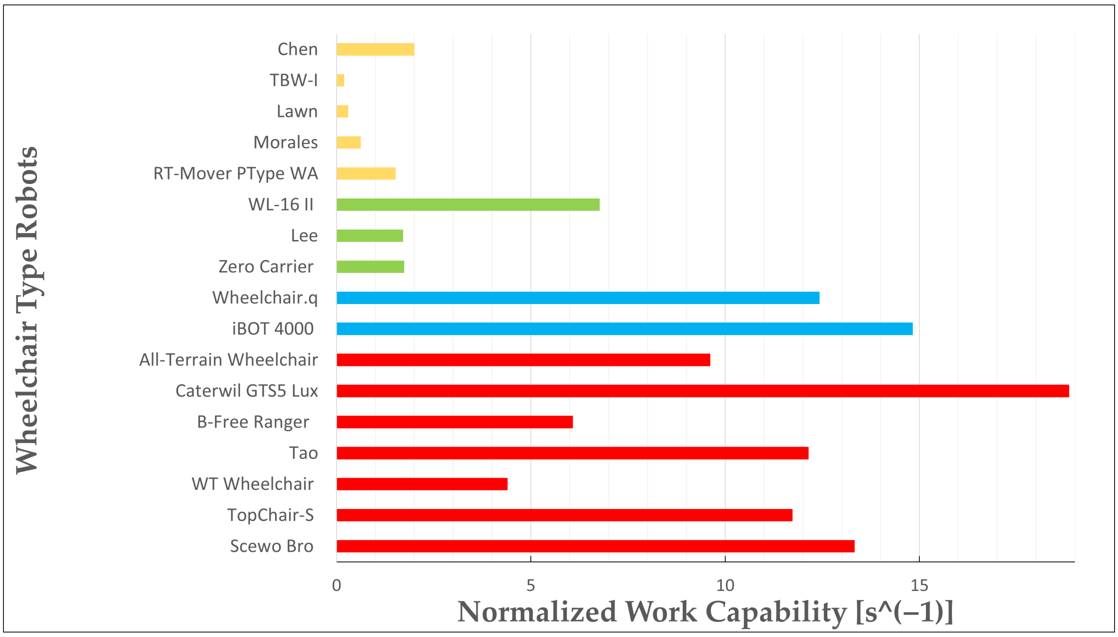

Figure 1.5: Normalized Work Capability comparison for wheelchair type robots; Chen [34]; TBW-I [35]; Lawn [37]; Morales [36]; RT-Mover PType WA [38–40]; WL-16 II [32, 33]; Lee [29]; Zero Carrier [27, 28]; Wheelchiar.q [22, 25]; iBOT 4000 [21, 24]; All-Terrain Wheelchair [15]; Caterwill GTS5 Lux [19]; B-Free Ranger [17]; Tao [13]; WT-Wheelchair [16, 20]; TopChair-S [12]; Scewo Bro [8].

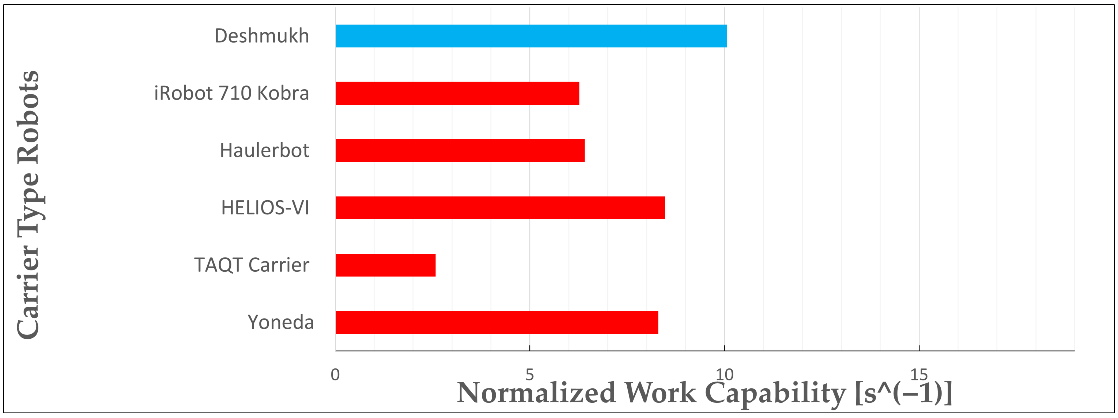

Figure 1.6: Normalized Work Capability comparison for carrier type robots; Deshmukh [48]; iRobot 710 Kobra [46]; Haulerbot [45]; HELIOS-VI [43]; TAQT Carrier [44]; Yoneda [42].

wheelchair-type robots while Figure 1.8 refers to carrier-type robots. Based on these two metrics, different categories do not cluster clearly. Each single robot may be designed in such a way to match desired values of maximum step height and slope regardless of the category it belongs.

Here, the Transport Ability (TA) is introduced to quantify how effective the

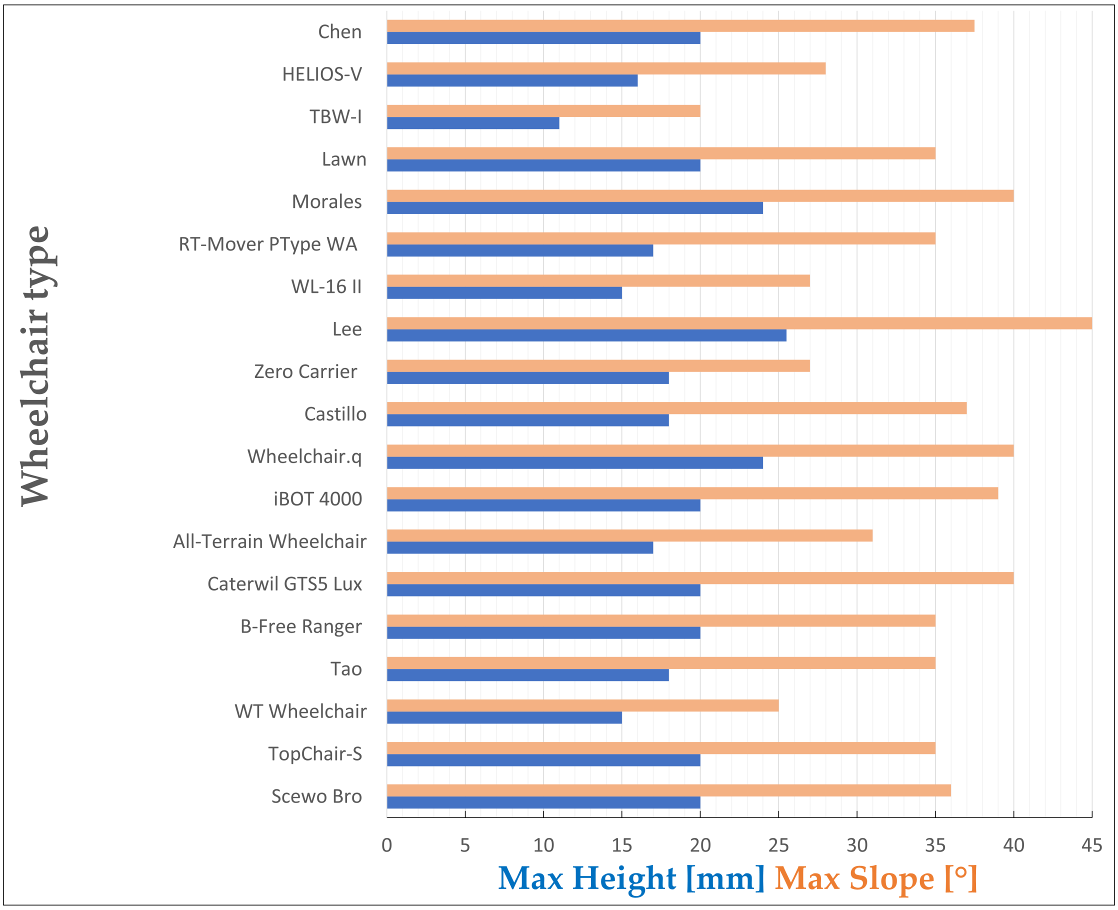

Figure 1.7: Max crossable height and slope comparison for wheelchair type robots; Chen [34]; HELIOS-V [41]; TBW-I [35]; Lawn [37]; Morales [36]; RT-Mover PType WA [38–40]; WL-16 II [32,33]; Lee [29]; Zero Carrier [27,28]; Castillo [23]; Wheelchiar.q [22,25]; iBOT 4000 [21,24]; All-Terrain Wheelchair [15]; Caterwill GTS5 Lux [19]; B-Free Ranger [17]; Tao [13]; WT-Wheelchair [16,20]; TopChair-S [12]; Scewo Bro [8].

robot is at carrying payload during stair-climbing operation. We defined it as the ratio of the payload mass to the maximum robot power.

$$\text{Transport Ability } (TA)[\text{kg/W}] = \frac{\text{Payload mass}}{\text{Robot power}} \tag{1.4}$$

The value of TA represents how many kilograms of payload the robot can transport using a unit quantity of power, and so how effective the robot is during transport operation. Again, the values calculated for different robots are reported in Appendix A. When data are not provided, the metrics are not reported. A comparison bar chart of Transport Ability values is provided in Figure 1.9 for wheelchair-type robots and in Figure 1.10 for carrier-type robots. Red is used to indicate track-based robots, blue to wheel-cluster based, green to hybrid and leg-based and yellow to articulated mechanism-based robots. The most transport-effective categories appear to be track-based and wheel cluster-based because they

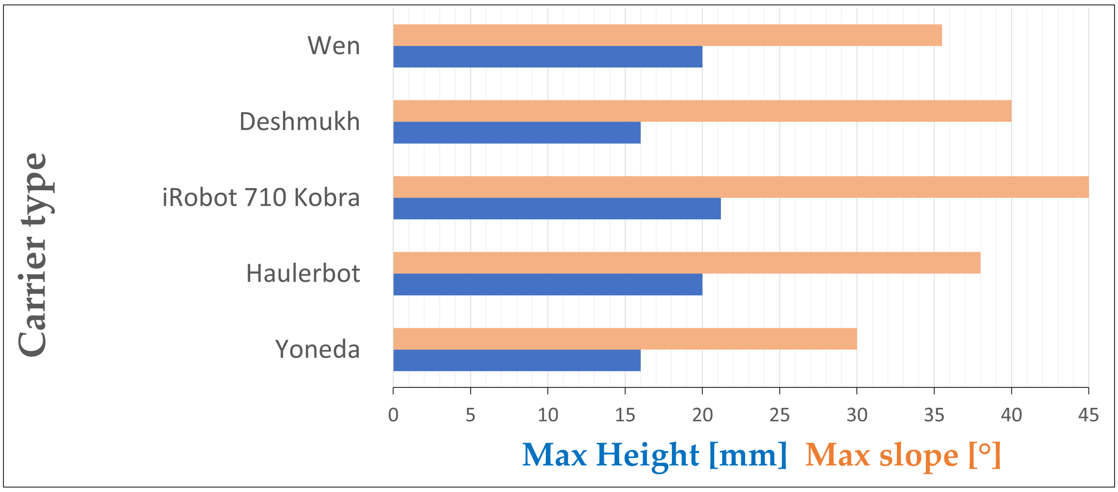

Figure 1.8: Max crossable height and slope comparison for carrier type robots; Wen [49]; Deshmukh [48]; iRobot 710 Kobra [46]; Haulerbot [45]; Yoneda [42].

reach higher value of TA. In fact, they combine a good carrying capacity with a small number of actuators. In contrast, the articulated mechanism-based robots and hybrid and leg-based categories, using many actuators to move the system, exhibit lower transport effectiveness because they reach lower values of TA.

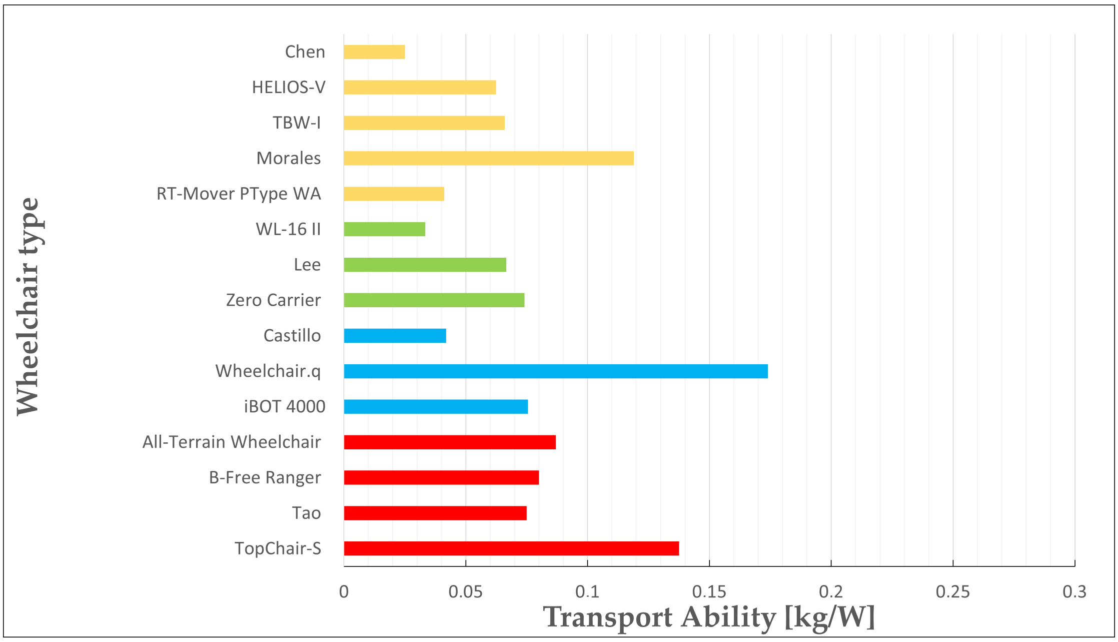

Figure 1.9: Transport Ability comparison for wheelchair type robots; Chen [34]; HELIIOS-V [41]; TBW-I [35]; Morales [36]; RT-Mover PType WA [38–40]; WL-16 II [32, 33]; Lee [29]; Zero Carrier [27, 28]; Castillo [23]; Wheelchiar.q [22, 25]; iBOT 4000 [21, 24]; All-Terrain Wheelchair [15]; B-Free Ranger [17]; Tao [13]; TopChair-S [12].

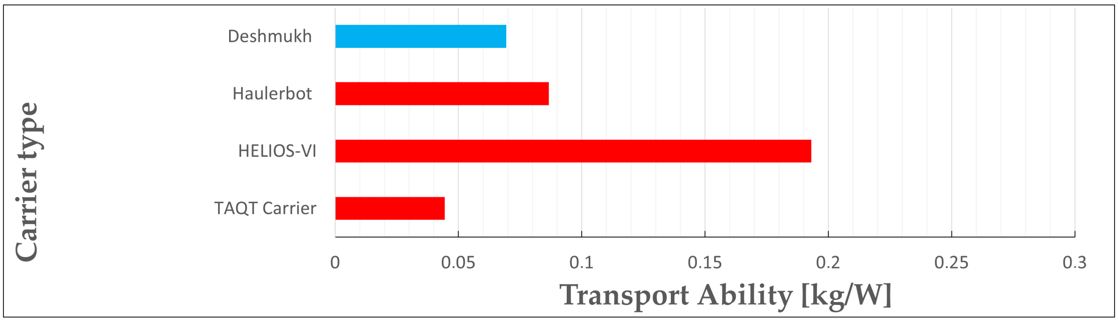

Figure 1.10: Transport Ability comparison for carrier type robots; Deshmukh [48]; Haulerbot [45]; HELIOS-VI [43]; TAQT Carrier [44].

1.3.2 Comparison Charts

To have a graphical representation of the various performance metrics and their correlation, several scatter plots are provided. Track-based robots are reported with red points, wheel cluster-based robots are reported in blue, hybrid and leg-based robots are reported in green, and articulated mechanism-based robot with yellow points. Figure 1.11 relates the two independent metrics: the Payload Capacity and the Normalized Speed. It can be observed that most of the points fall below an imaginary diagonal that from the top left to the bottom right cuts the graph into two parts. This highlights the intuitive inverse proportionality that exists between the payload and the transport speed. The lower the payload, the higher the speed of the robot. On the contrary, when the payload to be transported is very heavy, the speed of the robot decreases considerably. Articulated mechanism-based robots deviate from this behavior. Indeed, the normalized speed is almost independent on the payload capacity of each robot, as a result of a technical limitation of the gate-based walking strategy typical for this category.

It is important to observe the distribution of the various types of robots in the graph of Figure 10. For the two-dimensional data ($[NS, PC]$) pertaining to a given category, a standard deviational ellipse can be defined centered on the mean center and considering one standard deviation. These ellipses were created using the Gaussian Ellipsoids function of the MatLab ® software (MathWorks, Natick, MA, USA). It can be seen how the ellipse of the articulated mechanism-based robots (marked in yellow) lies in an area at the bottom of the graph. These vehicles cannot carry a load greater than the robot's own weight and never exceed a Normalized Speed of 0.02 s^{-1}. Hybrid and leg-based robots (green ellipse), despite being able to carry a wide range of payloads, never exceed an NS value greater than 0.1 s^{-1} Wheel cluster-based vehicles are always able to carry a payload comparable to the weight of the robot and at a speed higher than both that of articulated mechanism-based robots and that of hybrid and leg-based robots. Finally, the track-based robots are distributed in the central area of the graph. It is thus evident that they can carry a payload comparable to the weight of the robots. In addition, the arrangement of the ellipse on the graph shows that track-based

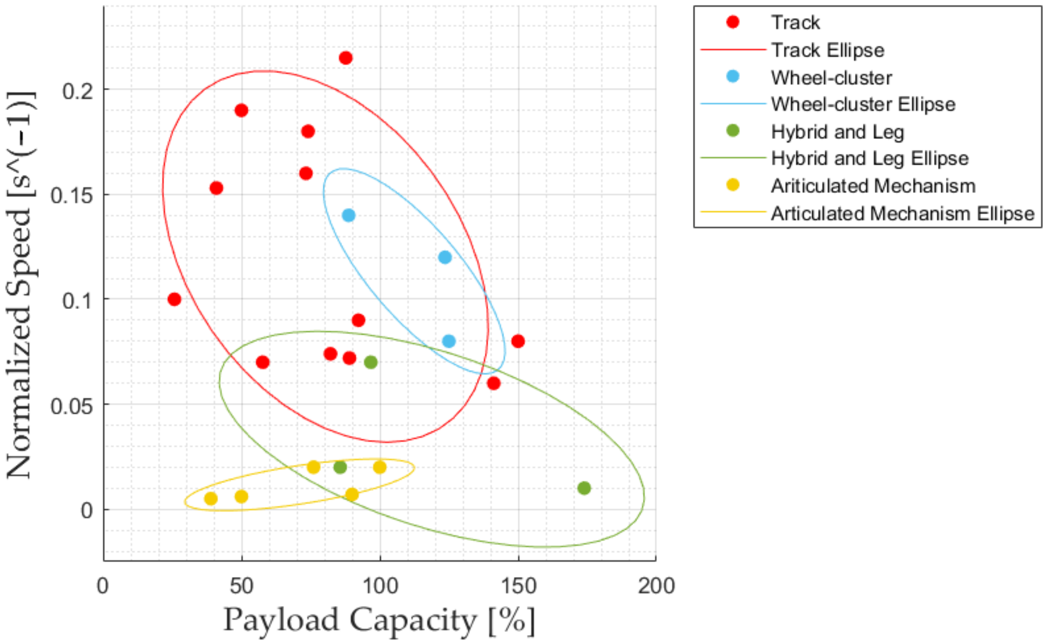

Figure 1.11: Payload Capacity—Normalized speed scatter plot

robots on average have a higher transport speed than the other categories.

In Figure 1.12, the NWC is shown as a function of the PC for the four types of vehicles. The distribution in this plane is significant. Again, to better highlight the arrangement of the different categories within the chart, it is also possible to add the already mentioned Gaussian ellipses to the graph. These ellipses are based on the statistical values of the PC and NWC parameters. Recall that the NWC is an index of the total performance of the vehicle, as it considers the load transported and the speed of transport [56]. Once a PC value is calculated, it is possible to identify which category of robot has better performance based on the position of the ellipses in the chart plan. Track-based and wheel cluster-based robots are more suitable for carrying a load on stairs because their ellipses reach higher values of NWC than the articulated mechanism-based and hybrid and leg-based robots.

We define the stairs slope as the inclination respect the horizontal of the notional line connecting the nosing of all treads in a flight. Compared to the step height, the slope considers not only the height of the step, but also the depth of the same. For this reason, when comparing the performance of different robots, it is preferable to use the maximum slope of the stairs. Then, Figure 1.13 illustrates the maximum stairs slope to payload capacity scatter plot. It can be seen which slope of stairs can overcome the different categories of robots. It emerges that most categories of robots are able to overcome values of stairs slope included in the range $25 - 45°$. These are the typical slope values of stairs for most real applications.

In Figure 1.14 the maximum stairs slope values for the different robots are dia-

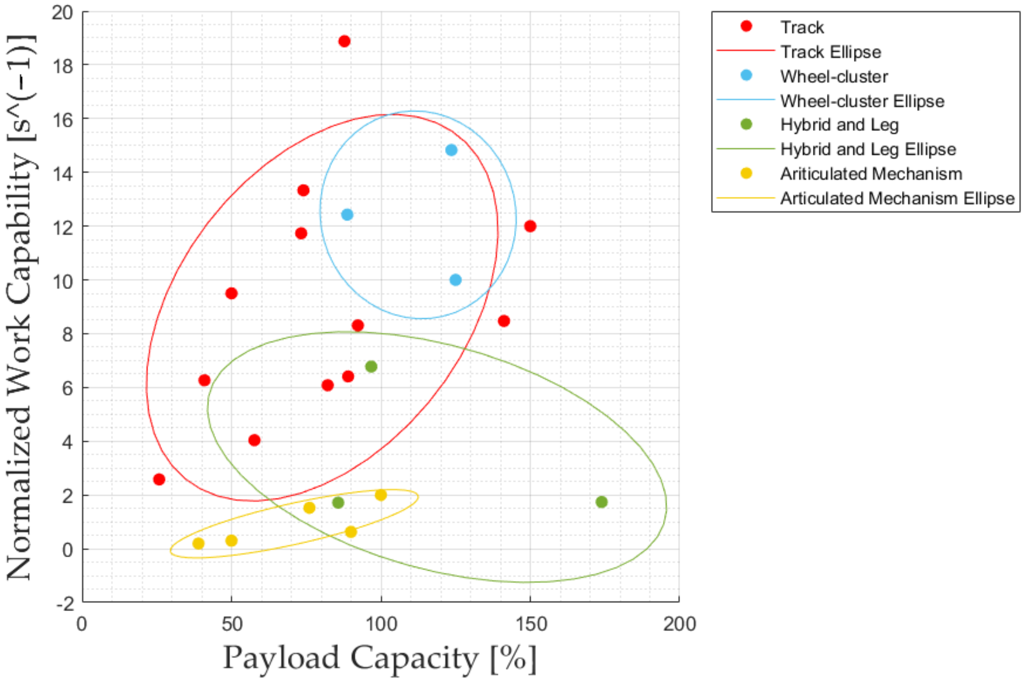

Figure 1.12: Normalized Work Capability—Payload Capacity scatter plot.

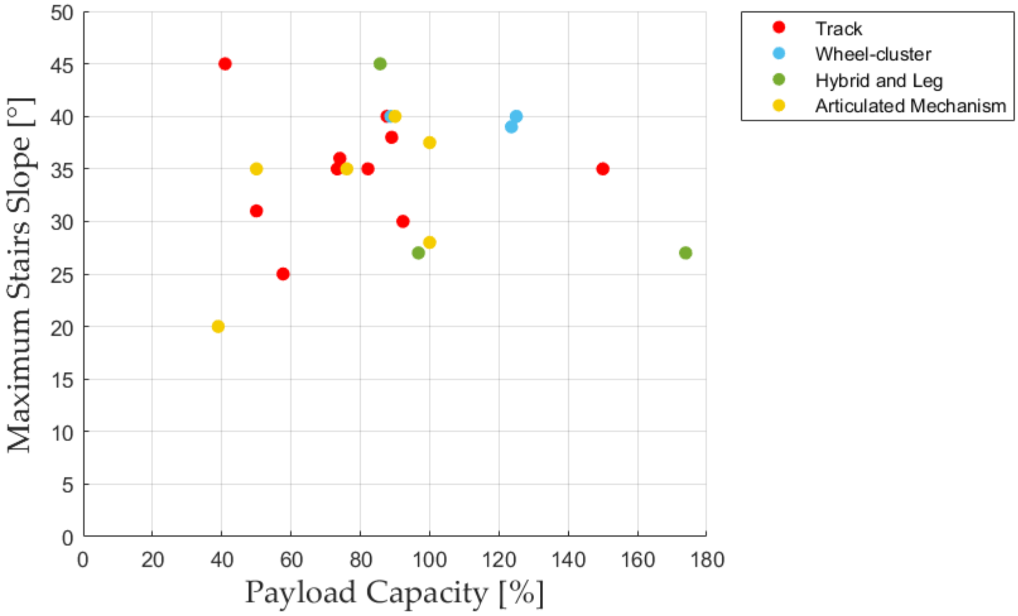

Figure 1.13: Maximum stairs slope—Payload Capacity scatter plot.

grammed as a function of Normalized Work Capability instead of Payload Capacity. The maximum slope range of stairs is always between 25° and 45°. The graph

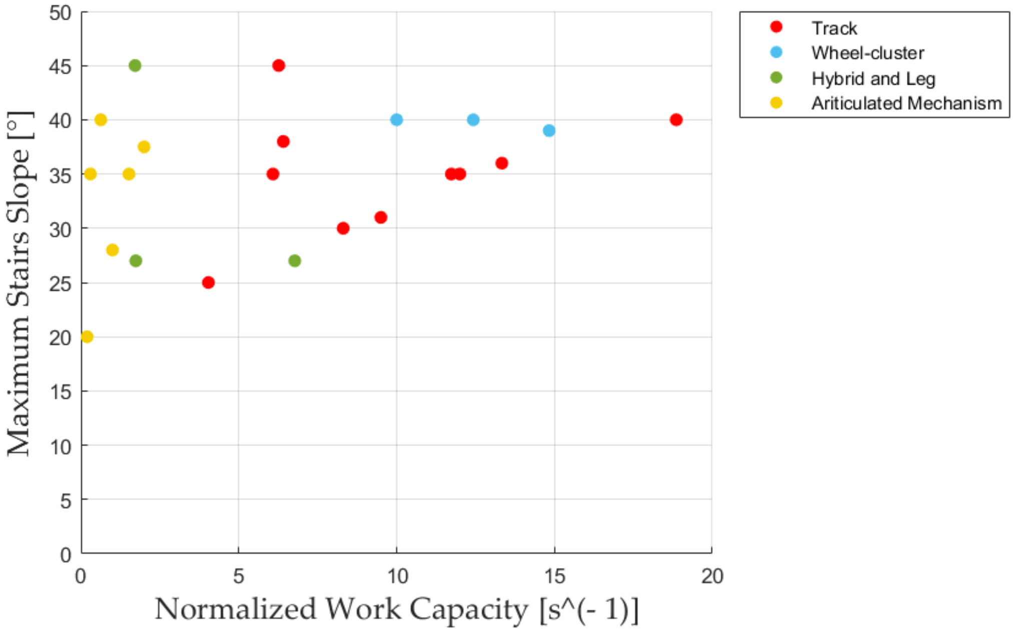

Figure 1.14: Maximum Stairs Slope—Normalized Work Capability scatter plot.

shows that the two categories that have the highest total performance are track-based and wheel cluster-based, as they have higher Normalized Work Capability values in that range, so that they are most suitable to perform the stair-climbing task respect to articulated mechanism-based and hybrid and leg-based robots.

Figure 1.15 shows the Transport Ability versus Payload Capacity scatter plot. Again, to better highlight the arrangement of the different categories within the chart, it is also possible to add the already mentioned Gaussian ellipses to the graph. These ellipses are based on the statistical values of the TA and PC parameters. Hybrid and leg-based robot ellipse is almost horizontal, sign that the Transport Ability varies little as the load carried varies. Moreover, hybrid and leg-based category has the lowest transport ability for all payload capacity values. On the contrary, wheel cluster-based robot ellipse is almost vertical, sign that the Transport Ability varies greatly depending on the climbing mechanism used. The most high transport ability value belongs to track-based robots category.

At the end, Figure 1.16 relates the two independent metrics: the Transport Ability and the Normalized Work Capability. As we have already said, the NWC is an index that reflects a bit the overall performance of the robot, since it considers both the load capacity and the transport speed of the robot. Similarly, TA is an index that considers how much power the robot needs to carry a unit load. Based on these two parameters, the Transport Ability-Normalized Work Capability graph can be divided into four zones: (1) in the top right the area of the robots with high overall performance and high transport ability, (2) in the bottom right the area of the robots with high overall performance but with low transport ability,

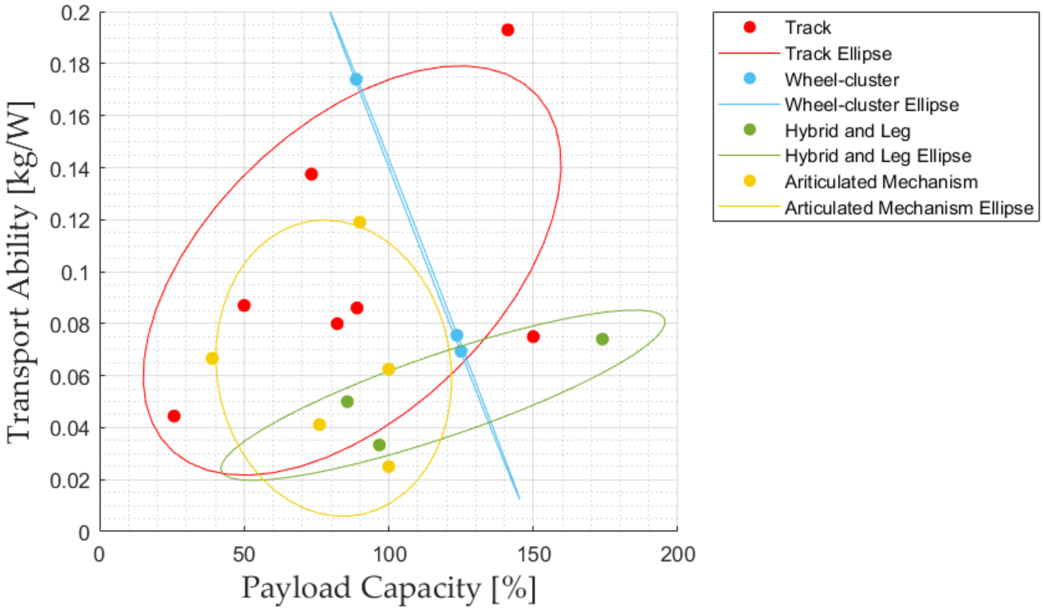

Figure 1.15: Transport Ability to Payload Capacity scatter plot.

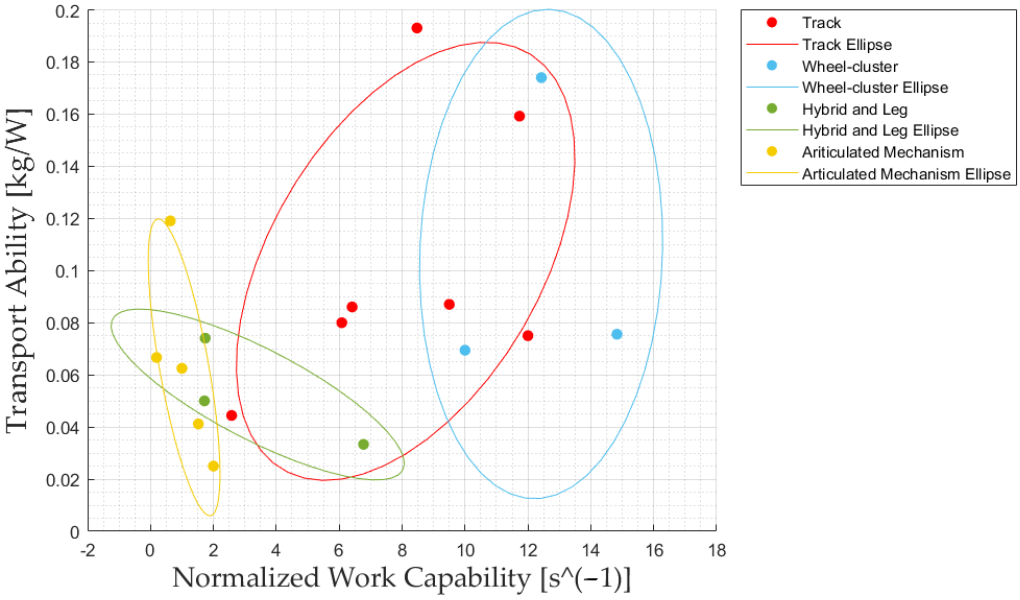

Figure 1.16: Transport Ability to Normalized Work Capability scatter plot.

(3) in the top left the area of the robots with high transport ability but with low overall performance, (4) in the bottom left the area of the robots with low transport ability and low overall performance. Moreover, in this case, to highlight the arrangement of the points of the different categories, the ellipses have been

added.

So, from the position of the ellipses in the $TA - NWC$ plan in the figure, it is possible to have important indications on the different categories of robots that cannot be deduced a priori through a single qualitative analysis of the systems. Articulated mechanism-based robots are shown to have variable transport ability depending on the climbing mechanism used. However, they demonstrate low overall performance by positioning themselves in the leftmost area of the graph plane in Figure 1.16. Wheel cluster-based and track-based robots are the categories that come closest to the area of the plan with high overall performance and high transport ability, proving to be the most suitable categories for transporting a payload on a flight of stairs. In contrast, the hybrid and leg-based robots category clusters in an area with low transport ability and low overall performance.

1.3.3 Complexity and Cost Issues

Drawing from [57], fundamental design choice criteria in mobile robotics are mechanical and control complexity, as also underlined in [5].

Mechanical complexity has a considerable influence on the reliability of robot operation. Track-based and wheel cluster-based robots are apparently simple and robust, while robots with complicated mechanical designs, such as legged and articulated-mechanism based robots are complex and delicate. Control complexity has significant influence on the robot motion control. It is higher for solutions involving legs and a sophisticated mechanism due to gait planning requirements.

Mechanical and control complexity can be used to evaluate the simplicity of realization of one robot compared to another. Therefore, in addition to the performance metrics of Section 1.3.1, it is decided to develop a qualitative evaluation scale of mechanical complexity (MC) and control complexity (CC) for the robots analyzed in this paper. Detailed numeric data are presented in Appendix A. Scores start from low and continue with medium-low, medium, medium-high, high and very-high.

Another fundamental design parameter is the overall cost. From mechanical and control complexity, it is possible to obtain an idea of the possible cost of the robot. It is plausible that an expensive solution has very high complexity. Therefore, cost is used to evaluate the simplicity of realization of one robot compared to another, and how much a robot can be easily sold compared to another one. It is also decided to draw up a qualitative evaluation scale of cost for the robots in this paper. Cost evaluation scores are presented in Appendix A. Scores start from low and continue with low-medium, medium, medium-high and high. To have a graphical representation of the results obtained, a cost scale graph is provided below in Figure 1.17. The five cost grades and the total number of robots belonging to each grade are reported on the abscissa and ordinate axis, respectively.

It is useful to say that the wheelchair type track-based robots Scewo Bro [8] and B-Free Ranger [17] are now available for $\$40,536$ and $\$17,688$, respectively. Wheel cluster-based robot iBOT 4000 Mobility System [24] was available for $\$26,000$ in the period from 1999 to 2016. Figure 1.17 provides information on how robots

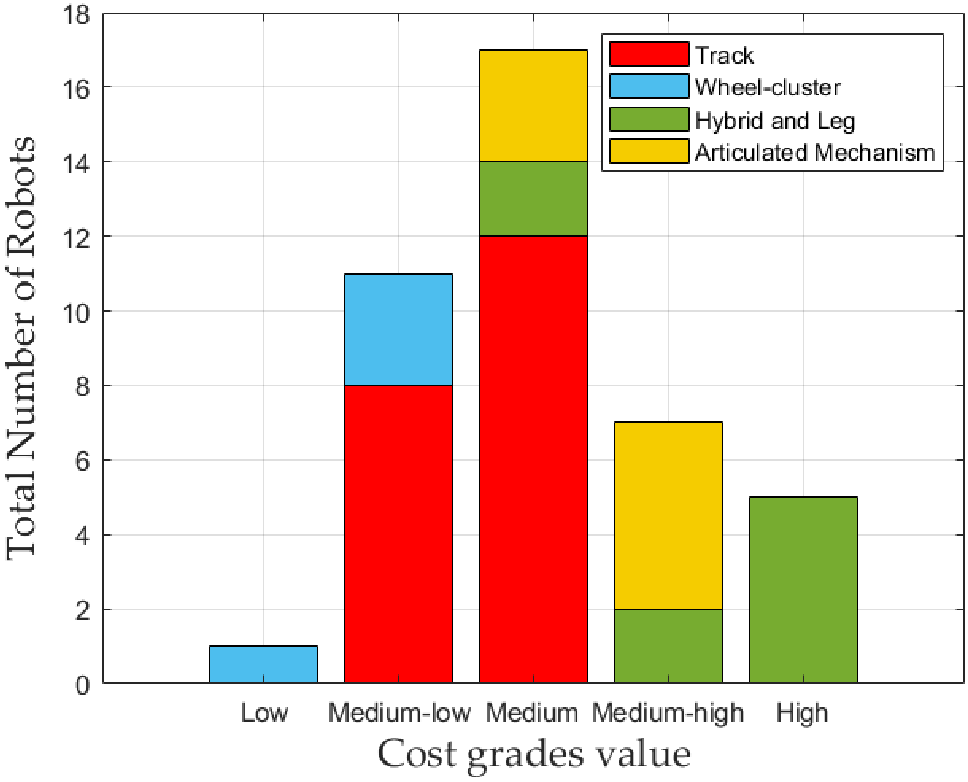

Figure 1.17: Cost scale graph.

type affects the cost. Due to the elaborate mechanical structure, the presence of numerous actuators and sensors and the complexity of the control system, the most expensive robots are the legged ones, immediately followed by the articulated mechanism-based ones. Track-based robots have an average system cost, while wheel-clustered robots are the cheapest type to make.

1.4 Conclusion

This chapter surveyed the current state-of-the-art in stair-climbing vehicles to obtain useful information about which category of robot is best able to transport people and heavy loads up a flight of stairs. In the first part, a brief description of the stair-climbing existing mechanisms and method of operation are provided. Then, based on the capability of carrying payload and the type of locomotion mechanism, we propose a general stair-climbing system categorization. Next, to compare the different payload robots, several quantitative performance metrics are defined and calculated on the purpose, namely: payload capacity, normalized speed, normalized work capability, maximum step height, maximum stairs slope and transport ability. Correlations among previous performance metrics are sought by plotting one metric against the other, providing the reader with an in-depth understanding of the stair climbing problem. Then, complexity and cost issues are addressed. As a conclusion of the chapter, we tried to identify what to look at to choose the best category for transporting people and heavy loads up a flight of stairs. The normalized work capacity parameter is chosen to quantify the overall performance of different climbing robots and the respective categories. A complete overview of the different stair-climbing system performance is obtained when expressing Transport Ability as a function of Normalized Work Capability. Since hybrid and leg-based robots are located in the lower left area of the $TA-NWC$ plan (Figure 1.16) and have a high cost, they prove to be the least suitable category for transporting a payload on a flight of stairs. Moreover articulated mechanism-based robots do not seem suitable for stair-climbing operations This is because they have low overall performance, low transport ability, complicated mechanical structure and control strategy. On the contrary, track-based and wheel cluster-based robots prove to be the most suitable categories to perform the transport of a load during the ascent of a flight of stairs. This is because they combine good overall performance and good transport ability, positioning in the right part of the $TA-NWC$ plan (Figure 1.16), with low mechanical complexity, simple control strategy and low construction cost. With these results it will be possible to design a track-based or wheel-cluster based robot that better than articulated mechanism-based robots and hybrid and leg-based robots can transport people and heavy loads up a flight of stairs.

Chapter 2

Rubber belts and tires: a detailed insight into force analysis during obstacle negotiation

Robotic vehicles are increasingly being deployed to perform tasks in hazardous environments and repetitive operations. Nowadays, they are extensively used for various applications, such as surveillance, monitoring, military operations, healthcare, and agriculture. In particular, tasks involving the inspection and monitoring of infrastructures and buildings, both commercial and residential, pose significant challenges. These tasks often involve operations in confined spaces or the transport of heavy loads across multiple floors, where the presence of stairs and other obstacles can pose significant risks to human operators due to physical stress or injury. The introduction of automation and robotics into these environments aims to reduce human error and increase efficiency. Consequently, research into robotic systems for inspection, transportation, and monitoring has grown in recent years. A key challenge faced by such robots is the ability to overcome obstacles, with stairs being among the most common in these environments. Tracked or wheeled platforms are frequently utilized for tasks that require climbing stairs or other similar obstacles, such as moving heavy goods or assisting individuals with mobility impairments. However, negotiating stairs often leads to mechanical stress and stability issues, even with advanced articulated tracked or wheeled platforms. Furthermore, improper operation or no optimal design of tracks or wheels can result in critical failures, such as tipping or damage to the rubber components. This chapter proposes a rigorous analysis approach to study what happens when a rubber belt, or a tire, come in contact with a step corner edge and what forces are exchanged between these two elements.

2.1 Research motivation and literature review

The tractive force caused by the wheel-terrain interaction determines the ability of the vehicle to climb slopes, accelerate and negotiate obstacles. Figure 2.1, taken

Figure 2.1: A tyre facing a step-like obstacle taken from [58]

from [58], shows a tyre during the negotiation of an obstacle similar to a sidewalk edge; as it is possible to note the tyre changes its shape near the contact with the corner edge. When this happens the tyre deflection that occurs between the treads and the corner edge generates two angles: β which is related to the upper branch and α related to the bottom branch of the tyre. The values of these angles strictly depend on the amount of tyre deformation and change continuously during the motion sequence. Such a deformation is seldom taken into account in the existing tyre contact models.

One of the common models is the rigid wheel [59], which consists of a rigid rim rolling over obstacles where only one single contact point is considered by neglecting what actually occurs in the real world where a wheel has more than one contact point with the surface. Attempts have been made to include the tyre deformation in the contact mechanics. For example, in Thomas and Vantsevich [60] a mathematical model of a wheel moving over an obstacle was presented with the aim of designing an advanced wheel system able to provide an optimal distribution of the normal and traction forces on the drive wheels and improves the performance of the vehicle dynamics. In this study a single wheel is considered when walking over a non-deforming obstacle whose height h_0 is smaller than its radius R with an applied torque T_w. The weight force W_w and the longitudinal force F_f act on the wheels while it rolls over the obstacle while the normal and tangential forces F_n and F_t respectively are generated as soon as the tyre comes in contact with the corner edge of the obstacle. The normal reaction R_z starts decreasing and drops to zero as the wheel loses the contact with the ground and is supported only by the edge of the obstacle. The tangential force F_t is described as $F_t = F_n \nu_p$ where ν_p is the coefficient of adhesion so in this case the normal force F_n on the corner edge of the obstacle is considered to be directed towards the direction of the centre of the wheel.

The same considerations are proposed in Wang et al. [61, 62] where the relationship between wheeled vehicle parameters and the ability to overcome a step obstacle is derived through mechanical analysis. It is supposed that the vehicle travels slowly while overcoming the obstacle such that the effect of the inertial force can be neglected. Figure 2.2, taken from [61], shows how the tire deforms when it is in contact with the obstacle. Even in this research study, the forces acting on the wheel are the same described in Thomas and Vantsevich [60] by

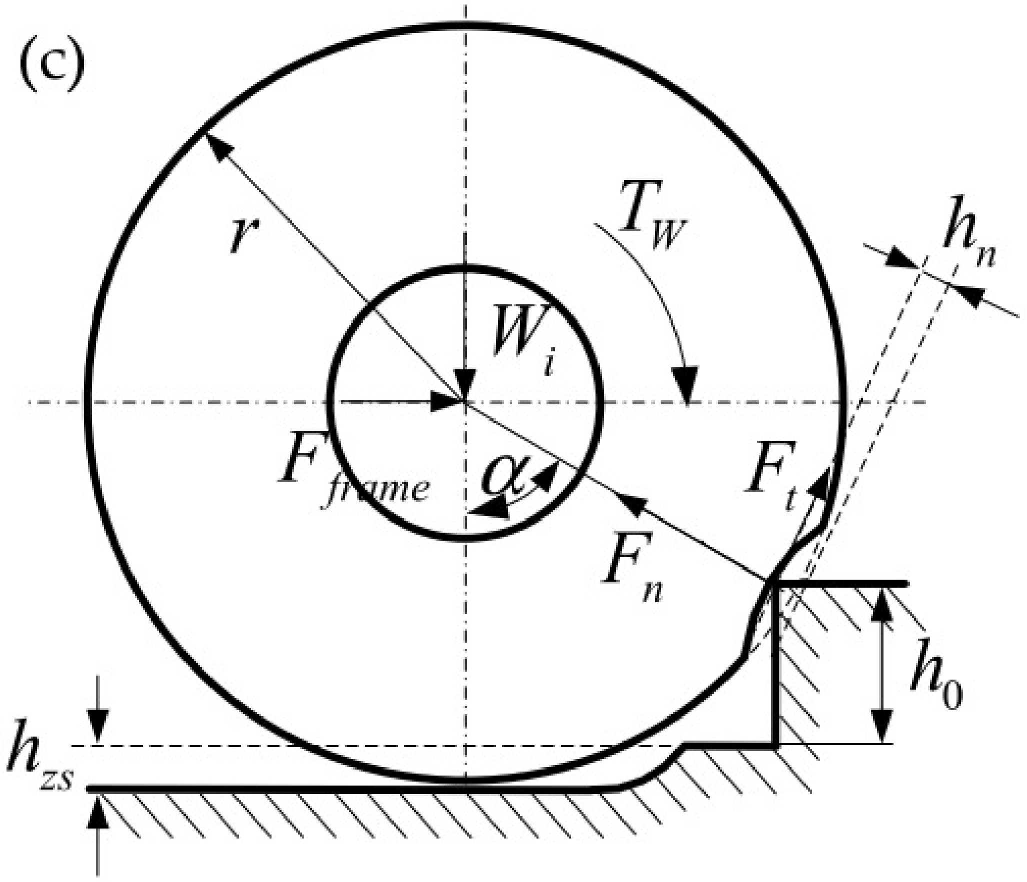

Figure 2.2: Wheel-obstacle interaction proposed in [61]

considering once more the normal force as directed to the centre of the wheel.

The main motivation behind this research study is the lack of a comprehensive wheel-obstacle contact model that takes into account the tyre tread deformation. What we criticize in this literature is the fact that the deformation of the tire when it hits a step is not like that shown in Fig. 2.2. The tire with the step forms two angles that are not considered in the [60, 61], and [62] discussions and which we assume will influence the process. There is no reason to consider the force F_n directed exactly in the centre of the wheel since, in the presence of the torque T_w, the wheel centre takes on no special significance. Instead, we consider that the direction of the force F_n depends on how the wheel deforms upon contact with the step. Please take Fig 2.3 as a reference where, for simplicity, we consider $h_{zs} = 0$ e $F_{frame} = 0$. The tire deflection that occurs between the treads and the corner edge generates two angles: β, which is related to the upper branch, and α, related to the bottom branch of the tire. The values of α and β change continuously during the motion sequence and strictly depend on the amount of tire deformation. Being able to correctly study what happens during the contact between a running gear

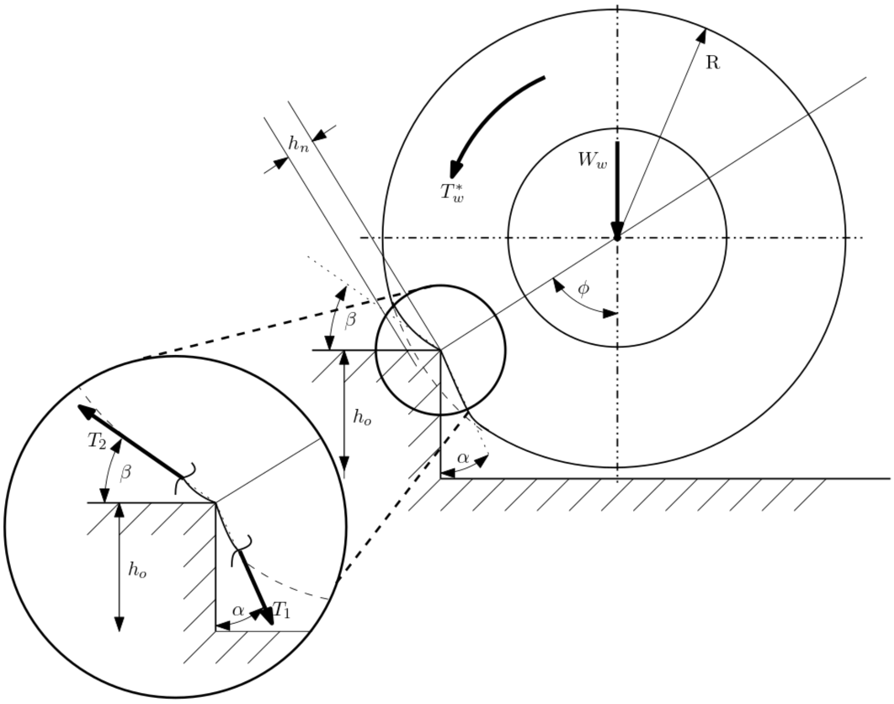

Figure 2.3: Wheel-obstacle interaction propose

(a pneumatic tyre or a rubber belt) and a corner edge is extremely important to assess the ability of a vehicle to traverse rough terrain.

2.2 A novel approach to wheel-obstacle contact mechanics

The wheel in Figure 2.3 has its tyre tread in contact only with the corner edge and does not exchange any force with the ground. By assuming a condition of incipient slippage between the tyre tread and the corner edge with a negligible effect of the tyre shoulder, the force system exchanged by the tyre and obstacle can be obtained by treating the portion of the tyre tread that is in contact as an equivalent belt at whose extremes act the tension T_1 and T_2, as explained in Figure 2.3. The angle β is the angle between the upper branch of the belt and the horizontal plane of the step while under tension T_2; similarly, the angle α is the angle between the lower branch of the belt and the vertical plane of the step while under tension T_1.

2.3 Experimental setup

As it is possible to see in Figure 2.4, a testbed has been specifically designed in order to analyse the behaviour of a rubber specimen in contact with a step-like obstacle. The theoretical model of the force system exchanged is shown in Figure 2.5, where T_1 is the tension at the upper branch and T_2 is the tension at the

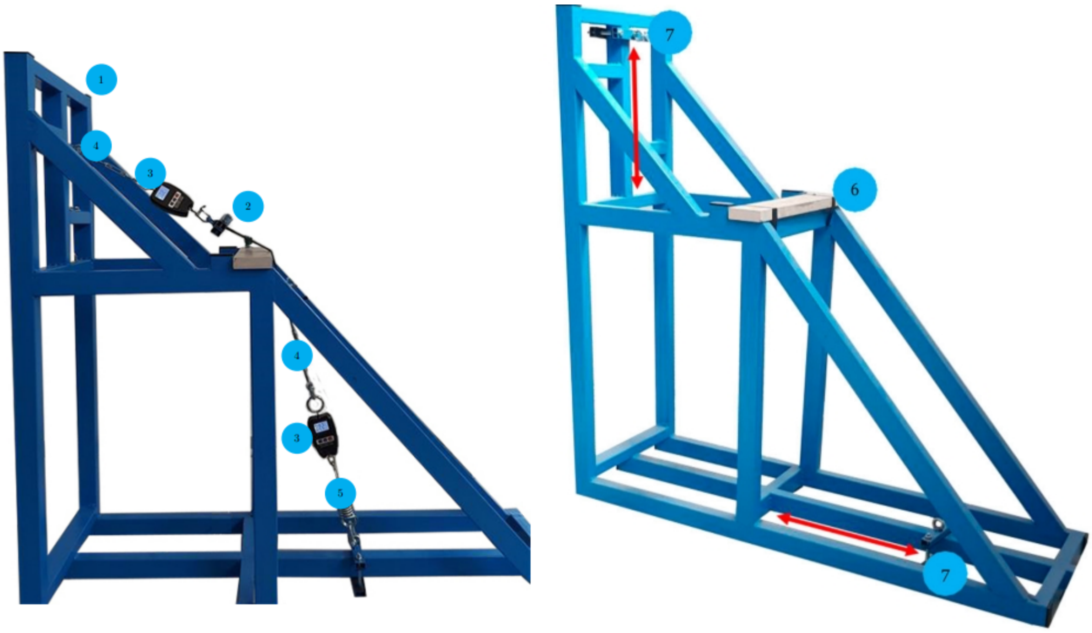

Figure 2.4: The testbed used for the experiments. (a) A side view of the testbed and (b) The upper and lower sliders used to adjust α and β angles.

lower branch of specimen. If these values are known and under the assumption of incipient slippage, then, it is possible to measure the exchanged forces on the corner edge. The structure of the testbed (1) features an upper and a lower adjustable clamp to set up different belt (2) tension angles by changing the position of the clamps over the horizontal and vertical bar. Two digital tensiometers (3) are mounted in series with two manual tensioners (4) and they are used to measure the forces acting on both sides of the specimen. The testbed allows to safely measure the forces acting on the belts while gradually increasing the tension on both sides by tightening the tensioners. The tensioner placed on the bottom side is connected to a spring (5) to allow relative sliding between the belt and the step corner. The testbed can hold (6) corner edges of different materials, i.e. concrete, marble or wood, to replicate the actual step corners and perform the tests as in real-world conditions. Finally, the upper and lower sliders (7) can be used to adjust the angles α and β as it is reported in Figure 2.4.

Figure 2.5 shows the diagram of the forces acting on a sample belt against a corner edge while both sides are under tension. The angle β is the angle between the upper side of the belt, while under tension T_1, and the horizontal plane of the step; similarly, the angle α is the angle between the lower side of the belt and the vertical plane of the step while under tension T_2. In addition, it is worth noting that when it is under tension, the relative angle θ between both the upper side and the lower side of the belt should be accounted as well as the angle δ which is the angle between the bisector of the angle between the upper and the lower side of the belt and the resultant of the contact forces. The resulting force F does not point in the same direction as the bisector of the two branches of the belt because of the friction between the belt itself and the corner edge.

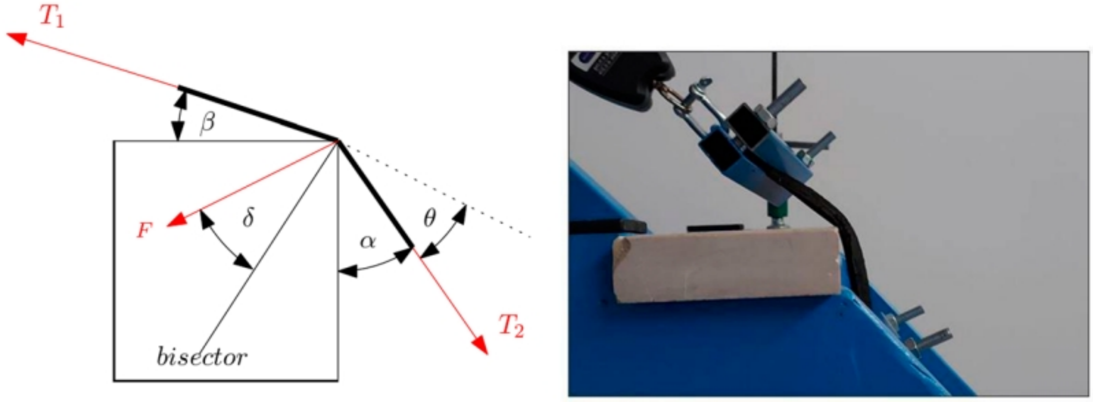

Figure 2.5: A diagram of the forces and the tyre used for the experimental tests. (a) Diagram of the forces acting on a sample belt or tire at the corner edge and (b) The tire used for the experiments with the test bed.

2.4 Experimental results

A series of experimental tests have been carried out in order to study the behaviour of different kinds of belts by changing the angles β and α and also the tension forces T_1 and T_2. At the beginning of each test, the upper clamp on the vertical bar has been set to obtain a desired β angle; then, for each β angle, the lower clamp on the horizontal bar was set to obtain different α and θ angles and the lower manual tensioner have been adjusted to pretension the system. By gradually tighten the upper manual tensioner, the measurements coming from both the digital tensiometers have been registered especially when the belt started to slip at the corner edge. This procedure has been repeated for each β and α angles and for each kind of belt tested during this research study. The ratio between the two tension forces $\frac{T_1}{T_2}$ in correspondence of each θ angle has been carefully addressed.

2.4.1 Rubber belt

The first test has been performed by using a rubber belt usually used for conveying and power transmission. The tensions on both the upper and the lower branches of the belt are measured in stationary phases by assuming a condition of incipient slippage. Figure 2.6 shows the trend of the $\frac{T_1}{T_2}$ curve according to different values of the β angle (38°, 28°, 19° and 6°). This first set of tests highlights a very interesting aspect: the ratio $\frac{T_1}{T_2}$ is not only affected by the β angle but also by the relative angle θ as described in the previous section. In fact, although they have different β angles, the curves reported in Figure 2.6 show a similar trend.

2.4.2 Tire

The same tests have been carried out on a section of a tyre tread 215/65r16 made by Bridgestone. Figure 2.7 shows the values of $\frac{T_1}{T_2}$ related to different values of the

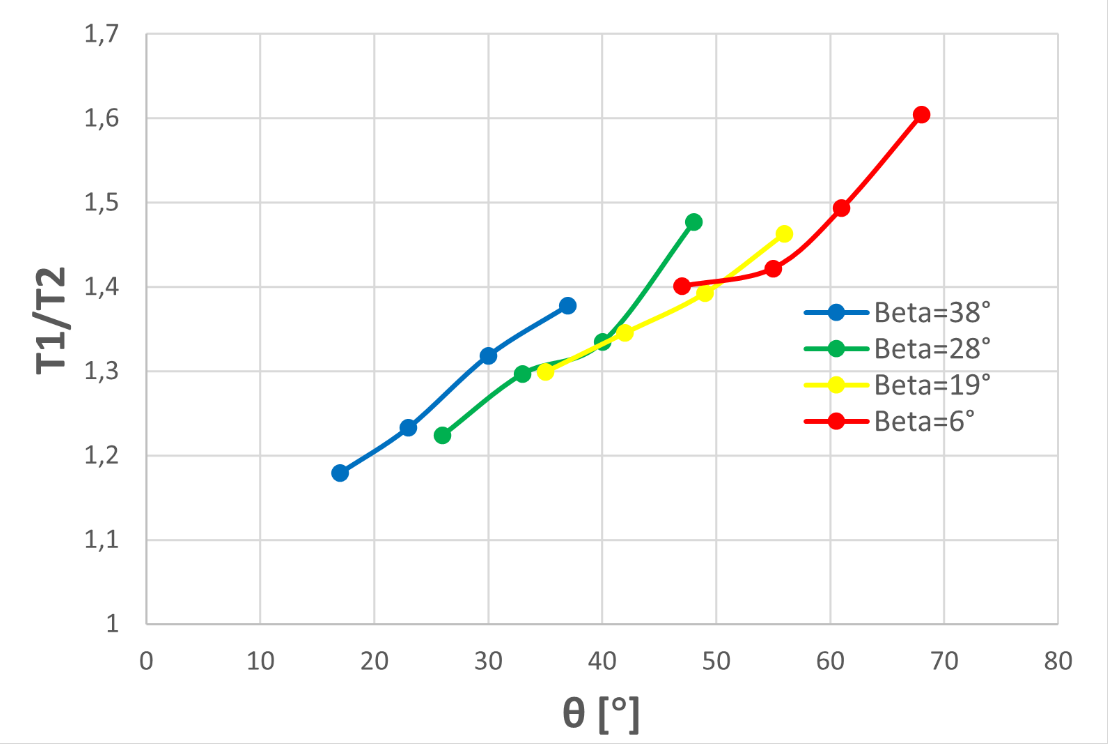

Figure 2.6: The relation between the tension forces and the β angle for the belt case

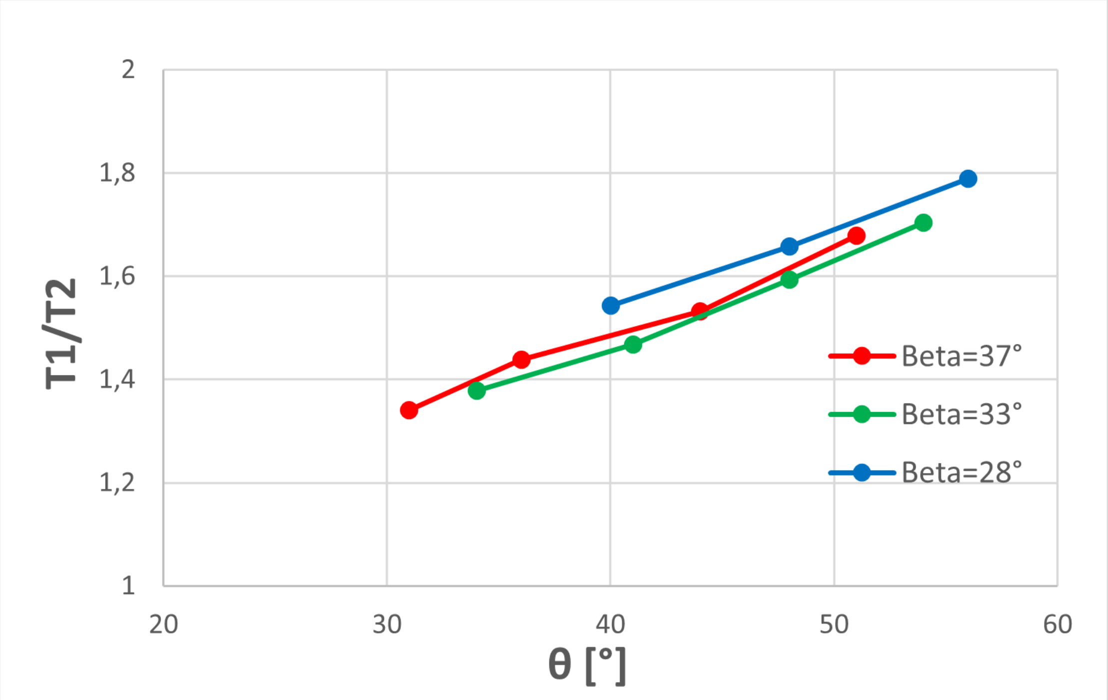

Figure 2.7: The relation between the tension forces and the β angle for the tire case

β angle, in particular, for $\beta = 37°$, $\beta = 33°$ and $\beta = 28°$. In this case, it is assumed that the tyre is subjected to deformation and the action of its shoulder tread is negligible; moreover, as with the belt, the tensions T_1 and T_2 are measured only during stationary phases under the condition of incipient slippage. Similarly to the belt case, it is possible to note that the ratio $\frac{T_1}{T_2}$ is not directly affected by the β angle, but most by the θ angle since even if they have different values for the β angle, their curves are almost very similar.

2.5 Experimental vs theoretical results

In this section, results coming from the experimental tests are compared with analytical models. The main theory refers to Euler that has been proposed for belt transmission where the thickness of the belt is much smaller than the radius pulley.

The Euler model, typically used to describe tension changes in flat belt transmissions, can be expressed as:

$$\frac{T_1}{T_2} = e^{\mu\theta} \tag{2.1}$$

where θ is the relative angle and μ is the coefficient of friction corresponding to the material of the corner edge used in the testbed previously measured with a tribometer. The results were obtained by applying the Euler model, assuming that

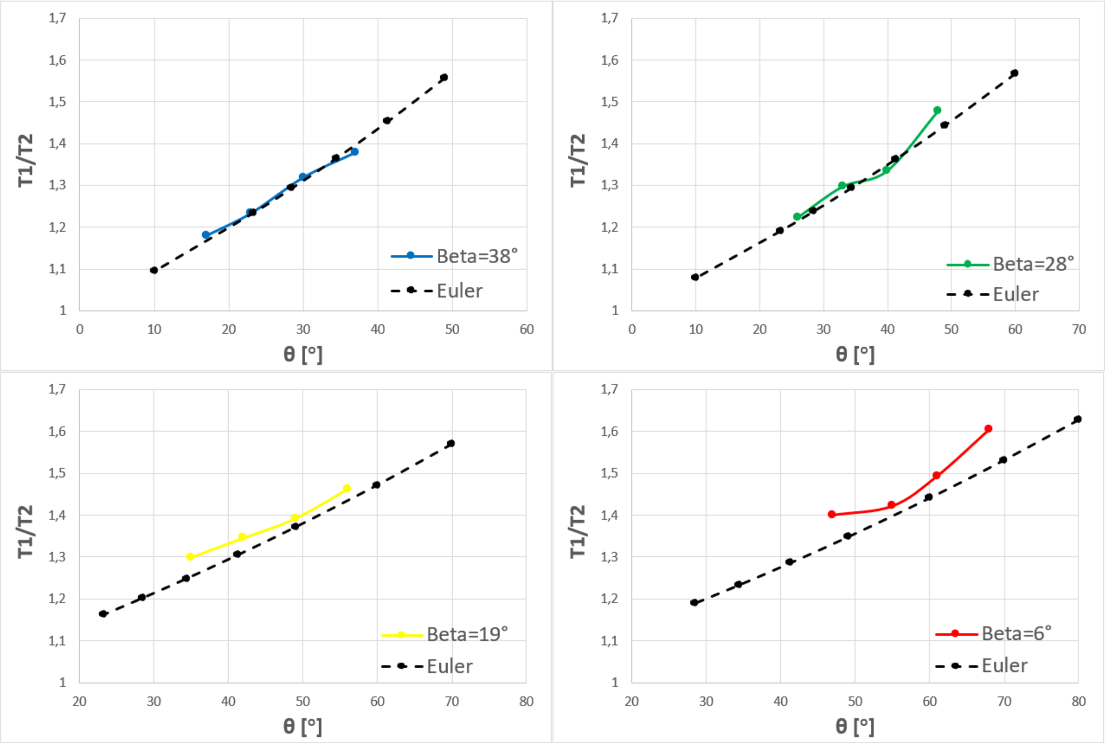

Figure 2.8: Euler model vs. rubber belt experimental results.

the system can be considered as a flat belt around a pulley, are compared with the experimental data in Figure 2.8. Since the behaviour of the four $\frac{T_1}{T_2}$ curves is similar, even in this case, the Euler model can be used to describe a system where a belt is in contact with a step corner edge. By relying on the same assumption, it is possible to model the contact between a pneumatic patch and a step corner edge. Figure 2.9 reports the comparison between the model and the real-world results for three different values of the β angle. It shows how the three couple of curves are very similar, indicating that the Euler model can well describe what happens when a pneumatic tyre is in contact with a step corner edge once the friction coefficient has been calculated.

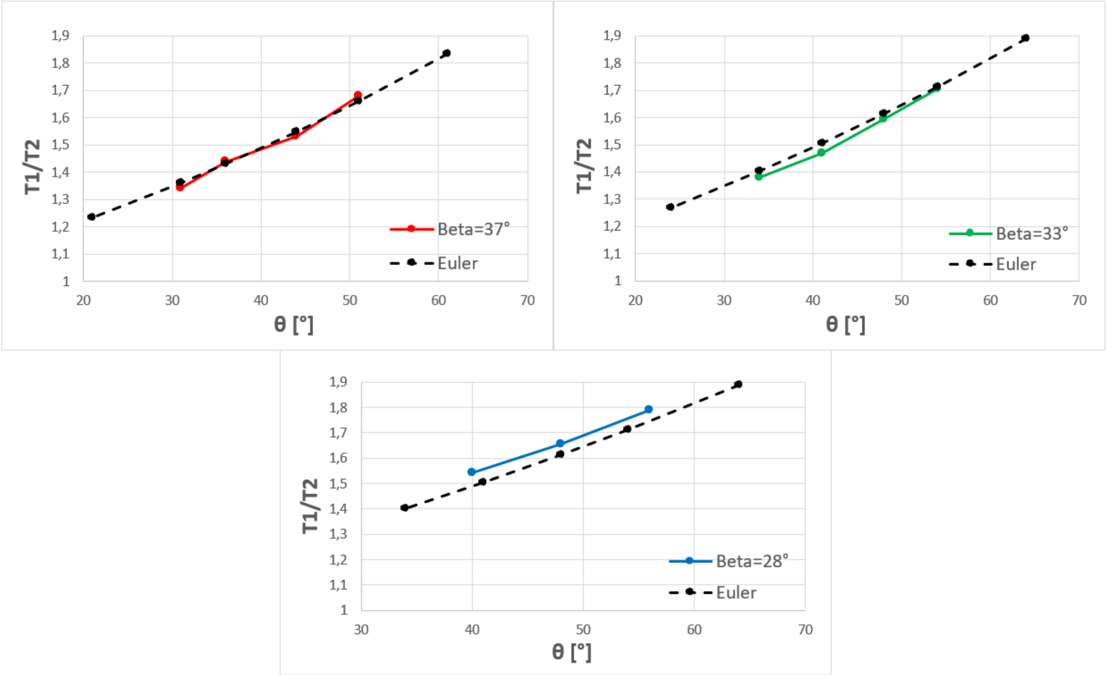

Figure 2.9: Euler model vs. tire patch experimental results.

2.6 Pneumatic tire over a step-obstacle

A series of tests have been carried out with a pneumatic tire trying to clear a step obstacle. The step height is 55 mm while the wheel radius is 140 mm. α and β at different tire pressures (from 1.2 to 2.5 bar) are measured and reported in Fig. 2.10. It is worth noticing that in order to measure α and β angles, a camera has been placed on the floor with its lens parallel to the tyre by using a laser meter to make the centre of the camera lens to be in the centre of the scene. The photos have been directly imported into Autodesk AutoCAD and the ‘scale’ command, based on known measurements, has been used to keep the appropriate dimensions. Finally, the main borders and edges have been traced in AutoCAD to

Figure 2.10: Tire trying to overcome a step a) pressure of 1.2 bar; b) pressure of 2.5 bar

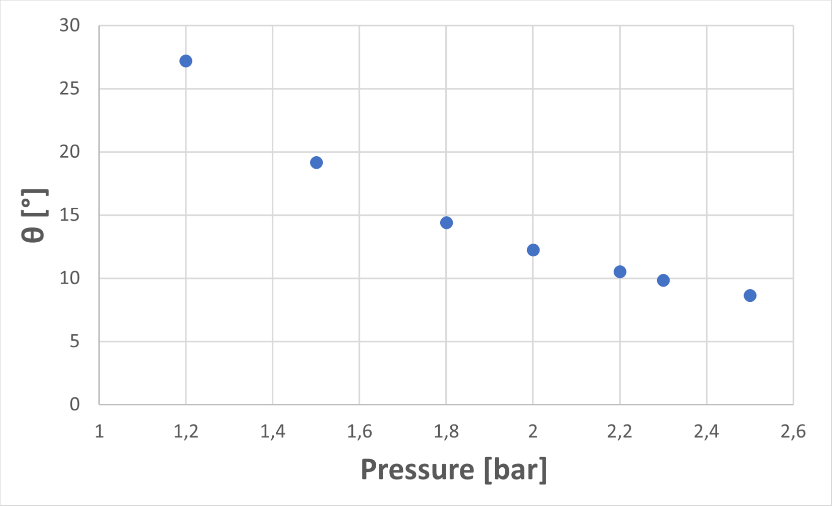

Figure 2.11: Values of the angles θ measured at different tire pressures

create a final DXF file containing only the references needed to properly measure the angles. Fig. 2.11 shows how the angle θ varies depending on the tire pressure. It can be calculated knowing α and β angles as

$$\theta = \frac{\pi}{2} - \alpha - \beta \tag{2.2}$$

In particular, it is higher for lower pressure values because α and β angles are smaller and the branches of the tires adhere more to the surface of the obstacle. As a result, the forces exchanged at the contact between tire and obstacle must be greater as described in Eq. 2.1. It follows that deflating a tire or facilitating its deflection can improve the capacity of a vehicle to climb up a step by increasing the contact forces exchanged with the ground. It can also be seen in [63] where low- and high-pressure tires are tested to compare their performance while facing step-like obstacles. In accordance with what we are saying, the authors state that low-pressure tires possess the improved ability to traverse step obstacles than high-pressure tires.

In accordance with Fig. 2.5, we suggest that the forces exchanged between the tire and the step are a force directed along the bisector of the two branches, called R_n and a force perpendicular to it (which depends on the coefficient of friction

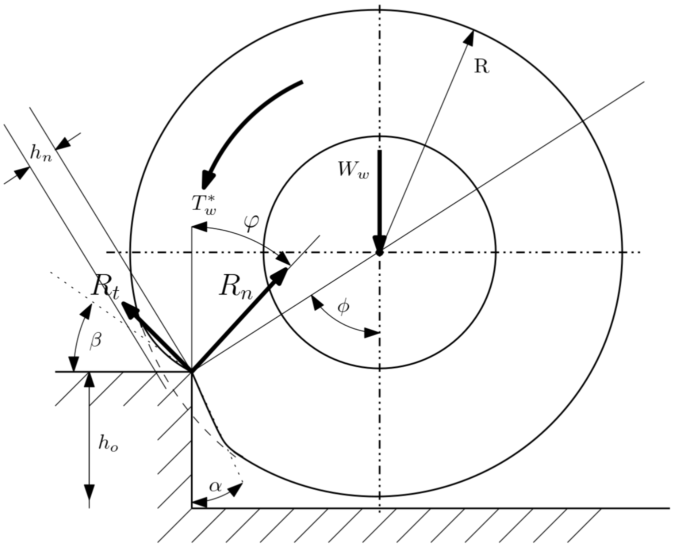

Figure 2.12: Wheel-obstacle interaction model

between the two bodies) called R_t (see Fig. 2.12). The φ angle is the angle that the force R_n forms with the vertical direction:

$$\varphi = \frac{\beta + \pi/2 - \alpha}{2} \tag{2.3}$$

Balancing the forces in Fig 2.12 we can say that

$$W_w sin(\varphi) = \mu R_n \tag{2.4}$$

$$W_w cos(\varphi) = R_n \tag{2.5}$$

then

$$tan(\varphi) = \mu \tag{2.6}$$

so the larger the angle φ, the higher the coefficient of friction. Therefore, the forces exchanged between the tire and the step depend on how the tire is deformed, i.e. the angles α and β, so it is important to determine these two angles.

2.7 Conclusion

This chapter aims to propose a rigorous analysis approach to study what happens when different kind of rubber belts or tires are in contact with a corner edge and what forces are exchanged between these two elements. A general introduction is given by mainly focusing on the scientific literature lack of a comprehensive wheel-obstacle contact model for the step-climbing problem. Then the importance of considering tire deformation has been emphasised and a novel approach to wheel-obstacle contact mechanics is given. A description of the test bench specifically developed for this work is provided along the experimental results for two cases of flat belt and tire patch that can be summarised as follows:

- the forces exchanged between a rubber belt and a corner edge depend on the relative angle θ between the two branches of the belt and on the friction coefficient.

- The forces exchanged between a tyre tread and a corner edge depend on the relative angle θ of the two tyre segments when it is pushed against the corner edge and the friction coefficient. The experimental tests showed how a pneumatic tyre patch behaves similarly to a belt when it is in contact with a step corner edge.

Following, the experimental results have been compared with Euler theoretical model to describe the behaviour of both tension $\frac{T_1}{T_2}$ while the relative angle θ changes its value. Figure 2.8 and Figure 2.9 allows to determine that the Euler model can be considered suitable for predicting what happens along the two branches of the belt when it is in contact with a corner edge. Moreover, it has been demonstrated that deflating a tire or facilitating its deflection can improve the capacity of a vehicle to climb up a step by increasing the contact forces exchanged with the ground.

Chapter 3

Development of a two-dimensional model and experimental tests of a deformable tire over a step-obstacle

The need to travel over rough terrain with a wheeled vehicle is a common occurrence, especially in non-urban environments [64]. However, the analysis of tire deformation during negotiation of a stepped obstacle remains an understudied problem and presents additional challenges to existing tire models [65]. In the previous Chapter it can be observed that the tire undergoes significant deformation near the contact with the corner edge, highlighting the importance of considering tire deformation in such contexts. This behavior is similarly observed in non-pneumatic wheels. The objective of this Chapter is to analyze the interaction between a deformable tire and a step-obstacle edge, deriving a theoretical model capable of calculating the deformation of the tyre when it is in contact with the step and verifying the results by comparison with experimental data. This Chapter is organized as follows: in Section 3.1 the experimental tests for step-obstacle negotiation are presented. Section 3.2 presents a two-dimensional model for both pneumatic and non-pneumatic tires. The solution procedures for non-pneumatic and pneumatic tires are provided in Sections 3.3 and 3.4, respectively. The results of the vertical force model are discussed in Section 3.5, while Section 3.6 reports the results of the step-obstacle model and compare it with the experimental data.

3.1 Step-obstacle experimental tests for pneumatic tire

A series of experimental tests have been conducted on a conventional pneumatic tire to evaluate its performance when negotiating a step-obstacle. These tests

Figure 3.1: Step-obstacle experimental tests

have been carried out in the mechanical engineering department laboratory of the Carlos III University, Madrid, in collaboration with collegues of the ADVANCED VEHICLE DYNAMICS AND MECHATRONIC SYSTEMS – VEDYMEC RESEARCH GROUP. A front-drive vehicle equipped with Dunlop P235/50 R18 97V tires was used for the experiments. A step-obstacle, with a width equal to the carriageway, was placed in front of the vehicle. The car was driven forward at low speed to traverse the obstacle. It has been assumed that the force exchanged between the tire and the step-obstacle acts in a perfectly vertical direction. Given that the vehicle is front-driven, the reaction force under the rear idler wheel was considered to have a vertical direction, as does the weight force. Consequently, the reaction force under the front-drive wheel was also assumed to act in a vertical direction

Images, such as the one shown in Fig. 3.1, were captured at the moment when the wheel lost contact with the ground, with its tread in contact solely with the corner edge, to document the tire deformation. From these images, with the same procedure used in the previous chapter, the angles α and β were measured for various step-obstacle heights and tire pressures, as presented in Figures 3.2 and 3.3, respectively.

The step-obstacle heights used in the tests were 50 mm, 65 mm, and 80 mm, while the tire pressures were set at 1.5, 2, 2.5, and 3 bar. Lower tire pressures resulted in greater adherence to the corner edge surface, which caused the β angle shown in Fig. 3.3 to decrease as the tire pressure decreased.

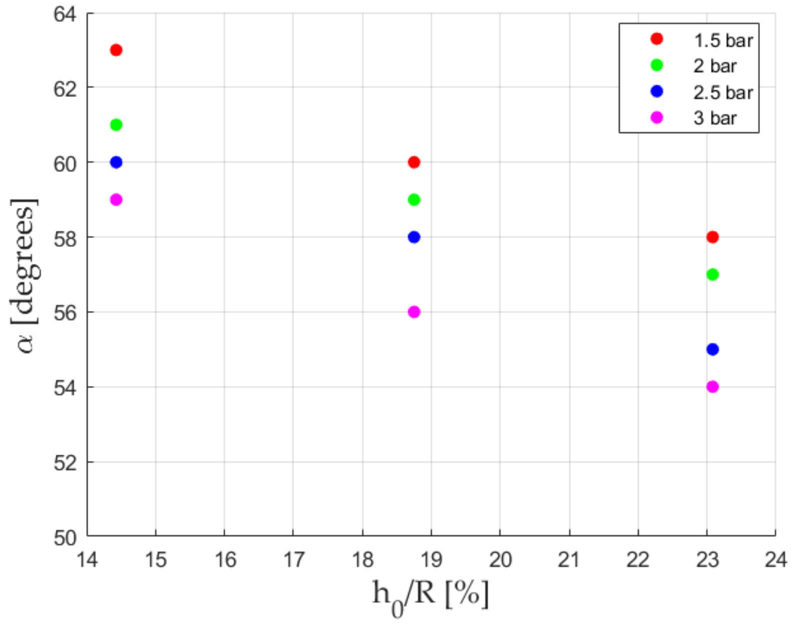

Figure 3.2: Angle between the tire's bottom branch and the corner edge

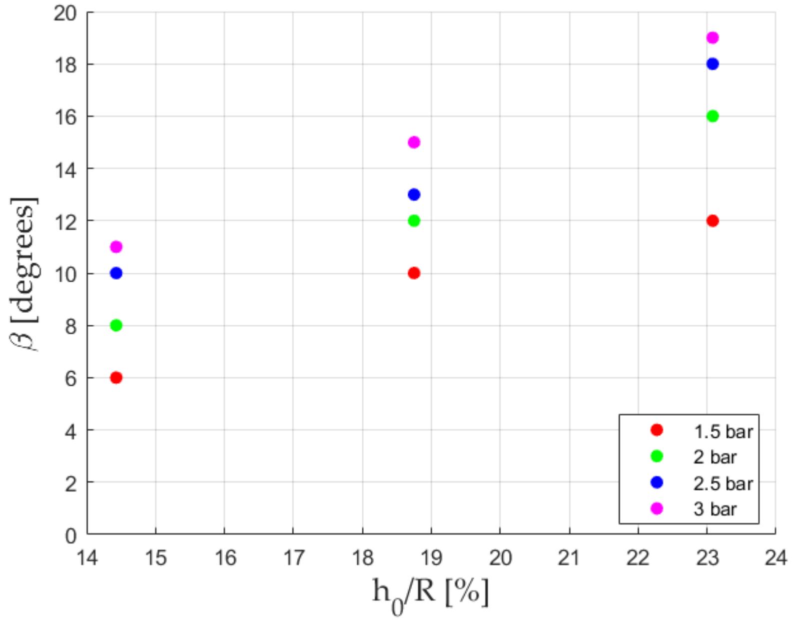

Figure 3.3: Angle between the tire's upper branch and the corner edge

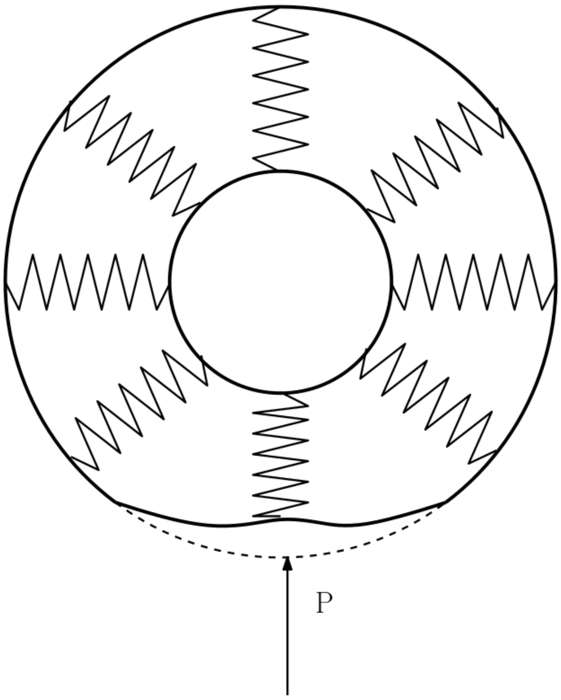

Figure 3.4: Circular beam model.

3.2 Analytical tire modeling

Considering the deformable tire facing a step-up obstacle, is needed to derive a theoretical model that calculates the tire tread deformation, specifically α and β. This model should take into account the tensions in the tire tread linking them to the tyre deformations. Then it would be possible to understand how the tension in the tread varies near the contact patch and derive a relationship between the tension in the tread of the tire and the vertical load applied to it.

During time many theoretical models have been developed to explain and/or understand tire behavior. These models range from those that predict the forces and moments generated at the contact between the tire and the ground, to models that focus on a particular physical phenomena that can occur in a loaded rolling tire. While most of them concern the pneumatic tire, and probably the best known is the Pacejka and Bakker work [66], few research has been published on non pneumatic tire models. [67] first develop a two-dimensional model of a compliant non-pneumatic tire. [68], using finite element model, investigate the static and dynamic behaviors of non-pneumatic tires with honeycomb spokes comparing its with traditional pneumatic tires.

For problems in which high frequency response are not of primary concern, a static circular beam model can be used. Figure 3.4, illustrates a classical tire representation, where the wheel is modeled with a circular beam and a series of radial springs connected to a rigid hub. The circular beam represents the tire tread while the radial springs inside the circular beam models the sidewalls. In regular operational conditions, such a wheel deforms primarily in its plane, the

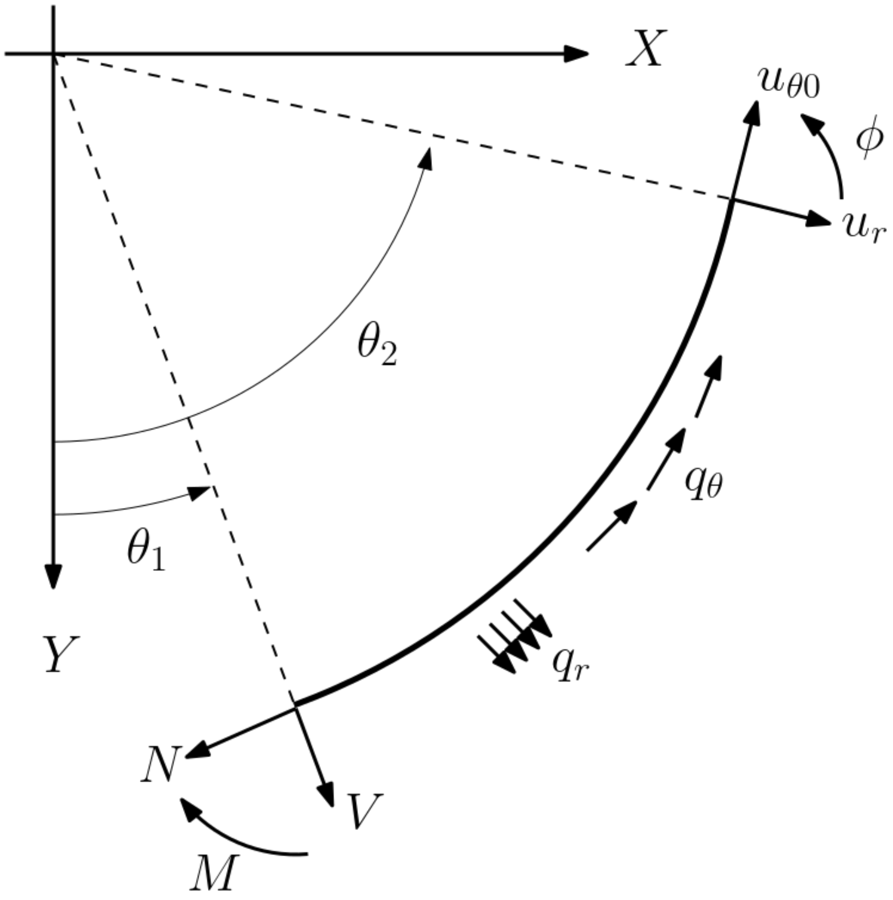

Figure 3.5: Uniformly curved beam: 1-D model for in plane deformation.

simplification from a three-dimensional to a two-dimensional structural analysis is assumed. Curvilinear beam theory taken from Belluzzi [69] can model the tire tread behavior where the contribution of normal stress is neglected. Due to a point load P at the bottom, the circular beam deforms and it is possible derive the radial deformation, the section rotation, the shear stresses and bending moment.

The Timoshenko circular beam is the simplest thin elastic continuum model that can account for the three primary deformation mechanisms of normal extension, normal bending and transverse shearing. Following Gasmi [70] cross-section of the beam rotates yet remains straight after deformation, which supposes uniform shear strain, and therefore shear stress, through the thickness. From this, it is assumed that the radial deformation of the ring, which is constant throughout the thickness of the ring, depends only on the angular coordinate. Second, because cross-sections may rotate, it is assumed that the circumferential deformation changes linearly through the thickness of the ring. Figure 3.5 illustrate the uniformly curved beam 1-D model for in plane deformation. If we consider that the radius of curvature R is much larger than the thickness h of the beam, it is possible to derive, taking inspiration from Gasmi [70], the approximate governing differential equation of a uniformly curved, extensional, Timoshenko beam as follows

$$
\begin{aligned}
EA\frac{d^2u_{\theta 0}}{d\theta^2} - GAu_{\theta 0} + (EA+GA)\frac{du_r}{d\theta} + RGA\phi &= -(R^2-R_c^2)bq_\theta \\
-GA\frac{d^2u_r}{d\theta^2} + EAu_r + (EA+GA)\frac{du_{\theta 0}}{d\theta} - RGA\frac{\phi}{d\theta} &= (R^2-R_c^2)bq_r \\
EJ\frac{d^2\phi}{d\theta^2} - R^2GA\phi - RGA\frac{du_r}{d\theta} + RGAu_{\theta 0} &= 0
\end{aligned}
\tag{3.1}
$$

In these equations EA is the circumferential stiffness, EJ is the bending stiffness, GA is the shear stiffness and the functions, $q_r(\theta)$ and $q_\theta(\theta)$, are respectively the radial and circumferential distributed loads applied at the mid-surface of the annular band. R_c refers to the rigid hub radius. The coupled differential equations 3.1 are subjected to the following exclusive essential/natural boundary conditions; either of which must be known at each edge of the beam:

$$
\begin{aligned}
u_r(\theta_i)/V(\theta_i) &= \frac{GA}{R}\left(\frac{du_r}{d\theta} - u_{\theta 0} + R\phi\right)\Bigg|_{\theta_i}, \\
u_{\theta 0}(\theta_i)/V(\theta_i) &= \frac{EA}{R}\left(\frac{du_{\theta 0}}{d\theta} + u_r\right)\Bigg|_{\theta_i}, \\
\phi(\theta_i)//M(\theta_i) &= \frac{EJ}{R}\left(\frac{d\phi}{d\theta}\right)\Bigg|_{\theta_i}; i = 1,2
\end{aligned}
\tag{3.2}
$$

In order to solve analytically the governing equations of the Timoshenko uniformly curved beam is convenient to decouple them into three independent differential equations

$$
\begin{aligned}
\frac{d^5u_r}{d\theta^5} + 2\frac{d^3u_r}{d\theta^3} + \frac{du_r}{d\theta} = {} & \frac{(R^2-R_c^2)b(R^2EA+EJ)}{EJEA}\frac{dq_r}{d\theta} \\
& - \frac{(R^2-R_c^2)b}{GA}\frac{d^3q_r}{d\theta^3} + \frac{(R^2-R_c^2)R^2b}{EJ}q_\theta \\
& - \frac{(R^2-R_c^2)b(EA+GA)}{GAEA}\frac{d^2q_\theta}{d\theta^2} \\[2ex]
\frac{du_{\theta 0}}{d\theta} = {} & -P\left(\frac{d^4u_r}{d\theta^4} + \frac{d^2u_r}{d\theta^2}\right) - u_r + \frac{(R^2-R_c^2)b}{EA}q_r \\
& - P\frac{(R^2-R_c^2)b}{GA}\frac{d^2q_r}{d\theta^2} - P\frac{(R^2-R_c^2)b(EA+GA)}{GAEA}\frac{dq_\theta}{d\theta} \\[2ex]
\phi = {} & \frac{1}{R}\left(u_{\theta 0} - \left(1+\frac{EA}{GA}\right)\frac{du_r}{d\theta}\right) - \frac{EA}{RGA}\frac{d^2u_{\theta 0}}{d\theta^2} - \frac{(R^2-R_c^2)b}{RGA}q_\theta
\end{aligned}
\tag{3.3}
$$

where the constant

$$
P = \frac{EJGA}{R^2EAGA + EJGA + EJEA}
$$

3.3 Solution procedure for non-pneumatic tire

Since the tire is non-pneumatic, there is no effect of internal air pressure. Additionally circumferential stiffness is neglected given the wheel structure design. Substituting the spring relationship into decoupled governing differential equations

$$q_r = -\frac{K_r u_r}{b} \tag{3.4}$$

we obtain

$$\begin{aligned}
\frac{d^5 u_r}{d\theta^5} + 2\frac{d^3 u_r}{d\theta^3} + \frac{du_r}{d\theta} = -\frac{(R^2 - R_c^2)(R^2 EA + EJ)}{EJEA} K_r \frac{du_r}{d\theta} \\
+ \frac{(R^2 - R_c^2)}{GA} K_r \frac{d^3 u_r}{d\theta^3}
\end{aligned}$$

$$\begin{aligned}
\frac{du_{\theta 0}}{d\theta} = -P\left(\frac{d^4 u_r}{d\theta^4} + \frac{d^2 u_r}{d\theta^2}\right) - \left(1 + \frac{(R^2 - R_c^2)}{EA} K_r\right) u_r \\
+ P\frac{(R^2 - R_c^2)}{GA} K_r \frac{d^2 u_r}{d\theta^2} \qquad (3.5) \\
\phi = \frac{1}{R}\left(u_{\theta 0} - \left(1 + \frac{EA}{GA}\right)\frac{du_r}{d\theta}\right) - \frac{EA}{RGA}\frac{d^2 u_{\theta 0}}{d\theta^2}
\end{aligned}$$

After analytically finding the function $u_r(\theta)$ from the first equation of 3.5 is possible determine $u_{\theta 0}(\theta)$, $\phi(\theta)$, $N(\theta)$, $V(\theta)$, $M(\theta)$. These functions depend on the constants $(C_i)_{1 \le i \le 6}$ which must be determined by imposing boundary conditions.

3.4 Solution procedure for pneumatic tire

Since the tire is pneumatic, the effect of internal air pressure must be considered. Substituting the spring relationship into decoupled governing differential equations

$$q_\theta = -\frac{K_\theta u_{\theta 0}}{b} \qquad q_r = -\frac{K_r u_r}{b} \tag{3.6}$$

where the radial stiffness can be related to internal air pressure using the following equation

$$K_r = k_1 p \tag{3.7}$$

we obtain

$$\begin{aligned}
\frac{d^6 u_r}{d\theta^6} + 2\frac{d^4 u_r}{d\theta^4} + \frac{d^2 u_r}{d\theta^2} = -\frac{(R^2 - R_c^2)(R^2 EA + EJ)}{EJEA} K_r \frac{d^2 u_r}{d\theta^2} \\
+ \frac{(R^2 - R_c^2)}{GA} K_r \frac{d^4 u_r}{d\theta^4} - \frac{(R^2 - R_c^2)R^2}{EJ} K_\theta D_1 \\
+ \frac{(R^2 - R_c^2)(EA + GA)}{GAEA} K_\theta D_3
\end{aligned}$$

$$\begin{aligned}\frac{du_{\theta 0}}{d\theta} &= -P\left(\frac{d^4u_r}{d\theta^4}+\frac{d^2u_r}{d\theta^2}\right)-\left(1+\frac{(R^2-R_c^2)K_r}{EA}\right)u_r \\ &\quad + P\frac{(R^2-R_c^2)K_r}{GA}\frac{d^2u_r}{d\theta^2}+P\frac{(R^2-R_c^2)(EA+GA)}{GAEA}K_\theta\frac{du_{\theta 0}}{d\theta} \\ \phi &= \frac{1}{R}\left(u_{\theta 0}-\left(1+\frac{EA}{GA}\right)\frac{du_r}{d\theta}\right)-\frac{EA}{RGA}\frac{d^2u_{\theta 0}}{d\theta^2}+\frac{(R^2-R_c^2)K_\theta}{RGA}u_{\theta 0}\end{aligned} \tag{3.8}$$

where

$$D_1 = \frac{-P\left(\frac{d^4u_r}{d\theta^4}+\frac{d^2u_r}{d\theta^2}\right)-\left(1+\frac{(R^2-R_c^2)}{EA}K_r\right)u_r+P\frac{(R^2-R_c^2)}{GA}K_r\frac{d^2u_r}{d\theta^2}}{1-P\frac{(R^2-R_c^2)(EA+GA)}{GAEA}K_\theta}$$

$$D_3 = \frac{-P\left(\frac{d^6u_r}{d\theta^6}+\frac{d^4u_r}{d\theta^4}\right)-\left(1+\frac{(R^2-R_c^2)}{EA}K_r\right)\frac{d^2u_r}{d\theta^2}+P\frac{(R^2-R_c^2)}{GA}K_r\frac{d^4u_r}{d\theta^4}}{1-P\frac{(R^2-R_c^2)(EA+GA)}{GAEA}K_\theta}$$

After analytically finding the function $u_r(\theta)$ from the first equation of 3.8 is possible determine $u_{\theta 0}(\theta)$, $\phi(\theta)$, $N(\theta)$, $V(\theta)$, $M(\theta)$. These functions depend on the constants $(C_i)_{1\leq i\leq 7}$ which must be determined by imposing boundary conditions. Finally the pressure contribution to the solution is added as:

$$N(\theta) = Rpb+\frac{EA}{R}\left(\frac{du_{\theta 0}}{d\theta}+u_r\right)$$

and

$$u_r(\theta) = u_{r0}+u_r(\theta)$$

where u_{r0} is

$$u_{r0} = \frac{R^2pb}{EA+K_{press}R^2}$$

and K_{press} is the tension radial sidewall stiffness.

3.5 Vertical force model results for pneumatic tires

Sensor-embedded pneumatic tires, commonly referred to as intelligent tires, are capable of providing reliable and essential information regarding tire-road contact characteristics, such as slip, forces, and tire deformation. Sensor measurements from intelligent pneumatic tires, including radial and tangential tread deformations [71] and tire strain time histories [72], are considered in the analysis.

Considering a pneumatic tire subjected to a pure vertical load, the results obtained from the proposed analytical model are presented. The tire used in the

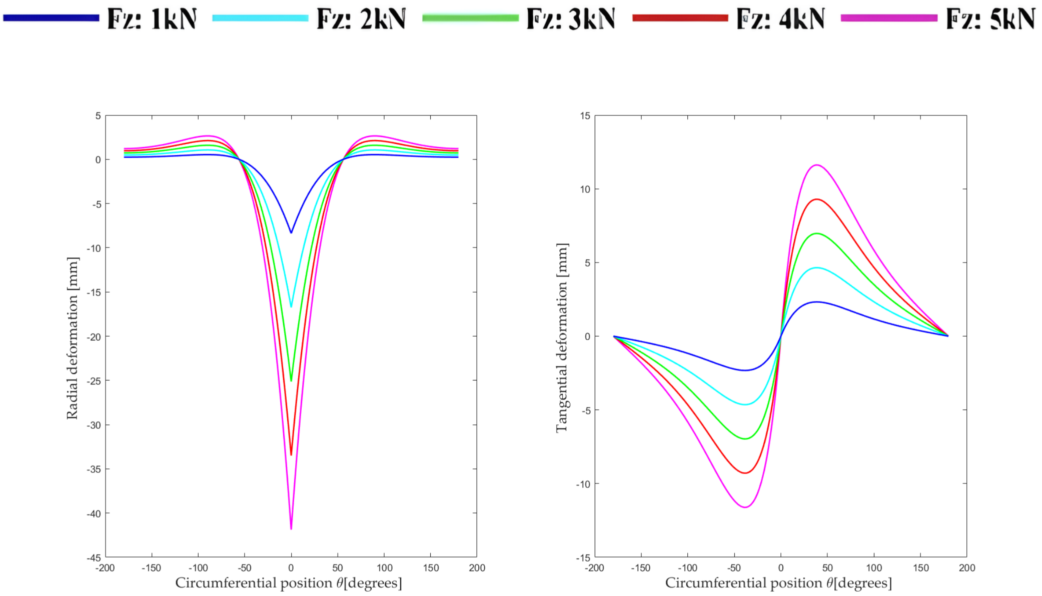

Figure 3.6: In-plane tire deformations under different vertical forces: (left) radial deformations and (right) tangential deformations

Description	Units	Value
EA	N	$2.7 \cdot 10^4$
EJ	$N \cdot mm^2$	$2.88 \cdot 10^8$
Poisson's ratio	–	0.3
k_1	–	0.4

Table 3.1: Model parameters

experimental tests outlined in Section 3.1 (Dunlop P235/50 R18 97V) is considered, and the model parameters are shown in Table 3.1. A tire pressure of 2 bar is assumed for the calculations.

Figure 3.6 presents the radial and tangential deformations at different circumferential positions under varying vertical forces. It is observed that both types of deformation are symmetric with respect to the center of the tire's contact patch.

The ideal strain time histories, measured along the circumferential (longitudinal) and axial (lateral) directions of the inner liner surface of the tire tread during one full revolution under steady-state, straight-line rolling, are depicted in Fig. 3.7.

The strain waveform exhibits near symmetry with respect to the center of the tire contact patch, due to the absence of braking, traction, or steering forces. Tensile strain occurs within the contact patch (region between points B and D), with the peak occurring at the center (point C). Compressive strain is observed in the leading and trailing regions outside the contact patch. Therefore, the tread element experiences compression before entering and after exiting the contact patch,

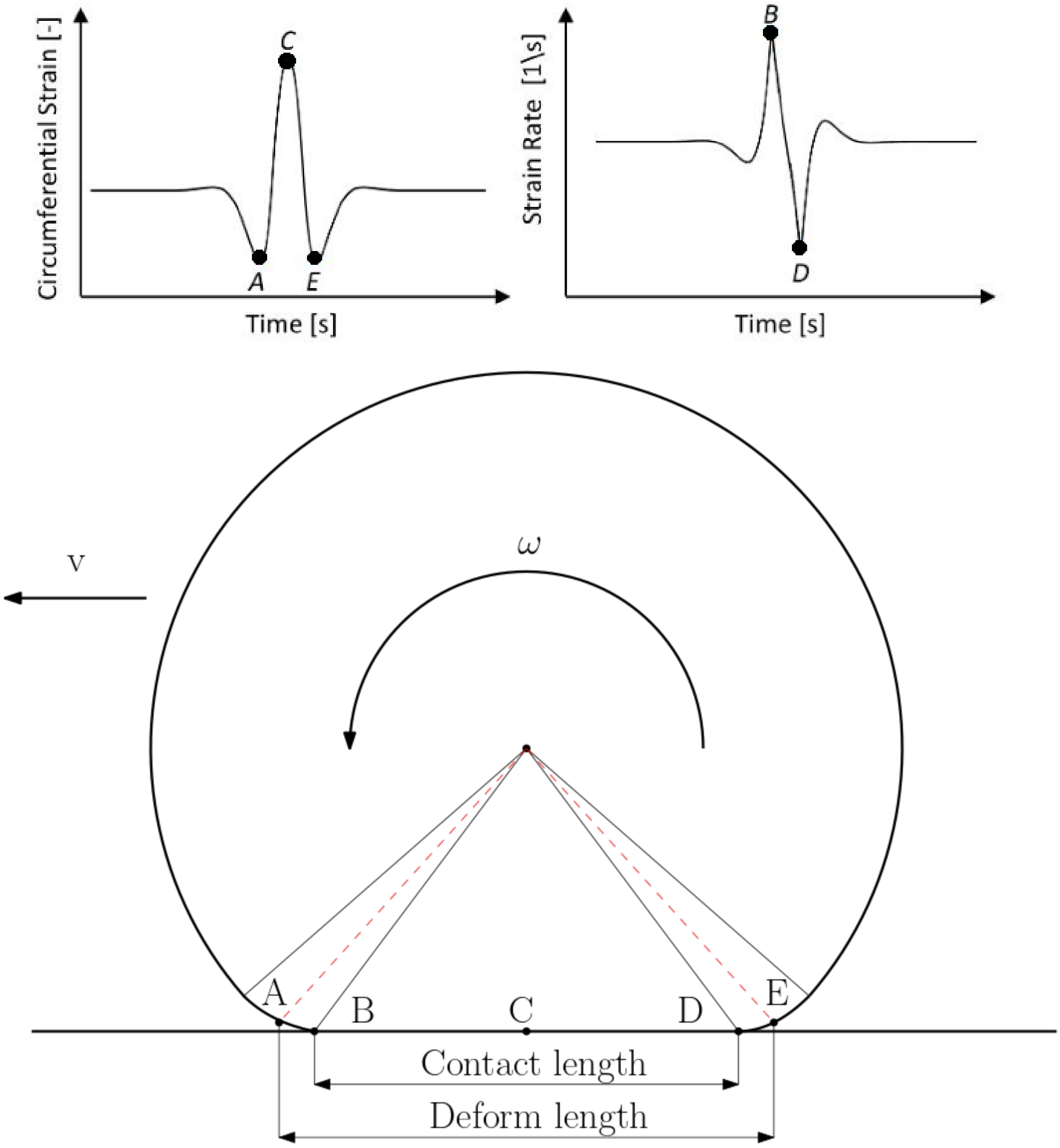

Figure 3.7: Characteristics of tire strain time history

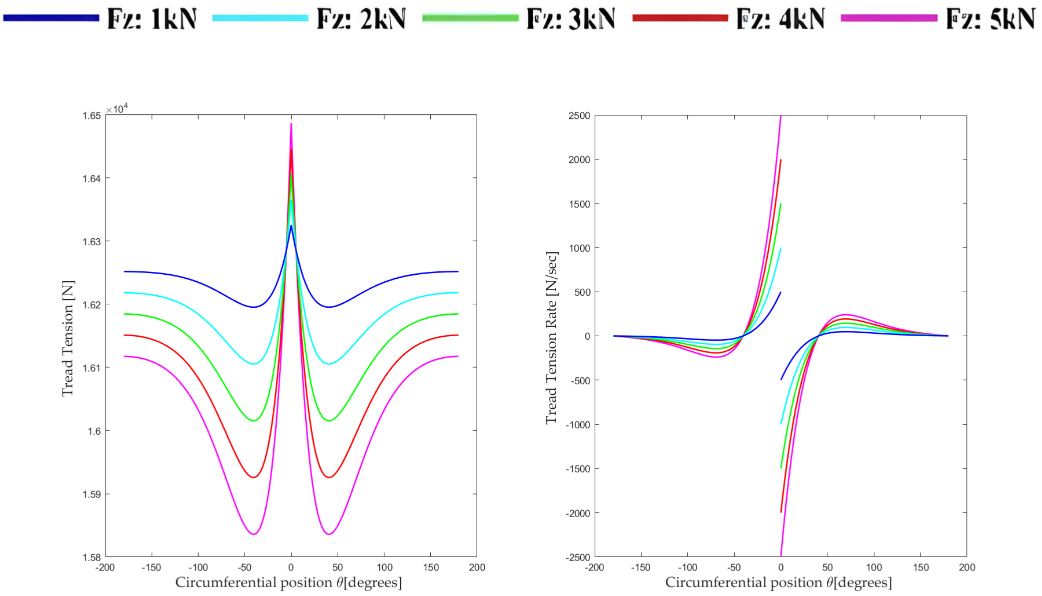

Figure 3.8: Characteristics of tire tension time history: (left) tread tension and (right) tread tension rate

and is subjected to stretching within the patch during steady-state rolling.

The time derivative of circumferential strain, shown in Figure 3.7, displays two peaks corresponding to the leading and trailing edges of the tire contact patch. The time interval between these peaks, representing points B and D, reflects the time required to traverse the contact length between these two points.

The circumferential strain in the tire arises from the normal forces acting on the tire tread. Consequently, the tire tension time history derived from the analytical model is presented in Fig. 3.8.

3.6 Step-obstacle interaction model results for pneumatic tire

Figure 2.3 illustrates the step-obstacle problem to be analyzed. Since the contact force between the tire and the step-obstacle is assumed to be vertical, as justified in Section 3.1, the hub force is also assumed to be vertical. A point load approximation is utilized due to the characteristics of the contact region between the tire and the corner edge of the step-obstacle. The tire used in the experimental tests of Section 3.1 (P235/50 R18 97V) is employed in this analysis, and the model parameters are identical to those in Section 3.5.

The technical specifications of the vehicle used in the experimental tests are reported in Table 3.2.

Assuming the center of mass is located at the vehicle's center, a vertical force of 7663 N is considered in the model to replicate the test conditions.

Description	Units	Value
total length	mm	4300
front overhang	mm	880
rear overhang	mm	770
total mass	kg	1500

Table 3.2: Vehicle technical specification

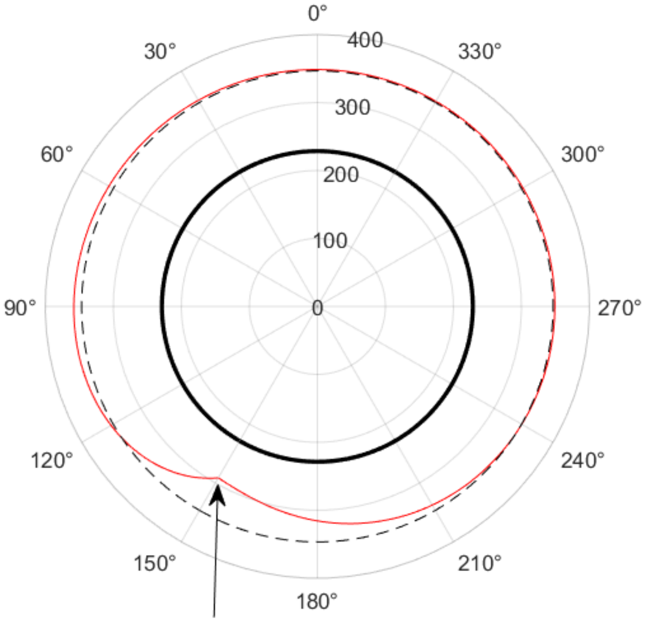

Figure 3.9: Pneumatic tire tread deformation

The outputs of the analysis include the tire deflection between the treads and the corner edge, specifically the α and β angles, and the tread tensions close to the contact zone.

Figure 3.9 shows the pneumatic tire deformation when encountering a step-obstacle with a height equal to 13.5 percent of the wheel radius, at 2 bar pressure. The blacked-out line circle represents the rigid wheel hub. When compared with figures in the literature (Fig. 2.2), it can be seen that the deformation better represents what occurs when a pneumatic tire encounters a step-obstacle.

Figure 3.10 depicts the tread tension across the tire, highlighting the influence of internal pressure. The internal air pressure causes the tread tension values to remain positive. However, it can be observed that the tire behaves differently on either side of the step-obstacle: the upstream region is compressed, while the downstream region experiences extension.

An analysis of variable obstacle heights for the pneumatic tire is conducted to compare experimental data with the analytical model results. Figure 3.11 presents the calculated angles between the tire bottom branch and the corner edge, as shown

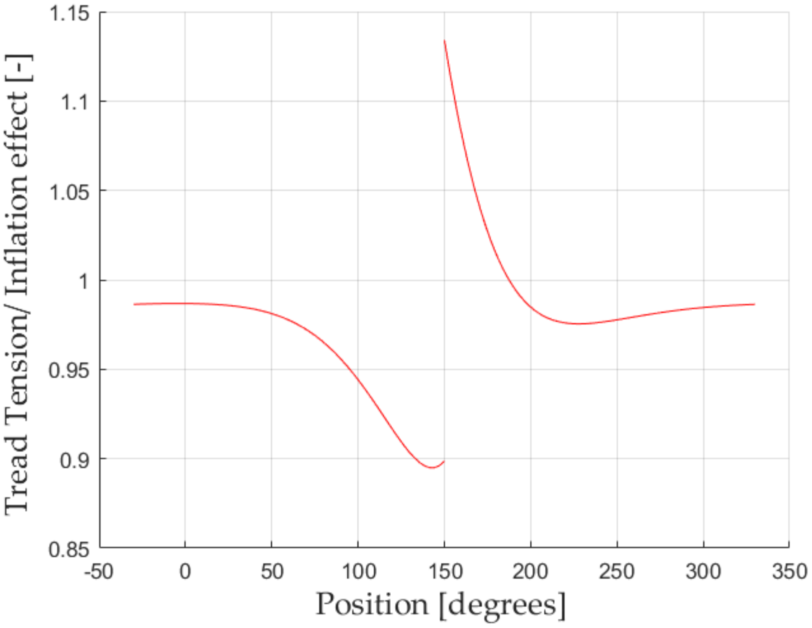

Figure 3.10: Pneumatic tire tread tension

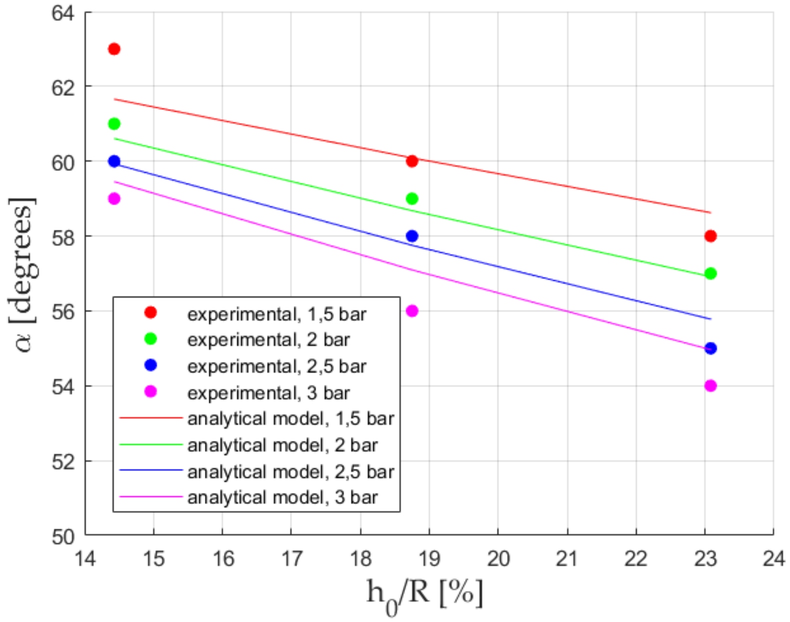

Figure 3.11: Angle between the tire bottom branch and the corner edge

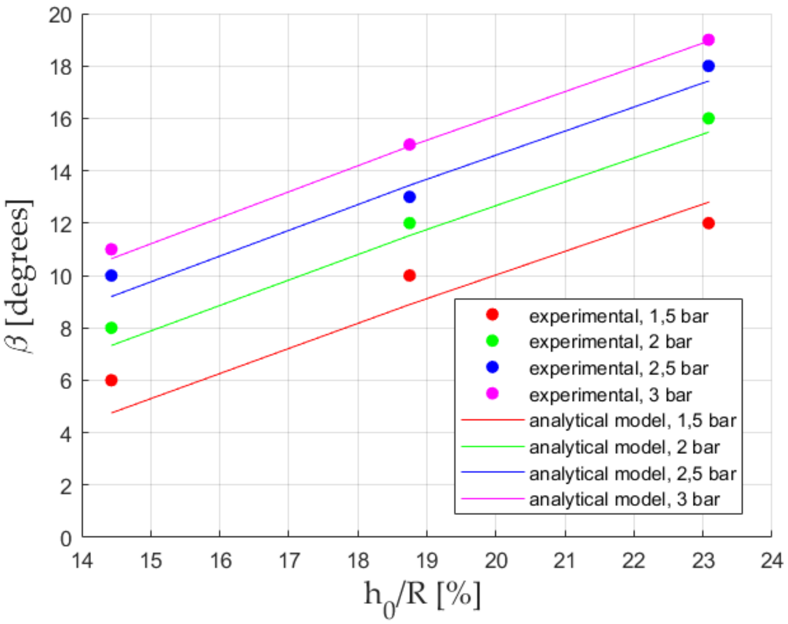

Figure 3.12: Angle between the tire upper branch and the corner edge

in Figure 2.3, for various tire pressures. The results are also compared with experimental data in the same figure. Figure 3.12 shows the calculated angles between the tire upper branch and the corner edge under similar conditions, with a comparison to the experimental data. The results indicate a strong correlation between the two datasets. Lower tire pressures result in smaller β angles, suggesting that the compressed portion of the tire upstream adheres more closely to the surface of the step.

Figure 3.13 presents the required friction coefficient, calculated using the equations shown in the previous Chapter, as a function of tire pressure for varying obstacle heights. It is observed that for deflated tires, the required friction coefficient between the tire and the step-obstacle is lower. This suggests that deflating a tire or facilitating its deflection can enhance the vehicle's ability to traverse a step by increasing the contact forces exchanged with the ground. This observation aligns with the findings of [63], where low- and high-pressure tires are tested to compare their performance when facing step-like obstacles. The authors similarly conclude that low-pressure tires exhibit improved performance in traversing step obstacles compared to high-pressure tires.

3.7 Conclusions

This chapter presents experimental results on the behavior of a conventional pneumatic tire clearing a step-obstacle, alongside an analytical model developed to analyze the interaction between a deformable tire and the corner edge of a step-obstacle.

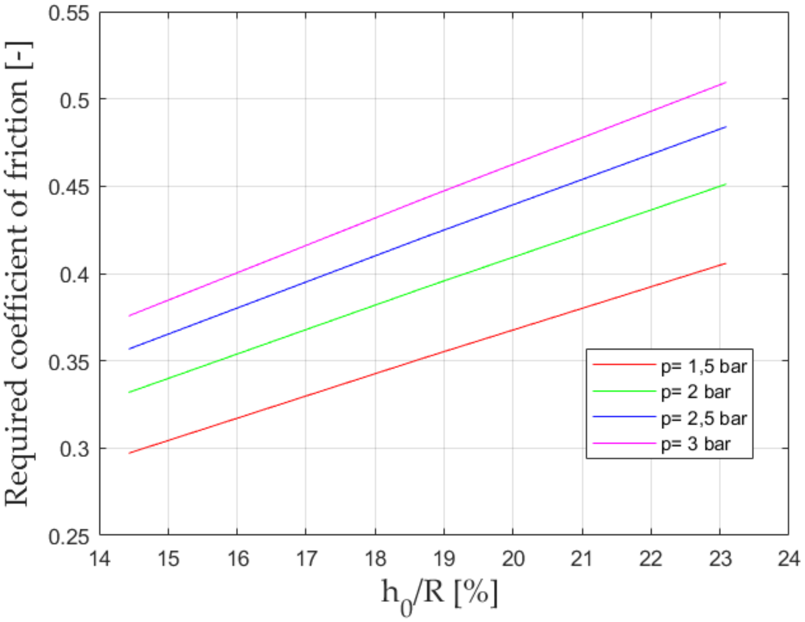

Figure 3.13: Required coefficient of friction to clear the obstacle

Two-dimensional models for both non-pneumatic and pneumatic tires are formulated. The non-pneumatic tire model consists of a thin, flexible annular band, supported by springs that connect the band to a rigid hub. The pneumatic tire model extends this by incorporating the effects of tangential springs and internal pressure. Timoshenko's curved beam theory is employed to model the annular band, accounting for deformations due to bending, shearing, and circumferential extension. Governing differential equations are derived for both non-pneumatic and pneumatic tire cases.

The results of the in-plane deformation model for different vertical forces are discussed, as well as the characteristics of tread tension. This approach follows the standard methodology for analyzing strain-based intelligent tires under flat ground loading conditions. Additionally, model results for the interaction between the tire and a step-obstacle are presented, with a particular focus on tire tread deformation.

The model's predictions are compared with experimental data, demonstrating a good agreement between the two. The analysis for pneumatic tires also highlights the effect of pressure on the ability to overcome a step-obstacle, showing that tires with lower pressure can clear greater obstacle heights.

Chapter 4

Design and Analysis of a tracked stair-climbing robot using innovative suspension system

Today, ground mobile robots are used in a multitude of field and for performing multiple tasks and operations. In the coming years, their use will certainly become even more widespread. Overcoming a series of steps using mobile robots is a complicated challenge. The locomotion system design of stair-climbing robot is generally more complex because of the wide range of situations that can potentially be encountered.

There are three main type of locomotion systems: wheeled robots (W), tracked robots (T) and legged robots (L). Hybrid robots are a combination of the previous classes: legs-wheels (LW), legs-tracks (LT), wheels-tracks (WT), and legs-wheels-tracks (LWT) [5].

Wheeled robots, controlling a few active degrees of freedom (DOFs), can achieve high speeds on flat ground with low power consumption. Unfortunately they have limited ability to overcome a series of steps obstacles [6]. "HELIOS-V" [41] is a 6-wheeled vehicle equipped with 4 low-pressure tires on the outside and 2 high-pressure tires on the inside. [21] deals with two wheeled vehicle with an inverted pendulum layout used for personal transportation. Krys [53] has special wheels that can easily go up and down stairs without wobbling. Rocker-bogie [73] also has special structures that help it move well in difficult environments.

Tracked robots are capable of overcome obstacles but they have high power consuption than wheeled robots. Tracked robots can have non-articulated tracks or articulated tracks. Very simple mechanics and controls characterise robots with non-articulated tracks. Despite their simplicity, they move well over obstacles. Example of this scheme is Yoneda [42], a stair-climbing crawler with high gripping force on the stairs. To improve the capacity to overcome obstacles, more than two tracks with relative passive mobility can be adopted [74]. For example ROBHAZ-DT3 [75] track is splitted in two parts. TAQT Carrier [44], Silver [76] and Macbot [77] posses front and rear moving flippers to go up the stairs.

Legged robots are machines that have legs like humans and animals. These robots are able to go over different kinds of obstacles by copying how humans and animals walk up stairs using their legs and feet. However, they are slow and have very high power consuption. Example of legged robots are WL-16 II [32,33], Lee [29], ANYmal [78] and RHex [79].

Hybrid locomotion systems are like trying to combine the best parts of different ways of moving, while trying to avoid the not-so-good parts. Leg-wheel robots combine the energy efficiency of wheels with the operative flexibility of legs [80]. Three-wheeled locomotion unit geometry, that means it can move well on bumpy ground and can climb over things easily, is adopted in the Epi.q mobile robots family [81]. Ascento [82] is a small robot with wheels and legs that can move fast on flat ground and jump over things that are in its way. Zero Carrier [27,28] is a machine that has legs with chains and wheels on the end. Some of the legs move to help the machine move forward, while others just have wheels. RT-Mover PType WA [38–40] has legs that look like axles and a seat that can move back and forth. It also has wheels on the ends of the legs. Morales [36] and Lawn [37] use special supports to lift the machine and then put the wheels on a new surface.

Hybrid mobile robots with legs and tracks, used in unstructured environments, demonstrate that speed and energy efficiency are not crucial. Titan X [83] is a quadruped mobile robot with three DOFs per leg. The four belts have a double function: mechanical transmission for actuation of the knee joints during legged locomotion, and tracks during tracked locomotion.

In wheel-track hybrid robots, the relative position of the tracks and wheels or the track shape can usually be changed to enable or disable wheel contact with the ground. Wheels and tracks combination is used to achieve stair-climbing task combined with energy efficiency on flat ground. For example All-Terrain Wheelchair [15] use wheels on flat ground while the tracks are hidden under the carriage. When something is in the way, the tracks on a vehicle can be moved down to the ground while the wheels come off the ground. This helps the vehicle go over the obstacle without getting stuck. Helios-VI [43] has two active arms attached to the axis of the one drive pulley of the active crawler. One of the arms has two tires on the end to help the vehicle move better on bumpy ground. The other arm can carry things and change how the things are positioned.

The WheTLHLoc [84] is an example of a robotic platform that combines all three types of locomotion. It is characterized by a main body equipped with actuated wheels and two protruded structures to allow for climbing stairs. Azimuth [52] is fitted with four independent leg-track-wheel articulations which can generate a wide variety of locomotion modes. Wheelchair.q [22,25] is made up of two parts that help it move, and it also has a special part in the back that keeps it stable.

In chapter 1 it has been highlighted as tracked robots perform better than others the task of carrying a load up a flight of stairs [54]. These because they combine good overall performance and good transport ability with low mechanical complexity, simple control strategy and low construction cost. Considering this, it is decided to design a tracked stair-climbing robot capable of safely and effectively climb a flight of stairs.

How then to design a new tracked robot? First of all, one must choose if road wheels are fixed respect to the robot body or not. The first group is very basic in how they move, so they are not very good at getting around obstacles. So we opted for a robot whose road wheels can move relative to the body of the vehicle. This category of platforms can have passive suspension system or active suspension system. The passive suspension system for tracked robots is chosen because it combines mechanical simplicity with the ability to adapt the system layout to the ground shape of unstructured environments. The basic design for tracked vehicle usually has wheels connected to the body with springs or dampers that allow them to move easily. Inspired to tank suspension design, Yutan Li et al. [85] develop a christie suspension spring loaded with shock absorbers robot. Another example of passively suspension system can be found in [86]. Sun and Jing develop a tracked robot with novel bio-inspired passive "legs" adapting the track shape to different environments scenarios. Also the all-terrain rover Polibot [87] use a novel passively suspension system to adapt the rubber track to terrain irregularities and distribute the pressure evenly under all conditions.

In [87] we created a special model that helps us figure out how a system will move based on the shape of the ground it's on. In the same article, the effectiveness of this model was demonstrated, verifying an excellent comparison between the experimental results and those of the model. So we modify and use it as a tool to broadly design the new tracked robot by giving the profile of a flight of stairs as the ground geometry and iteratively testing how the system was configured. This represents a novelty because such a model had never before been used as a basis for the design of a new tracked robot. To verify that the resulted design can effectively climb a flight of stairs, dynamic simulation is carried out. Then the design of a new robot capable of climbing a flight of stairs is conceived.

The chapter is divided into different sections. In Section 4.1, the "XXbot" concept is presented, robot design is outlined, especially the working principle of passive swing arms. Section 4.2 and 4.3 described the inverse kinematic model for the proposed architecture. Stair-climbing simulation are made with the multibody sotware MSC-Adams and results are presented in Section 4.4.

4.1 XXbot

The fundamental idea behind the "XXbot" is to design a tracked robot that can adapt the track to the staircase supporting surface profile. The "XXbot" concept is shown in Fig. 4.1. Its name comes from the double-X shape of the suspensions. The two tracks have articulated passive suspension systems that include two central bogie-like suspensions and swing arm suspensions on the front and rear side of the robot. This suspension system guarantees a very high adaptability of the track to the shape of the support surface, both on the negotiation of obstacles and on a flight of stairs.

Table 4.1 lists the different components of the system. Referring to the left track, the weight of the vehicle is spread evenly on the ground through the six wheels. Each wheel is attached to the frame SF with a swingarm and a spring

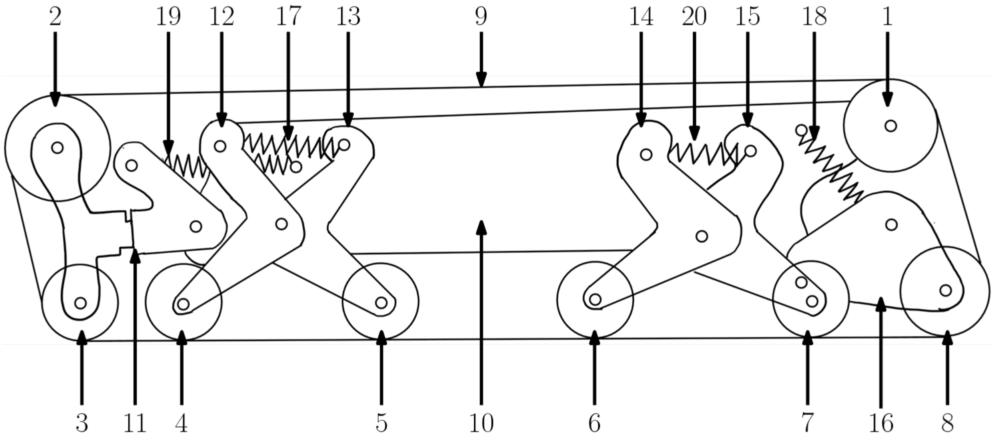

Figure 4.1: XXbot robot concept.

element. This allows the wheels to move and adjust to the shape of the ground. Moreover, the two central bogie-like suspensions give the system even more adaptability. They distribute the weight of the robot over the central ground wheels that ensure the contact of the track with the supporting surface. W_4 and W_5 are hinged and connected to each other through a spring. In the same way, W_6 and W_7 are hinged to form the second central bogie-like suspension. Finally, the subframe SF that accommodates the drive sprocket W_1.

4.2 Analytical model

To evaluate the feasibility and performance of the "XXbot", an analytical model is needed. In this part, we will figure out how to move the rover and adjust its suspension system based on the shape of the ground it's driving on. To do this, we need to first understand how wheels touch the ground. For vehicles with tracks, it can be tricky to figure out. But for now, let's pretend that the tracks are very thin and don't make much of a difference. Then, each wheel on the ground touches the ground at just one point, denoted with $CP_i, i = 3..., 8$ to match the road wheels numbering. When you walk up or down stairs, it's safe to assume that the stairs will be sturdy and won't break.

The model inputs are the geometric parameters of the suspension, the map of elevation for the supporting surface, the position of the first contact point (CP_3) on the map, the length of the track, the weight of the robot and the position of the center of gravity of the robot. The output of the model are the body position and tilt along with the suspension configuration.

4.2.1 Degrees of freedom

A global reference frame $X_gY_gZ_g$ and a vehicle reference frame $X_vY_vZ_v$ are defined in Fig. 4.2. For simplicity we assume half symmetry model. In this case, the $X_g - Z_g$ plane contains the vehicle center of mass. The model not include roll and

Table 4.1: Main components of the robot.

Item number	**Description**	**Symbol**
1	Sprocket	W_1
2	Idler wheel	W_2
3	Ground wheel	W_3
4	Ground wheel	W_4
5	Ground wheel	W_5
6	Ground wheel	W_6
7	Ground wheel	W_7
8	Ground wheel	W_8
9	Track	-
10	Subframe	SF
11	Front Swing Arm	FSA
12	Bogie arm Front-Front	BFF
13	Bogie arm Front-Rear	BFR
14	Bogie arm Rear-Front	BRF
15	Bogie arm Rear-Rear	BRR
16	Rear Swing Arm	RSA
17	sring-damper	S_1
18	spring-damper	S_2
19	spring-damper	S_3
20	spring-damper	S_4

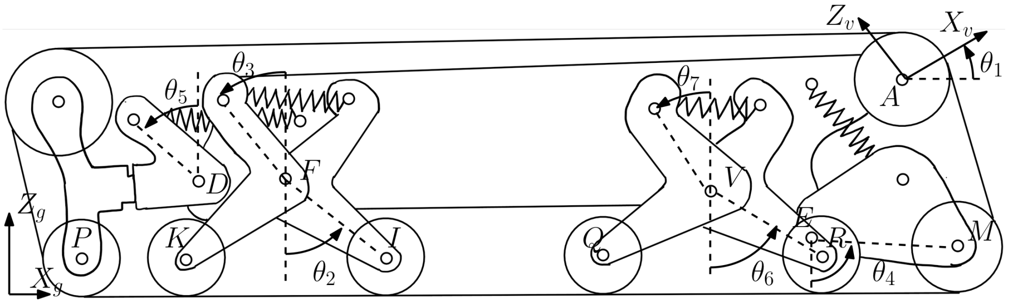

Figure 4.2: Reference frames and degrees of freedom.

Table 4.2: Degrees of freedom of the system (please refer to Fig. 4.2)

Number	Description	Symbol
1	Vertical position of A (global ref. frame)	x_A
2	Horizontal position of A (global ref. frame)	y_A
3	Pitch of SF (robot's pitch)	θ_1
4	Orientation of BFR relative to joint F	θ_2
5	Orientation of BFF relative to joint F	θ_3
6	Orientation of RSA relative to joint E	θ_4
7	Orientation of FSA relative to joint D	θ_5
8	Orientation of BRR relative to joint V	θ_6
9	Orientation of BRF relative to joint V	θ_7

yaw rotations (φ and ψ) but only pitch movements (θ).

Moreover, in the model it is assumed that the wheels touch the surface at their lowest point and that the normal forces pass through the center of them. In fact, the goal of the analytical approach created is to compute the quasi-static kinematic model of the suspension to solve inverse kinematic problems. This means figuring out how the robot is set up based on where the wheels touch the ground.

The system of Fig. 4.2 consists of seven rigid bodies (six are the suspension elements and the seventh rigid body is the vehicle frame) connected by four revolute joints located in D,F,V and E points. Table 4.2 reports the resulting nine DOFs.

4.2.2 Constraints

The support surface elevation map can be represented by the following expression:

$$Z = f_{te}(X) \tag{4.1}$$

where f_{te} is a function that gives the height of the support surface (Z) for any value of X.

Referring to the schematics of Fig. 4.2, if we know where the first point of contact is on the X-axis and imagine that the wheels touch the ground at their lowest point, we can use these equations to describe how they are connected:

$$X_P = X_{CP3} \tag{4.2}$$
$$Z_P - r_3 = f_{te}(X_P) \tag{4.3}$$
$$Z_K - r_4 = f_{te}(X_K) \tag{4.4}$$
$$Z_I - r_5 = f_{te}(X_I) \tag{4.5}$$
$$Z_Q - r_6 = f_{te}(X_Q) \tag{4.6}$$
$$Z_R - r_7 = f_{te}(X_R) \tag{4.7}$$
$$Z_M - r_8 = f_{te}(X_M) \tag{4.8}$$

where r_i is the radius of wheel i. Given the geometry of the suspension (Fig. 4.1), the coordinates of the wheel centers (P, K, I, Q, R and M) can be expressed, in the vehicle reference system, as a function of the DOFs of Table 4.2. For clarity, these equations are not reported here and showed in Appendix B.

Track adds a kinematic constraint equation to the problem. Infinitely high stiffness and a negligible thickness characterise the track in this model. Under these assumptions, a change in the orientation of only one of the rigid bodies would change the length of the track. This constraint can be expressed as follows:

$$L_{track} = L_{nom} \tag{4.9}$$

where L_{nom} is one design variable. Since the total length of the robot is approximately 1200 mm, L_{nom} imposed is 2845 mm. The derivation of L_{track} in terms of DOFs is explained in Appendix C.

Equations shown represent a system of eight equations with nine unknows corresponding to the system DOFs. Then, there are many different solutions to the problem and we need to think about how things balance to find the right one. We will learn more about this in the next part.

4.2.3 Equilibrium equations

If a vehicle has more than two wheels, it becomes harder to figure out how much weight is on each wheel using normal equations. So, we need to look at how the elastic parts of the wheels bend to figure out how much weight they are carrying. To do this, we also need to think about how the bodies 2 to 7 of the vehicle balance and rotate respect D, F, V and E. These equations introduce eighteen additional unknown parameters, that are reported in Table 4.3.

The numbering of the track branches tensions is omitted for shortness. The weight of the single suspension bodies, wheels and track is neglected. Half vehicle mass is set to 110 kg and the weight force applied to vehicle center of gravity (COG) is indicated as W. The COG position (X_G, Z_G) has been defined in the centreline of the vehicle. The equilibrium equations are obtained and reported in Appendix D. Track tensions directions relative to the horizontal direction (ϵ_{ij} and ϵ_{ij}) and the tangency point positions ($XQij$ and $ZQij$) are derived in Appendix C. Referring to Table 4.2 in Appendix E, it is possible to express the rotation of the elastic forces ($\beta_1, \beta_2, \beta_3$ and β_4) in terms of the system DOFs.

Elastic elements deflection are used to compute forces $F_{el,1}$, $F_{el,2}$, $F_{el,3}$, $F_{el,4}$. Each spring in the suspension has a set amount of pressure called pre-load. If a force smaller than the pre-load is applied to the spring, it will act like a stiff object and not bend or move. This applies to all four parts of the suspension that help the car move smoothly:

$$L_i = \begin{cases} L_{max,i} & \text{if } F_{el,i} < F_{pre,i} \\ L_{max,i} - (F_{el,i} - F_{pre,i})/k_i & \text{otherwise} \end{cases} \tag{4.10}$$

Table 4.3: List of unknowns.

Unknowns	Description
T_1	Track tension of branch 1
T_2	Track tension of branch 2
T_3	Track tension of branch 3
T_4	Track tension of branch 4
T_5	Track tension of branch 5
T_6	Track tension of branch 6
T_7	Track tension of branch 7
T_8	Track tension of branch 8
C	Torque applied to W1 (A point)
N_3	Vertical force for wheel 3
N_4	Vertical force for wheel 4
N_5	Vertical force for wheel 5
N_6	Vertical force for wheel 6
N_7	Vertical force for wheel 7
N_8	Vertical force for wheel 8
$F_{el,1}$	Applied force to spring 1
$F_{el,2}$	Applied force to spring 2
$F_{el,3}$	Applied force to spring 3
$F_{el,4}$	Applied force to spring 4

where L_i is the length of spring i when a force $F_{el,i}$ is applied to its ends, $F_{pre,i}$ and $L_{max,i}$ are the pre-load and the maximum length of spring i respectively, k is the elastic stiffness.

DOFs in Appendix E are used to compute the deformable elements lengths (L_i for i = 1,2,3,4). Wheels equilibrium equations are considered to close the system. W_1 is the only wheel with drive torque. This results in a further eight equations as follows. This simplifies the problem because, due to the tangential forces between the track and the support surface, the horizontal component of tension may vary along the track.

$$T_1 = T_2 \tag{4.11}$$

$$T_2 = T_3 \tag{4.12}$$

$$T_3 = T_4 \tag{4.13}$$

$$T_4 = T_5 \tag{4.14}$$

$$T_5 = T_6 \tag{4.15}$$

$$T_6 = T_7 \tag{4.16}$$

$$T_7 = T_8 \tag{4.17}$$

$$T_8 = T_1 + C/r_1 \tag{4.18}$$

Equations shown represent a system of twenty-eight equations in twenty-eight unknowns which are the nine DOFs of Table 4.2 plus the nineteen unknown forces of Table 4.3.

4.3 Matlab Simulation model

The analytical model just presented is implemented in Matlab® software to evaluate the way the robot is positioned, the configuration of its suspension system, the external forces and forces acting on bodies when "XXbot" overcoming a series of stair steps starting from the flat surface. Step dimensions are high 140 mm and depth 250 mm.

Since we are considering a quasi-static kinematic problem, the analytical model evaluates the static equilibrium of the robot in precise configurations. Since it is impossible to evaluate all the configurations that the robot assumes when climbing the flight of stairs, only the most significant ones are chosen. For clarity Fig. 4.3 shows the configuration where wheels W_3 and W_4 are on the second step. When an edge of the step is located between two wheels and deforms the shape of the track, it is necessary to evaluate the constraining reaction N_{Ci} that the corner applies to the robot. For simplicity, it is considered vertical and applied at the step edge. This leads to the introduction of two further unknowns to the problem, the vertical reaction N_{Ci} and the track tension T_{Ci} downstream of the corner. T_{prev} is the track tension in the upstream branch of the corner. To close the system, two further equations that evaluate the equilibrium of a little portion of the track

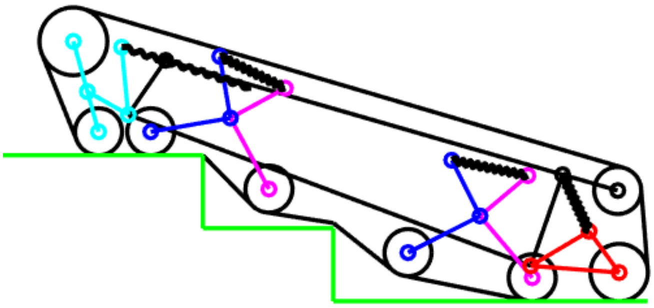

Figure 4.3: "XXbot" on the second stair step.

around the obstacle are used:

$$T_{prev}\sin\left(\epsilon_{Ci-W_{prev}}\right)+T_{Ci}\sin\left(\epsilon_{Ci-W_{succ}}\right)=N_{Ci} \tag{4.19}$$
$$T_{prev}\cos\left(\epsilon_{Ci-W_{prev}}\right)+T_{Ci}\cos\left(\epsilon_{Ci-W_{succ}}\right)=0 \tag{4.20}$$

Furthermore, the vertical constraining reaction N_{Ci} is taken into account in the equilibrium equations of vertical translation and rotation around the point P as follows:

$$W=N_3+N_4+N_5+N_6+N_7+N_8+N_{Ci} \tag{4.21}$$

$$\begin{split}N_4(X_K-X_P)+N_5(X_I-X_P)+N_6(X_Q-X_P)+N_7(X_R-X_P)\\+N_8(X_M-X_P)+N_{Ci}(X_{NCi}-X_P)=W(X_G-X_P)\end{split} \tag{4.22}$$

This procedure is repeated as many times as how much step edges deform the shape of the track in a configuration.

4.4 MSC Adams ATV Simulations

MSC.ADAMS software performs dynamical simulation of mechanical systems. It is like a box that has important parts and extra parts that can be added. The ADAMS/View package helps us to understand how mechanical systems work. There are other packages that focus on different parts of machines. Tracked vehicles can be modeled using the ADAMS Tracked Vehicle (ATV) Toolkit.

It allows creating, modifying and simulating realistic spatial models of tracked vehicles in the ADAMS environment. Using this software, a dynamic simulation of a stair-climbing case is carried out. For simplicity, half symmetry model is assumed for the vehicle. Also in this case, the $X_g - Z_g$ plane, defined in 4.2.1, contains the vehicle center of mass. The model not include roll and yaw rotations (φ and ψ) but only pitch movements (θ). Robot specific details and step dimensions are taken from the Matlab analytical model described above. The angular velocity of the sprocket is 15 deg/s. Half vehicle mass is set to 110 kg.

Table 4.4: List of unknowns.

Name	Description	Value
μ_S	static friction coefficient	0.9
μ_D	dynamic friction coefficient	0.7
V_S	stiction transition velocity	0.001 m/s
V_D	friction transition velocity	0.05 m/s

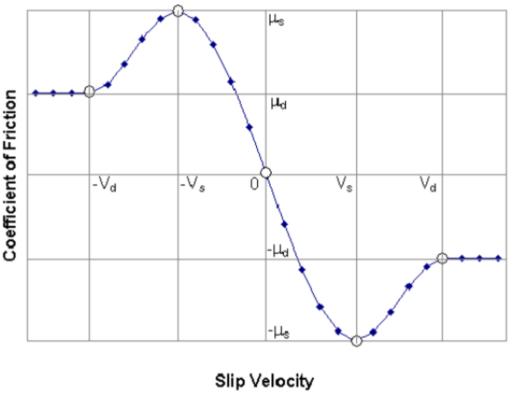

Figure 4.4: Coefficient of friction varying with slip velocity.

ADAMS uses a relatively simple velocity-based friction model for contacts. The Fig. 4.4 shows the dependence between the coefficient of friction and the slip velocity. V_s, the stiction transition velocity, is the velocity at which the coefficient of friction achieves a maximum value of μ_S. μ_S is the coefficient of static friction between the track and the ground. The coefficient of dynamic frictions between the track and the ground is μ_D. ADAMS changes μ_S to μ_D as the slip velocity at the contact point increases. When the slip velocity reach the value of V_D, the effective coefficient of friction is equal to the dynamic coefficient μ_D. Table 4.4 summarises contact parameters values.

The case of stair climbing simulations are described in following. First, the tracked robot model and the stair-shaped ground were created in the pre-processing environment of the Adams ATV software. Then the simulation parameters were defined and the calculation was launched in the solution environment. The program initially solves the static problem in the initial condition. It then solves the dynamic problem for each time instant until it reaches the end of the simulation. Simulation results are reported in the software post-processing environment.

Fig. 4.5 shows the simulation initial condition in a perspective view. Figure 4.6 shows a sequence of simulation snapshots in the moments of time that seemed most significant to us. Following tables summarises the forces in the spring elements, the vertical contact forces between track and step as well as the tension in the belt downstream and upstream of the sprocket for the same instants of simulation time.

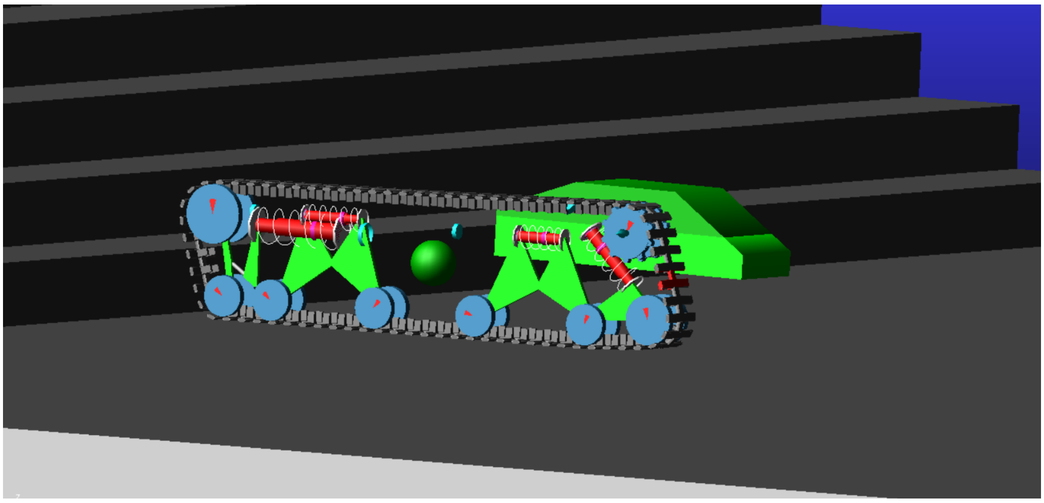

Figure 4.5: Tracked vehicle model in ATV Toolkit.

Table 4.5 refers to Fig. 4.6(a) (flat ground). Table 4.6 refers to Fig. 4.6(b) (first step). Table 4.7 refers to Fig. 4.6(c) (second step). Table 4.8 refers to Fig.4.6(d) (third step).

Finally, Fig.4.7 shows the motor torque during stair-climbing simulation. Vertical lines named flat ground, first step, second step and third step refer to the simulation instants shown in Fig. 4.6. It can be seen that maximum torque occurs when the front of the robot meets the step and overcomes it.

MSC.ADAMS simulation proof that the proposed tracked robot can effectively climb a flight of stairs without tipping over backwards.

4.5 Conclusion and future works

This chapter talks about a new tracked-based robot called "XXbot". It uses a innovative system of articulated suspension. Each wheel on the road can move up and down to adapt the track shape to the stairs structure. The developed design aims to perform better compared to other stairs-climbing robots. We also developed a special model that helps us to figure out how the robot will move according to the shape of the ground. The model uses a static approach of forces and consists of 28 equations in 28 unknowns that are the nine suspensions DOFs and the nineteen unknown forces, including internal and contact forces. This means that we are trying to figure out how the rover is positioned on the ground and how its wheels are set up, while also considering that the track on the wheels cannot change its length. It is a useful tool to predict the behavior of the system in climbing stair conditions. The novelty of the present work compared to [87] is that the model has been modified to be used as a tool to design new complex systems and optimize the performance of the new robots. To verify that the proposed tracked robot can effectively climb a flight of stairs without tipping over backwards, MSC.ADAMS dynamic simulation is carried out. The angular velocity

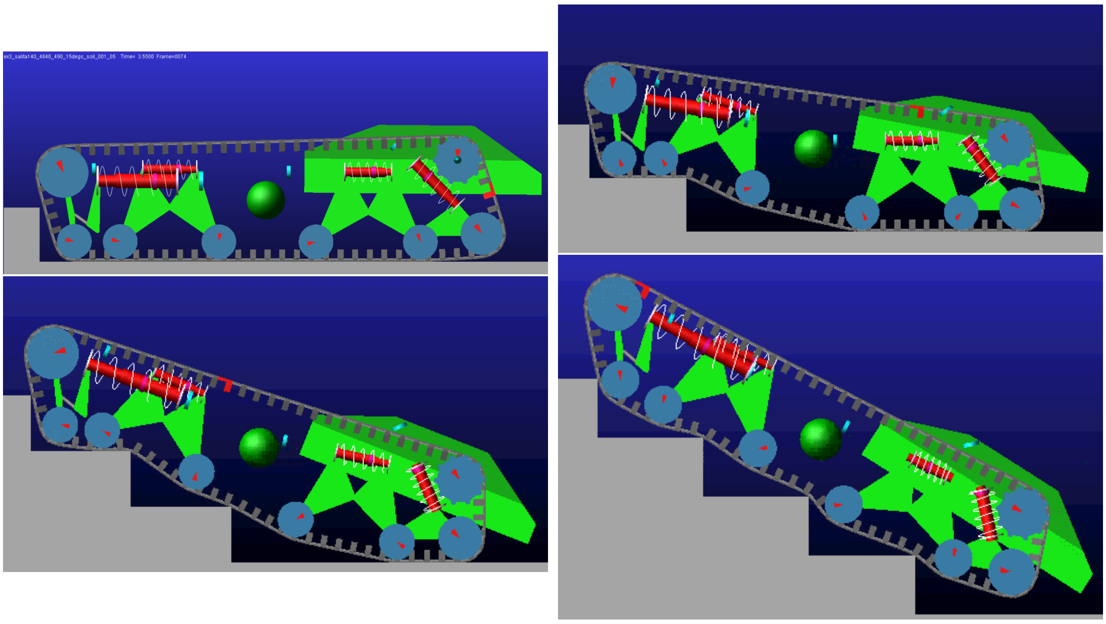

Figure 4.6: ADAMS ATV stair-climbing simulation snapshots: (**a**) Top-left:flat ground; (**b**) Top-right:first step; (**c**)Down-left:second step; (**d**)Down-right:third step

Table 4.5: Forces in the spring elements, the vertical contact forces between track and step,belt tension for flat ground configuration.

Name	Description	Value (N)
$F_{el,1}$	Applied force to spring 1	265
$F_{el,2}$	Applied force to spring 2	778
$F_{el,3}$	Applied force to spring 3	691
$F_{el,4}$	Applied force to spring 4	401
N_3	Vertical force for wheel 3	84
N_4	Vertical force for wheel 4	240
N_5	Vertical force for wheel 5	190
N_6	Vertical force for wheel 6	297
N_7	Vertical force for wheel 7	279
N_8	Vertical force for wheel 8	0
T_{up}	Belt tension upstream of the sprocket	613
T_{down}	Belt tension downstream of the sprocket	641

Table 4.6: Forces in the spring elements, the vertical contact forces between track and step,belt tension for first step configuration.

Name	Description	Value (N)
$F_{el,1}$	Applied force to spring 1	219
$F_{el,2}$	Applied force to spring 2	1105
$F_{el,3}$	Applied force to spring 3	607
$F_{el,4}$	Applied force to spring 4	268
N_3	Vertical force for wheel 3	138
N_4	Vertical force for wheel 4	112
N_5	Vertical force for wheel 5	0
N_6	Vertical force for wheel 6	88
N_7	Vertical force for wheel 7	198
N_8	Vertical force for wheel 8	221
N_{C1}	Vertical contact forces between track and step 1	332
T_{up}	Belt tension upstream of the sprocket	500
T_{down}	Belt tension downstream of the sprocket	653

Table 4.7: Forces in the spring elements, the vertical contact forces between track and step,belt tension for second step configuration.

Name	Description	Value (N)
$F_{el,1}$	Applied force to spring 1	284
$F_{el,2}$	Applied force to spring 2	1418
$F_{el,3}$	Applied force to spring 3	469
$F_{el,4}$	Applied force to spring 4	296
N_3	Vertical force for wheel 3	0
N_4	Vertical force for wheel 4	56
N_5	Vertical force for wheel 5	0
N_6	Vertical force for wheel 6	0
N_7	Vertical force for wheel 7	95
N_8	Vertical force for wheel 8	310
N_{C1}	Vertical contact forces between track and step 1	88
N_{C2}	Vertical contact forces between track and step 2	570
T_{up}	Belt tension upstream of the sprocket	558
T_{down}	Belt tension downstream of the sprocket	779

Table 4.8: Forces in the spring elements, the vertical contact forces between track and step,belt tension for third step configuration.

Name	Description	Value (N)
$F_{el,1}$	Applied force to spring 1	199
$F_{el,2}$	Applied force to spring 2	1467
$F_{el,3}$	Applied force to spring 3	347
$F_{el,4}$	Applied force to spring 4	560
N_3	Vertical force for wheel 3	0
N_4	Vertical force for wheel 4	0
N_5	Vertical force for wheel 5	0
N_6	Vertical force for wheel 6	0
N_7	Vertical force for wheel 7	0
N_8	Vertical force for wheel 8	0
N_{C1}	Vertical contact forces between track and step 1	383
N_{C2}	Vertical contact forces between track and step 2	450
N_{C3}	Vertical contact forces between track and step 3	283
T_{up}	Belt tension upstream of the sprocket	448
T_{down}	Belt tension downstream of the sprocket	1120

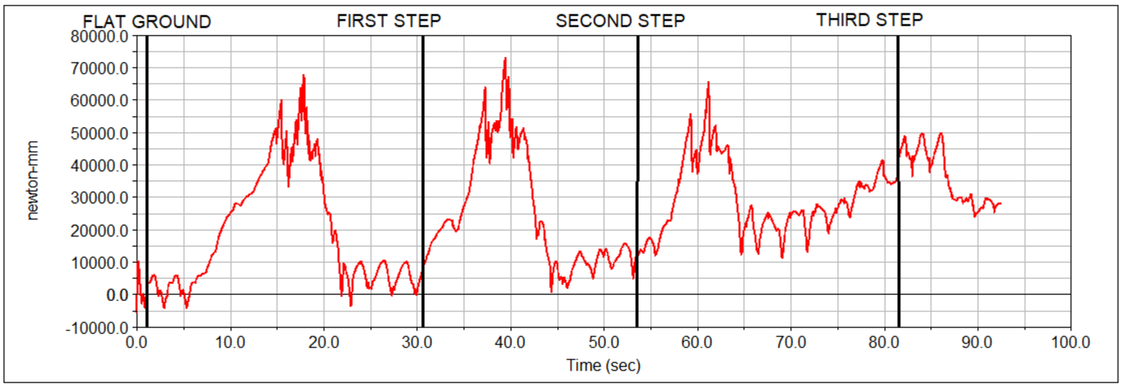

Figure 4.7: Motor Torque in the stair-climbing process.

of the sprocket is 15 deg/s. Half vehicle mass is set to 110 kg. Figure 4.6 and Table 4.5 to Table 4.8 summarises the simulation results and proof the effectiveness of the proposed vehicle.

Given the vehicle's excellent ability to overcome a flight of stairs, it could be used in hazardous work environments and in repetitive tasks. Specifically it can be used for surveillance and monitoring, military, health care, industrial and agricultural applications. In particular, inspection and monitoring of buildings and infrastructure, including commercial and residential buildings.

Nonetheless, the proposed platform could be used as a starting point to build an electric powered wheelchair (EPW) and help people with disabilities overcome architectural barriers.

Conclusions and Future Developments

This thesis focuses on the analysis and development of innovative technologies to improve robots' ability to overcome different types of obstacles. The primary goal is to enhance the robots' capability to operate in challenging environments and ensure smooth and safe movement even in the presence of physical barriers, thus contributing to the advancement of mobile robotics.

Moreover, this thesis address the stair-climbing problem in order to foster the understanding on contact mechanics between flat belt and corner edge and design a tracked stair-climbing robot using innovative suspension system to overcome architectural barriers.

As main focus of our study, a systematic review on stair-climbing robot has been presented, including brief descriptions of the mechanism and method of operation and highlighting the advantages and disadvantages of different types of climbing platform (Chapter 1). To quantitatively evaluate the system performance, various metrics are presented that consider allowable payload, maximum climbing speed, maximum crossable slope, transport ability and their combinations. Using these metrics, it is possible to compare vehicles with different locomotion modes and properties, allowing researchers and practitioners to gain in-depth knowledge of stair-climbing vehicles and choose the best category for transporting people and heavy loads up a flight of stairs. As a result, track-based and wheel cluster-based robots prove to be the most suitable categories to perform the transport of a load during the ascent of a flight of stairs.

The Chapter 2 aims to propose a rigorous analysis approach to study what happens when different kind of rubber belts or tires are in contact with a corner edge and what forces are exchanged between these two elements. A general introduction is given by mainly focusing on the scientific literature lack of a comprehensive wheel-obstacle contact model for the step-climbing problem. Then the importance of considering tire deformation has been emphasised and a novel approach to wheel-obstacle contact mechanics is given. A description of the test bench specifically developed for this work is provided along the experimental results for two cases of flat belt and tire patch that can be summarised as follows: 1) the forces exchanged between a rubber belt and a corner edge depend on the relative angle θ between the two branches of the belt and on the friction coefficient; 2) The forces exchanged between a tyre tread and a corner edge depend on the relative angle θ of the two tyre segments when it is pushed against the corner edge and the friction coefficient. The experimental tests showed how a pneumatic tyre patch behaves similarly to a belt when it is in contact with a step corner edge.

Following, the experimental results have been compared with Euler theoretical model to describe the behaviour of both tension $\frac{T_1}{T_2}$ while the relative angle θ changes its value. Figure 2.8 and Figure 2.9 allows to determine that the Euler model can be considered suitable for predicting what happens along the two branches of the belt when it is in contact with a corner edge. Moreover, it has been demonstrated that deflating a tire or facilitating its deflection can improve the capacity of a vehicle to climb up a step by increasing the contact forces exchanged with the ground.

Chapter 3 presents experimental results on the behavior of a conventional pneumatic tire clearing a step-obstacle, alongside an analytical model developed to analyze the interaction between a deformable tire and the corner edge of a step-obstacle. Two-dimensional models for both non-pneumatic and pneumatic tires are formulated. The non-pneumatic tire model consists of a thin, flexible annular band, supported by springs that connect the band to a rigid hub. The pneumatic tire model extends this by incorporating the effects of tangential springs and internal pressure. Timoshenko's curved beam theory is employed to model the annular band, accounting for deformations due to bending, shearing, and circumferential extension. Governing differential equations are derived for both non-pneumatic and pneumatic tire cases. The results of the in-plane deformation model for different vertical forces are discussed, as well as the characteristics of tread tension. This approach follows the standard methodology for analyzing strain-based intelligent tires under flat ground loading conditions. Additionally, model results for the interaction between the tire and a step-obstacle are presented, with a particular focus on tire tread deformation. The model's predictions are compared with experimental data, demonstrating a good agreement between the two. The analysis for pneumatic tires also highlights the effect of pressure on the ability to overcome a step-obstacle, showing that tires with lower pressure can clear greater obstacle heights.

In Chapter 4, the "XXbot" concept is presented. It is a tracked vehicle and uses a innovative system of articulated suspension. Each wheel on the road can move up and down to adapt the track shape to the stairs structure. We also developed a special model that helps us to figure out how the robot will move according to the shape of the ground. The model uses a static approach of forces and consists of 28 equations in 28 unknowns that are the nine suspensions DOFs and the nineteen unknown forces, including internal and contact forces. This means that we are trying to figure out how the vehicle is positioned on the ground and how its wheels are set up, while also considering that the track on the wheels cannot change its length. It is a useful tool to predict the behavior of the system in climbing stair conditions. To verify that the proposed tracked robot can effectively climb a flight of stairs without tipping over backwards, MSC.ADAMS dynamic simulation is carried out proving the vehicle's excellent ability to overcome a flight of stairs. The proposed platform can be used as a starting point to build an electric powered wheelchair (EPW) and help people with disabilities overcome architectural barriers.

As future development, we will explore the innovative design and potential advantages of incorporating deformable wheels into tracked vehicle systems. Building upon the results and analyses presented in previous chapters, we will introduce a new tracked vehicle concept that seeks to overcome the challenges associated with conventional wheel designs. By focusing on pneumatic and non-pneumatic deformable wheels, this design aims to achieve improved obstacle negotiation, shock absorption, and overall efficiency, particularly in environments where traditional rigid wheels struggle. Deformable wheels for tracked vehicles present a substantial step forward in addressing the limitations of traditional tracked vehicles, securing their role in the evolving field of mobile robotics.

Appendix A

In this appendix, performance metrics introduces in Section 1.3.1 are calculated for the robots analyzed in this document. WT and CT indicate wheelchair type and carrier type robots, respectively. When technical data are not provided, metrics are omitted. Tables A.1 and A.2 show the Payload Capacity and Normalized speed, respectively. Normalized Work Capability is calculated in Table A.3. Maximum crossable step height and stairs slope are reported in Table A.4. Then, Transport Ability values are calculated in Table A.5.

Name	**Type**	**Category**	**PC (%)**
Scewo Bro	WT	Track	74.07
WT Wheelchair	WT	Track	57.69
TopChair-S	WT	Track	73.33
Tao	WT	Track	150
B-Free Ranger	WT	Track	82.19
Caterwil GTS5 Lux	WT	Track	87.71
All-Terrain Wheelchair	WT	Track	50
iBOT 4000	WT	Wheel cluster	123.63
Wheelchair.q	WT	Wheel cluster	88.77
Zero Carrier	WT	Hybrid and Leg	173.91
Lee	WT	Hybrid and Leg	85.71
WL-16 II	WT	Hybrid and Leg	96.77
RT-Mover PType WA	WT	Articulated Mechanism	76.08
Morales	WT	Articulated Mechanism	90
Lawn	WT	Articulated Mechanism	50
TBW-I	WT	Articulated Mechanism	38.96
HELIOS-V	WT	Articulated Mechanism	100
Chen	WT	Articulated Mechanism	100
Yoneda	CT	Track	92.30
TAQT Carrier	CT	Track	25.80
HELIOS-VI	CT	Track	141.17
Haulerbot	CT	Track	89.04
iRobt 710 Kobra	CT	Track	40.96
Deshmukh	CT	Wheel cluster	125

Table A.1: Payload capacity of the analyzed robots.

Name	**Type**	**Category**	**NS ($\mathbf{s^{-1}}$)**
Scewo Bro	WT	Track	0.18
WT Wheelchair	WT	Track	0.07
TopChair-S	WT	Track	0.16
Tao	WT	Track	0.08
B-Free Ranger	WT	Track	0.074
Caterwil GTS5 Lux	WT	Track	0.21
All-Terrain Wheelchair	WT	Track	0.19
iBOT 4000	WT	Wheel cluster	0.12
Wheelchair.q	WT	Wheel cluster	0.14
Zero Carrier	WT	Hybrid and Leg	0.01
Lee	WT	Hybrid and Leg	0.02
WL-16 II	WT	Hybrid and Leg	0.07
RT-Mover PType WA	WT	Articulated Mechanism	0.02
Morales	WT	Articulated Mechanism	0.007
Lawn	WT	Articulated Mechanism	0.006
TBW-I	WT	Articulated Mechanism	0.005
Chen	WT	Articulated Mechanism	0.02
Yoneda	CT	Track	0.09
TAQT Carrier	CT	Track	0.10
HELIOS-VI	CT	Track	0.06
Haulerbot	CT	Track	0.072
iRobt 710 Kobra	CT	Track	0.15
Deshmukh	CT	Wheel cluster	0.08

Table A.2: Normalized speed of the analyzed robots.

Name	**Type**	**Category**	**NWC (s^{-1})**
Scewo Bro	WT	Track	13.33
WT Wheelchair	WT	Track	4.40
TopChair-S	WT	Track	11.73
Tao	WT	Track	12.14
B-Free Ranger	WT	Track	6.08
Caterwil GTS5 Lux	WT	Track	18.85
All-Terrain Wheelchair	WT	Track	9.61
iBOT 4000	WT	Wheel cluster	14.83
Wheelchair.q	WT	Wheel cluster	12.43
Zero Carrier	WT	Hybrid and Leg	1.74
Lee	WT	Hybrid and Leg	1.71
WL-16 II	WT	Hybrid and Leg	6.77
RT-Mover PType WA	WT	Articulated Mechanism	1.52
Morales	WT	Articulated Mechanism	0.62
Lawn	WT	Articulated Mechanism	0.30
TBW-I	WT	Articulated Mechanism	0.195
Chen	WT	Articulated Mechanism	2.00
Yoneda	CT	Track	8.30
TAQT Carrier	CT	Track	2.58
HELIOS-VI	CT	Track	8.47
Haulerbot	CT	Track	6.41
iRobt 710 Kobra	CT	Track	6.27
Deshmukh	CT	Wheel cluster	10.06

Table A.3: Normalized work capability of the analyzed robots.

Name	**Type**	**Category**	**Height (cm)**	**Slope (°)**
Scewo Bro	WT	Track	20	36
WT Wheelchair	WT	Track	15	25
TopChair-S	WT	Track	20	35
Tao	WT	Track	18	35
B-Free Ranger	WT	Track	20	35
Caterwil GTS5 Lux	WT	Track	20	40
All-Terrain Wheelchair	WT	Track	17	31
iBOT 4000	WT	Wheel cluster	20	39
Wheelchair.q	WT	Wheel cluster	24	40
Castillo	WT	Wheel cluster	18	37
Zero Carrier	WT	Hybrid and Leg	18	27
Lee	WT	Hybrid and Leg	25.5	45
WL-16 II	WT	Hybrid and Leg	15	27
RT-Mover PType WA	WT	Articulated Mechanism	17	35
Morales	WT	Articulated Mechanism	24	40
Lawn	WT	Articulated Mechanism	20	35
TBW-I	WT	Articulated Mechanism	20	20
HELIOS-V	WT	Articulated Mechanism	16	28
Chen	WT	Articulated Mechanism	20	37.5
Yoneda	CT	Track	16	30
Haulerbot	CT	Track	20	38
iRobt 710 Kobra	CT	Track	21.2	45
Deshmukh	CT	Wheel cluster	16	40
Wen	CT	Hybrid and Leg	20	35.5

Table A.4: Crossable step height and stairs slope of the analyzed robots.

Name	**Type**	**Category**	**TA (kg/W)**	**Power (W)**
TopChair-S	WT	Track	0.137	800
Tao	WT	Track	0.075	1000
B-Free Ranger	WT	Track	0.08	1500
All-Terrain Wheelchair	WT	Track	0.087	920
iBOT 4000	WT	Wheel cluster	0.075	1800
Wheelchair.q	WT	Wheel cluster	0.174	500
Castillo	WT	Wheel cluster	0.041	1430
Zero Carrier	WT	Hybrid and Leg	0.074	1080
Lee	WT	Hybrid and Leg	0.06	1200
WL-16 II	WT	Hybrid and Leg	0.033	1800
RT-Mover PType WA	WT	Articulated Mechanism	0.041	1700
Morales	WT	Articulated Mechanism	0.119	840
TBW-I	WT	Articulated Mechanism	0.066	900
HELIOS-V	WT	Articulated Mechanism	0.062	800
Chen	WT	Articulated Mechanism	0.025	3200
TAQT Carrier	CT	Track	0.044	1800
HELIOS-VI	CT	Track	0.193	622
Haulerbot	CT	Track	0.086	1500
Deshmukh	CT	Wheel cluster	0.069	144

Table A.5: Transport ability values of the analyzed robots.

Name	**Type**	**Category**	**MC/CC**
Scewo Bro	WT	Track	Medium-low/Medium-low
WT Wheelchair	WT	Track	Medium-high/Medium-high
TopChair-S	WT	Track	Medium-low/Medium-low
Tao	WT	Track	Medium-low/Medium-low
B-Free Ranger	WT	Track	Medium-high/Medium-high
iBOT 4000	WT	Wheel cluster	Medium-low/Medium-high
Wheelchair.q	WT	Wheel cluster	Medium-low/Medium-high
Zero Carrier	WT	Hybrid and Leg	Medium-high/High
Lee	WT	Hybrid and Leg	High/High
WL-16 II	WT	Hybrid and Leg	Very-high/Very-high
RT-Mover PType WA	WT	Articulated Mechanism	High/High
Morales	WT	Articulated Mechanism	High/High
TBW-I	WT	Articulated Mechanism	High/High
Chen	WT	Articulated Mechanism	High/High
HELIOS-V	WT	Articulated Mechanism	Medium-high/Medium-high

Table A.6: Mechanical and control complexity values of the analyzed robots.

Name	**Type**	**Category**	**Cost**
Scewo Bro	WT	Track	Medium
WT Wheelchair	WT	Track	Medium
TopChair-S	WT	Track	Medium-low
Tao	WT	Track	Medium-low
B-Free Ranger	WT	Track	Medium
ZED Evolution	WT	Track	Medium
Caterwil GTS5 Lux	WT	Track	Medium-low
Fortissimo	WT	Track	Medium
Hkust	WT	Track	Medium-low
All-Terrain Wheelchair	WT	Track	Medium
iBOT 4000	WT	Wheel cluster	Medium-low
Wheelchair.q	WT	Wheel cluster	Medium-low
Castillo	WT	Wheel cluster	Medium-low
Wang	WT	Hybrid and Leg	Medium
Zero Carrier	WT	Hybrid and Leg	High
Lee	WT	Hybrid and Leg	Medium-high
JWCR-1	WT	Hybrid and Leg	High
WL-16 II	WT	Hybrid and Leg	High
RT-Mover PType WA	WT	Articulated Mechanism	Medium-high
Morales	WT	Articulated Mechanism	Medium-high
Lawn	WT	Articulated Mechanism	Medium-high
TBW-I	WT	Articulated Mechanism	Medium-high
HELIOS-V	WT	Articulated Mechanism	Medium
Chen	WT	Articulated Mechanism	Medium-high
RPWheel	WT	Articulated Mechanism	Medium
Zhang	CT	Track	Medium
Dongsheng	CT	Track	Medium
Htoo	CT	Track	Medium-low
Amoeba Go-1	CT	Track	Medium
Yoneda	CT	Track	Medium-low
Riuqin	CT	Track	Medium-low
TAQT Carrier	CT	Track	Medium
HELIOS-VI	CT	Track	Medium-low
Haulerbot	CT	Track	Medium
iRobt 710 Kobra	CT	Track	Medium
Deshmukh	CT	Wheel cluster	Low
Wen	CT	Hybrid and Leg	Medium-high
Shihua	CT	Hybrid and Leg	Medium-low
PEOPLER-II	CT	Hybrid and Leg	High
Yeping	CT	Hybrid and Leg	High
Yinhui	CT	Articulated Mechanism	Medium

Table A.7: Mechanical complexity, control complexity, and cost of the analyzed robots.

Appendix B

Based on the way the suspension is built (Fig. B.1), we can figure out where the wheels are located using a system called the vehicle reference frame. We can find the wheel centers (which are called P, K, I, Q, R, and M) X and Z coordinates by using the information from Table 4.2:

$$\begin{aligned} X_P = X_A + (d_3 + d_{18} + d_{19} + d_{20} + d_4)\sin\theta_1 - \\ (d_{14} + d_{15} + d_{16} + d_{17} + d_1 + d_2)\cos\theta_1 - \\ d_{11}\sin(\theta_5 + \alpha_3) + d_13\cos(\alpha_4 + \pi/2 - \theta_5 - \alpha_3) \end{aligned} \tag{B.1}$$

$$\begin{aligned} Z_P = Z_A - (d_3 + d_{18} + d_{19} + d_{20} + d_4)\cos\theta_1 - \\ (d_{14} + d_{15} + d_{16} + d_{17} + d_1 + d_2)\sin\theta_1 - \\ d_{11}\cos(\theta_5 + \alpha_3) + d_{13}\sin(\alpha_4 + \pi/2 - \theta_5 - \alpha_3) \end{aligned} \tag{B.2}$$

$$X_K = X_A + (d_3 + d_{18} + d_{19})\sin\theta_1 - (d_{14} + d_{15} + d_{16} + d_{17})\cos\theta_1 - d_6\sin(\theta_3 + \alpha_1) \tag{B.3}$$

$$Z_K = Z_A - (d_3 + d_{18} + d_{19})\cos\theta_1 - (d_{14} + d_{15} + d_{16} + d_{17})\sin\theta_1 - d_6\cos(\theta_3 + \alpha_1) \tag{B.4}$$

$$X_I = X_A + (d_3 + d_{18} + d_{19})\sin\theta_1 - (d_{14} + d_{15} + d_{16} + d_{17})\cos\theta_1 - d_6\sin\theta_2 \tag{B.5}$$

$$Z_I = Z_A - (d_3 + d_{18} + d_{19})\cos\theta_1 - (d_{14} + d_{15} + d_{16} + d_{17})\sin\theta_1 - d_6\cos\theta_2 \tag{B.6}$$

$$X_Q = X_A + (d_3 + d_{18} + d_{19})\sin\theta_1 - (d_{14} + d_{15} + d_{16})\cos\theta_1 - d_6\sin(\theta_6 + \alpha_1) \tag{B.7}$$

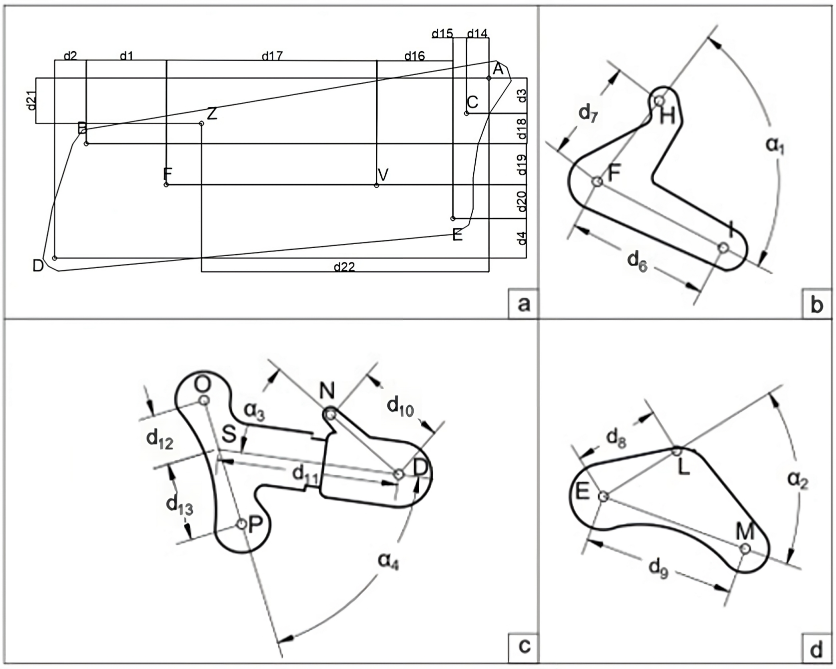

Figure B.1: Body and suspension dimensions

$$Z_Q = Z_A - (d_3 + d_{18} + d_{19}) \cos\theta_1 - (d_{14} + d_{15} + d_{16}) \sin\theta_1 - d_6 \cos(\theta_6 + \alpha_1) \tag{B.8}$$

$$X_R = X_A + (d_3 + d_{18} + d_{19}) \sin\theta_1 - (d_{14} + d_{15} + d_{16}) \cos\theta_1 + d_6 \sin(\theta_7) \tag{B.9}$$

$$Z_R = Z_A - (d_3 + d_{18} + d_{19}) \cos\theta_1 - (d_{14} + d_{15} + d_{16}) \sin\theta_1 + d_6 \cos(\theta_7) \tag{B.10}$$

$$X_M = X_A + (d_3 + d_{18} + d_{19} + d_{20}) \sin\theta_1 - (d_{14} + d_{15}) \cos\theta_1 + d_9 \sin(\theta_4) \tag{B.11}$$

$$Z_M = Z_A - (d_3 + d_{18} + d_{19} + d_{20}) \cos\theta_1 - (d_{14} + d_{15}) \sin\theta_1 + d_9 \cos(\theta_4) \tag{B.12}$$

Appendix C

In this section, we figure out how to find the length of the track based on the number of parts on a Table 4.2. The track goes around the wheels and can be made up of straight lines and curved lines. Each wheel's curved line can be described using the position of the wheels before and after it. For instance, we can calculate the length of the track between Q_{12} and Q_{18} (Fig. C.1) as follow:

$$Q_{12}\hat{}Q_{18} = R_1(2\pi + \delta_{fol} - \gamma_{fol} - \delta_{pre} - \gamma_{pre}) \tag{C.1}$$

where R_1 is the radius of wheel 1, the angle that $\overline{AO}$ line forms respect to the horizontally is called δ_{fol}, the angle that $\overline{AM}$ line forms respect to the horizontally is called δ_{pre}, the angle between the tangency point Q_{12} and $\overline{AO}$ is called γ_{fol}, the angle between the tangency point Q_{18} and $\overline{AM}$ is called γ_{pre}.

We calculate the angles as :

$$\delta_{fol} = atan2(Z_O - Z_A, X_O - X_A) \tag{C.2}$$

$$\delta_{pre} = atan2(Z_M - Z_A, X_M - X_A) \tag{C.3}$$

$$\gamma_{fol} = \arccos\left(\frac{R_1 - R_2}{\overline{AO}}\right) \tag{C.4}$$

$$\gamma_{pre} = \arccos\left(\frac{R_1 - R_8}{\overline{AM}}\right) \tag{C.5}$$

where the four-quadrant inverse tangent is atan2, R_2 and R_8 are the wheels dimensions, $\overline{AO}$ and $\overline{AM}$ are the segments lengths. To figure out how long the

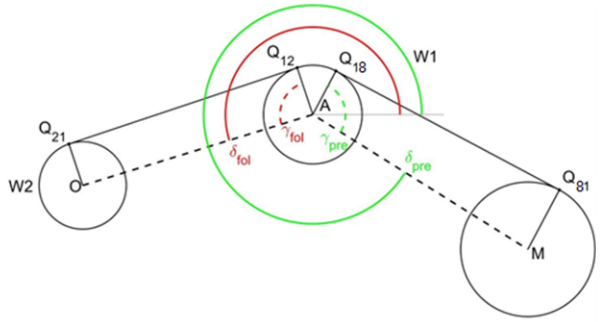

Figure C.1: Contact arc length between track and wheel 1 derivation track is, we need to look at a straight line between two points called Q_{12} and Q_{21}. We can calculate its length as:

$$\overline{Q_{12}Q_{21}} = \sqrt{\overline{AO}^2 + (R_1 - R_2)^2} \tag{C.6}$$

We can find the total length of the track by using some equations that help us understand how things work in general: C.1 and C.6.

$$L_{track} = \sum_{i=1}^{8} R_i \cdot (2\pi + \delta_{fol,i} - \gamma_{fol,i} - \delta_{pre,i} - \gamma_{pre,i}) + \sqrt{\overline{C_iC_{i+1}}^2 + (R_i - R_{i+1})^2} \tag{C.7}$$

where the wheel center is denoted as C_i and the wheel radius as R_i. For the formula of equation C.7 to work, δ_{pre} must be numerically grater than δ_{fol} for all wheels. Sometimes, not all wheels will have this condition. When this happens, it is sufficient to add 2π to δ_{pre}. For wheel 8, R_{i+1} is replaced by R_1. The suspension of a vehicle has certain shapes and measurements that can be described using numbers. The numbers can be figured out based on the different ways the suspension can move. There is a formula that calculates the length of the track, or the distance between the wheels, but it is very long and complicated and not easy to solve using math.

Appendix D

Referring to Fig. D.1, Fig. D.2 and Fig. D.3, the equilibrium equations are reported in the following

$$W = N_3 + N_4 + N_5 + N_6 + N_7 + N_8 \tag{D.1}$$

$$\begin{split} W(X_G - X_P) = N_4(X_K - X_P) + N_5(X_I - X_P) + N_6(X_Q - X_P) \\ + N_7(X_R - X_P) + N_8(X_M - X_P) \end{split} \tag{D.2}$$

$$\begin{split} F_{el,3} \cos\beta_3 \cdot (Z_N - Z_D) + F_{el,3} \sin\beta_3 \cdot (X_N - X_D) + \\ T_2 \cos\epsilon_{34}(Z_D - Z_{Q34}) - T_2 \sin\epsilon_{34}(X_D - X_{Q34}) - \\ T_1 \cos\epsilon_{21}(Z_{Q21} - Z_D) - T_1 \sin\epsilon_{21}(X_D - X_{Q21}) - N_3(X_D - X_P) = 0 \end{split} \tag{D.3}$$

$$\begin{split} F_{el,1} \cos\beta_1 \cdot (Z_J - Z_F) + F_{el,1} \sin\beta_1 \cdot (X_F - X_J) + \\ T_3 \cos\epsilon_{43}(Z_F - Z_{Q43}) - T_3 \sin\epsilon_{43}(X_F - X_{Q43}) + \\ T_4 \cos\epsilon_{45}(Z_F - Z_{Q45}) - T_4 \sin\epsilon_{45}(X_F - X_{Q45}) - N_4(X_F - X_K) = 0 \end{split} \tag{D.4}$$

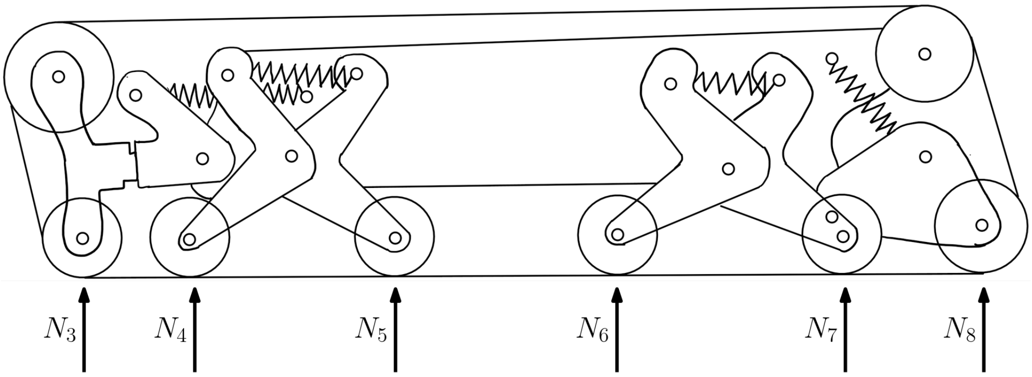

Figure D.1: Global free body diagram of the vehicle

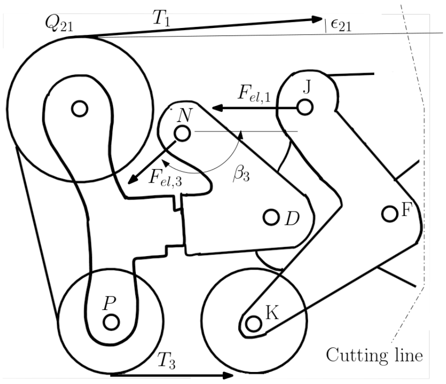

Figure D.2: Left half suspension system internal forces

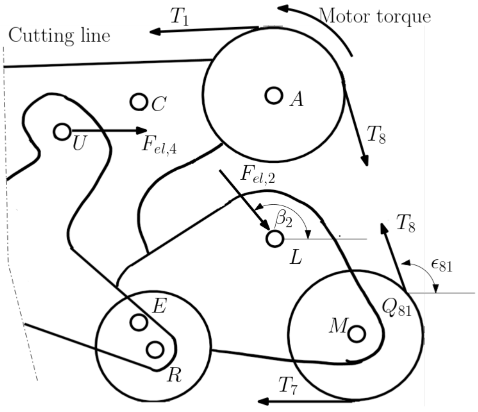

Figure D.3: Right half suspension system internal forces

$$\begin{gathered}-F_{el,1}\cos\beta_1\cdot(Z_H-Z_F)+F_{el,1}\sin\beta_1\cdot(X_H-X_F)+\\ T_4\cos\epsilon_{54}(Z_F-Z_{Q54})-T_4\sin\epsilon_{54}(X_{Q54}-X_F)+\\ T_5\cos\epsilon_{56}(Z_F-Z_{Q56})-T_5\sin\epsilon_{56}(X_{Q56}-X_F)+N_5(X_I-X_F)=0 \quad \text{(D.5)}\end{gathered}$$

$$\begin{gathered}F_{el,4}\cos\beta_4\cdot(Z_T-Z_V)+F_{el,4}\sin\beta_4\cdot(X_V-X_T)+\\ T_5\cos\epsilon_{65}(Z_V-Z_{Q65})-T_5\sin\epsilon_{65}(X_V-X_{Q65})+\\ T_6\cos\epsilon_{67}(Z_V-Z_{Q67})-T_6\sin\epsilon_{67}(X_{Q56}-X_F)-N_6(X_V-X_Q)=0 \quad \text{(D.6)}\end{gathered}$$

$$\begin{gathered}-F_{el,4}\cos\beta_4\cdot(Z_U-Z_V)+F_{el,4}\sin\beta_4\cdot(X_U-X_V)+\\ T_6\cos\epsilon_{76}(Z_V-Z_{Q76})-T_6\sin\epsilon_{76}(X_{Q76}-X_V)+\\ T_7\cos\epsilon_{78}(Z_V-Z_{Q78})-T_7\sin\epsilon_{78}(X_{Q78}-X_V)+N_7(X_R-X_V)=0 \quad \text{(D.7)}\end{gathered}$$

$$\begin{gathered}F_{el,2}\cos\beta_2\cdot(Z_E-Z_L)+F_{el,2}\sin\beta_2\cdot(X_L-X_E)+\\ T_8\cos\epsilon_{81}(Z_E-Z_{Q81})-T_8\sin\epsilon_{81}(X_{Q81}-X_E)+\\ T_7\cos\epsilon_{87}(Z_E-Z_{Q87})-T_7\sin\epsilon_{87}(X_{Q87}-X_E)+N_8(X_M-X_E)=0 \quad \text{(D.8)}\end{gathered}$$

Appendix E

We use the DOFs reported in Table 4.2 to calculate the springs length (S1, S2, S3 and S4):

$$L_1 = \sqrt{(X_H - X_J)^2 + (Z_H - Z_J)^2} \tag{E.1}$$

$$L_4 = \sqrt{(X_U - X_T)^2 + (Z_U - Z_T)^2} \tag{E.2}$$

$$L_2 = \sqrt{(X_C - X_L)^2 + (Z_C - Z_L)^2} \tag{E.3}$$

$$L_3 = \sqrt{(X_Z - X_N)^2 + (Z_Z - Z_N)^2} \tag{E.4}$$

where

$$(X_H - X_J) = d_7 \sin(\theta_2 + \alpha_1) + d_7 \sin\theta_3 \tag{E.5}$$

$$(Z_H - Z_J) = -d_7 \cos(\theta_2 + \alpha_1) - d_7 \cos\theta_3 \tag{E.6}$$

$$(X_U - X_T) = d_7 \sin(\theta_7 + \alpha_1) + d_7 \sin\theta_6 \tag{E.7}$$

$$(Z_U - Z_T) = -d_7 \cos(\theta_7 + \alpha_1) - d_7 \cos\theta_6 \tag{E.8}$$

$$\tag{E.9}$$

$$(X_C - X_L) = -\sqrt{(d_{14})^2 + (d_3)^2} \cdot \cos(\theta_1 + atan2(d_3, d_{14})) + \\ \sqrt{(d_{15})^2 + (d_{18} + d_{19} + d_{20})^2} \cdot \cos(\theta_1 + atan2(d_{18} + d_{19} + d_{20}, d_{15})) + d_8 \sin(\theta_4 + \alpha_2) \tag{E.10}$$

$$(Z_C - Z_L) = -\sqrt{(d_{14})^2 + (d_3)^2} \cdot \sin(\theta_1 + atan2(d_3, d_{14})) + \\ \sqrt{(d_{15})^2 + (d_{18} + d_{19} + d_{20})^2} \cdot \sin(\theta_1 + atan2(d_{18} + d_{19} + d_{20}, d_{15})) - d_8 \cos(\theta_4 + \alpha_2) \tag{E.11}$$

$$(X_Z - X_N) = -\sqrt{(d_{22})^2 + (d_{21})^2} \cdot \cos(\theta_1 + atan2(d_{21}, d_{22})) + \\ \sqrt{(d_1 + d_{17} + d_{16} + d_{15} + d_{14})^2 + (d_3 + d_{18})^2} \cdot \cos(\theta_1 + \\ atan2(d_3 + d_{18}, d_1 + d_{17} + d_{16} + d_{15} + d_{14})) \\ \sqrt{(d_2)^2 + (d_4 + d_{19} + d_{20})^2} \cdot \cos(\theta_1 + atan2(d_4 + d_{19} + d_{20}, d_2)) + d_{10} \sin\theta_5 \tag{E.12}$$

$$
\begin{aligned}
(Z_Z - Z_N) = -\sqrt{(d_{22})^2 + (d_{21})^2} \cdot \sin\left(\theta_1 + atan2(d_{21}, d_{22})\right) + \\
\sqrt{(d_1 + d_{17} + d_{16} + d_{15} + d_{14})^2 + (d_3 + d_{18})^2} \cdot \sin\left(\theta_1 + \right. \\
\left. atan2(d_3 + d_{18}, d_1 + d_{17} + d_{16} + d_{15} + d_{14})\right) \\
\sqrt{(d_2)^2 + (d_4 + d_{19} + d_{20})^2} \cdot \sin(\theta_1 + atan2(d_4 + d_{19} + d_{20}, d_2)) - d_{10} \cos\theta_5
\end{aligned}
\tag{E.13}
$$

where the four-quadrant inverse tangent is indicated by atan2.

$$\beta_1 = atan2(Z_H - Z_J, X_H - X_J) \tag{E.14}$$

$$\beta_4 = atan2(Z_U - Z_T, X_U - X_T) \tag{E.15}$$

$$\beta_2 = atan2(Z_C - Z_L, X_C - X_L) \tag{E.16}$$

$$\beta_3 = atan2(Z_Z - Z_N, X_Z - X_N) \tag{E.17}$$

References

[1] J. Green, J. Clounie, R. Galarza, S. Anderson, J. Campell-Smith, R. C. Voicu, Optimization of an intelligent wheelchair: Lidar and camera vision for obstacle avoidance, in: 2022 22nd International Conference on Control, Automation and Systems (ICCAS), 2022, pp. 313–318. doi:10.23919/ICCAS55662.2022.10003851.

[2] H. Kaye, T. Kang, M. Laplante, Mobility device use in the united states (01 2000).

[3] N. C. for Health Statistics, Percentage of any difficulty walking or climbing steps for adults aged 18 and over, in: National Health Interview Survey, 2022.

[4] C. Di Priamo, L'inclusione scolastica: Accessibilità, qualità dell'offerta e caratteristiche degli alunni con sostegno, Report Istituto Nazionale di Statistica Istat (Italian) (2020).

[5] L. Bruzzone, G. Quaglia, Review article: locomotion systems for ground mobile robots in unstructured environments, Mechanical Sciences 3 (2012) 49–62. doi:10.5194/ms-3-49-2012.

[6] G. Reina, M. Foglia, On the mobility of all-terrain rovers, Industrial Robot: An International Journal 40 (2013) 5–5. doi:10.1108/01439911311297720.

[7] R. Bogue, Climbing robots: recent research and emerging applications, Industrial Robot (2019).

[8] P. Chatterjee, N. Lahiri, A. Bhattacharjee, A. Chakraborty, Automated hybrid stair climber for physically challenged people, in: 2021 5th International Conference on Electronics, Materials Engineering Nano-Technology (IEMENTech), 2021, pp. 1–4. doi:10.1109/IEMENTech53263.2021.9614713.

[9] J. N. J. Science, T. Agency), Stories that change the world: Amoeba energy (amoeba-inspired technlogies to change the mobility), JST (2020).

[10] W. Tao, J. Xu, T. Liu, Electric-powered wheelchair with stair-climbing ability, International Journal of Advanced Robotic Systems 14 (2017) 172988141772143. doi:10.1177/1729881417721436.

[11] R. Riener, The cybathlon promotes the development of assistive technology for people with physical disabilities, Journal of NeuroEngineering and Rehabilitation 13 (12 2016). `doi:10.1186/s12984-016-0157-2`.

[12] J. Lee, W. Jeong, J. Han, T. Kim, S. Oh, Barrier-free wheelchair with a mechanical transmission, Applied Sciences 11 (11) (2021). `doi:10.3390/app11115280`.
URL `https://www.mdpi.com/2076-3417/11/11/5280`

[13] W. TAO, Y. JIA, T. LIU, J. YI, H. WANG, Y. INOUE, A novel wheel-track hybrid electric powered wheelchair for stairs climbing, Journal of Advanced Mechanical Design, Systems, and Manufacturing 10 (4) (2016) JAMDSM0060–JAMDSM0060. `doi:10.1299/jamdsm.2016jamdsm0060`.

[14] F. Martínez, J.A.G.; Cardinale, Robotics in Neurosurgery: Principles and Practice, Springer, 2022.

[15] J. Podobnik, J. Rejc, S. Slajpah, M. Munih, M. Mihelj, All-terrain wheelchair: Increasing personal mobility with a powered wheel-track hybrid wheelchair, IEEE Robotics Automation Magazine 24 (4) (2017) 26–36. `doi:10.1109/MRA.2017.2746182`.

[16] J. Wang, T. Wang, C. Yao, X. Li, C. Wu, Active tension control for wt wheelchair robot by using a novel control law for holonomic or nonholonomic systems, Mathematical Problems in Engineering 2013 (01 2013). `doi:10.1155/2013/236515`.

[17] S. Nakajima, S. Sawada, Methodology of climbing and descending stairs for four-wheeled vehicles, in: 2020 IEEE 23rd International Conference on Intelligent Transportation Systems (ITSC), 2020, pp. 1–6. `doi:10.1109/ITSC45102.2020.9294695`.

[18] J. Meyer, S. Weber, L. Jäger, R. Sigrist, R. Gassert, O. Lambercy, A survey on the influence of cybathlon on the development and acceptance of advanced assistive technologies, Journal of NeuroEngineering and Rehabilitation 19 (04 2022). `doi:10.1186/s12984-022-01015-5`.

[19] M. Popovic, Biomechatronics, Elsevier Science: Amsterdam (2019).

[20] S. Yu, T. Wang, Z. Wang, Y. Wang, C. Yao, X. Li, Original design of a wheelchair robot equipped with variable geometry single tracked mechanisms, Int. J. Robotics Autom. 30 (2015).
URL `https://api.semanticscholar.org/CorpusID:11945401`

[21] Y. Onozuka, N. Tomokuni, G. Murata, M. Shino, Dynamic stability control of inverted-pendulum-type robotic wheelchair for going up and down stairs, in: 2020 IEEE/RSJ International Conference on Intelligent Robots and Systems (IROS), 2020, pp. 4114–4119. `doi:10.1109/IROS45743.2020.9341242`.

[22] G. Quaglia, M. Nisi, Design of a self-leveling cam mechanism for a stair climbing wheelchair, Mechanism and Machine Theory 112 (2017) 84–104. doi:10.1016/j.mechmachtheory.2017.02.003.

[23] B. D. Castillo, Y.-F. Kuo, J. J. Chou, Novel design of a wheelchair with stair climbing capabilities, 2015 International Conference on Intelligent Informatics and Biomedical Sciences (ICIIBMS) (2015) 208–215.
URL https://api.semanticscholar.org/CorpusID:15119734

[24] H. Uustal, J. Minkel, Study of the independence ibot 3000 mobility system: An innovative power mobility device, during use in community environments, Archives of physical medicine and rehabilitation 85 (2005) 2002–10. doi:10.1016/j.apmr.2004.04.044.

[25] G. Quaglia, W. Franco, R. Oderio, Wheelchair.q, a motorized wheelchair with stair climbing ability, Mechanism and Machine Theory 46 (11) (2011) 1601–1609. doi:https://doi.org/10.1016/j.mechmachtheory.2011.07.005.
URL https://www.sciencedirect.com/science/article/pii/S0094114X1100139X

[26] H. Wang, L. He, Q. Li, W. Zhang, D. Zhang, P. Xu, Research on a kind of leg-wheel stair-climbing wheelchair, 2014, pp. 2101–2105. doi:10.1109/ICMA.2014.6886028.

[27] J. Yuan, S. Hirose, Research on leg-wheel hybrid stair-climbing robot, zero carrier, in: 2004 IEEE International Conference on Robotics and Biomimetics, 2004, pp. 654–659. doi:10.1109/ROBIO.2004.1521858.

[28] J. Yuan, S. Hirose, Zero carrier: A novel eight leg-wheels hybrid stair climbing mobile vehicle, Journal of Robotics and Mechatronics 17 (2005) 44–51.

[29] C.-H. Lee, K.-m. Lee, J. Yoo, I.-s. Kim, Y.-B. Bang, A compact stair-climbing wheelchair with two 3-dof legs and a 1-dof base, Industrial Robot: An International Journal 43 (2016) 181–192. doi:10.1108/IR-05-2015-0085.

[30] C. Xi, Z. Qun-fei, M. Pei-sun, Humanoid robot 3-d motion simulation for hardware realization 24 (2007) 713–717+722.

[31] J. Tang, Q. Zhao, J. Huang, Application of “human-in-the-loop” control to a biped walking-chair robot, in: 2007 IEEE International Conference on Systems, Man and Cybernetics, 2007, pp. 2431–2436. doi:10.1109/ICSMC.2007.4413944.

[32] Y. Sugahara, K. Hashimoto, H. Sunazuka, M. Kawase, A. Ohta, C. Tanaka, H. ok Lim, A. Takanishi, Towards the biped walking wheelchair, The First IEEE/RAS-EMBS International Conference on Biomedical Robotics and Biomechatronics, 2006. BioRob 2006. (2006) 781–786.
URL https://api.semanticscholar.org/CorpusID:17641071

[33] C.-Y. Zheng, Z. Qunfei, P.-S. Ma, H.-Q. Zhang, Z. Gou, Mechanism design of a biped walking-chair robot 28 (2006) 297–302.

[34] C.-T. Chen, H.-V. Pham, Design and fabrication of a statically stable stair-climbing robotic wheelchair, Industrial Robot: An International Journal 36 (2009) 562–569. doi:10.1108/01439910910994632.

[35] Y. Sugahara, N. Yonezawa, K. Kosuge, A novel stair-climbing wheelchair with transformable wheeled four-bar linkages, in: 2010 IEEE/RSJ International Conference on Intelligent Robots and Systems, 2010, pp. 3333–3339. doi:10.1109/IROS.2010.5648906.

[36] J. A. Chocoteco, R. Morales, V. Feliu-Batlle, Enhancing the trajectory generation of a stair-climbing mobility system, Sensors 17 (11) (2017). doi:10.3390/s17112608.
URL https://www.mdpi.com/1424-8220/17/11/2608

[37] M. Lawn, T. Ishimatsu, Modeling of a stair-climbing wheelchair mechanism with high single-step capability, IEEE Transactions on Neural Systems and Rehabilitation Engineering 11 (3) (2003) 323–332. doi:10.1109/TNSRE.2003.816875.

[38] S. Nakajima, Stair-climbing gait for a four-wheeled vehicle, ROBOMECH Journal 7 (04 2020). doi:10.1186/s40648-020-00168-z.

[39] S. Nakajima, Evaluation of the mobility performance of a personal mobility vehicle for steps, IEEE Access 5 (2017) 9748–9756. doi:10.1109/ACCESS.2017.2700323.

[40] S. Nakajima, Rt-mover: A rough terrain mobile robot with a simple leg-wheel hybrid mechanism, I. J. Robotic Res. 30 (2011) 1609–1626. doi:10.1177/0278364911405697.

[41] Y. Uchida, K. Furuichi, S. Hirose, Fundamental performance of a 6 wheeled off-road vehicle "helios-v", in: Proceedings 1999 IEEE International Conference on Robotics and Automation (Cat. No.99CH36288C), Vol. 3, 1999, pp. 2336–2341 vol.3. doi:10.1109/ROBOT.1999.770454.

[42] K. Yoneda, Development of a hi-grip stair climbing crawler with hysteresis compliant blocks, in: Proc. 4th Int. Conf. on Climbing and Walking Robots and the Support Technologies for Mobile Machines, Madrid, 2004, 2004, pp. 569–576.

[43] S. Hirose, E. Fukushima, R. Damoto, H. Nakamoto, Design of terrain adaptive versatile crawler vehicle helios-vi, in: Proceedings 2001 IEEE/RSJ International Conference on Intelligent Robots and Systems. Expanding the Societal Role of Robotics in the the Next Millennium (Cat. No.01CH37180), Vol. 3, 2001, pp. 1540–1545 vol.3. doi:10.1109/IROS.2001.977198.

[44] S. Hirose, T. Sensu, The taqt carrier: A practical terrain adaptive quadru-track carrier robot, in: Proceedings of the IEEE/RSJ International Conference on Intelligent Robots and Systems, Vol. 3, 1992, pp. 2068–2073. doi:10.1109/IROS.1992.601941.

[45] S. R. Thamel, R. Munasinghe, T. Lalitharatne, Motion planning of novel stair-climbing wheelchair for elderly and disabled people, in: 2020 Moratuwa Engineering Research Conference (MERCon), 2020, pp. 590–595. doi:10.1109/MERCon50084.2020.9185273.

[46] B. Ur rehman, D. CALDWELL, C. Semini, Centaur robots - a survey, 2017, pp. 247–258. doi:10.1142/9789813231047_0032.

[47] A. Ugenti, R. Galati, G. Mantriota, G. Reina, Analysis of an all-terrain tracked robot with innovative suspension system, Mechanism and Machine Theory 182 (2023) 105237. doi:https://doi.org/10.1016/j.mechmachtheory.2023.105237.
URL https://www.sciencedirect.com/science/article/pii/S0094114X23000113

[48] A. Ghosal, Part special issue: 13th national conference on machines and mechanisms (nacomm). selected papers based on the presentations at the conference, bangalore, india, december 12–13, 2007, Mechanism and Machine Theory 2 (01 2010).

[49] H. Wen, H. Yang, Y. Chen, L. Zhou, D. Wu, A robot with decoupled mechanical structure and adapted state machine control for both ground and staircase situations, Applied Sciences 9 (23) (2019). doi:10.3390/app9235185.
URL https://www.mdpi.com/2076-3417/9/23/5185

[50] T. Okada, W. Botelho, T. Shimizu, Motion analysis with experimental verification of the hybrid robot peopler-ii for reversible switch between walk and roll on demand, I. J. Robotic Res. 29 (2010) 1199–1221. doi:10.1177/0278364909348762.

[51] T. Okada, A. Mahmoud, W. Botelho, T. Shimizu, Trajectory estimation of a skid-steering mobile robot propelled by independently driven wheels, Robotica 30 (2012) 123 – 132. doi:10.1017/S026357471100035X.

[52] S. A. A. Moosavian, H. Semsarilar, A. Kalantari, Design and manufacturing of a mobile rescue robot, in: 2006 IEEE/RSJ International Conference on Intelligent Robots and Systems, 2006, pp. 3982–3987. doi:10.1109/IROS.2006.281835.

[53] V. Mostýn, V. Krys, T. Kot, Z. Bobovský, P. Novak, The synthesis of a segmented stair-climbing wheel, International Journal of Advanced Robotic Systems 15 (2018) 172988141774947. doi:10.1177/1729881417749470.

[54] A. Pappalettera, F. Bottiglione, G. Mantriota, G. Reina, Watch the next step: A comprehensive survey of stair-climbing vehicles, Robotics 12 (3) (2023). doi:10.3390/robotics12030074.
URL https://www.mdpi.com/2218-6581/12/3/74

[55] M. B. Binnard, Design of a small pneumatic walking robot, Ph.D. thesis, Massachusetts Institute of Technology, Dept. of Mechanical Engineering (1995).

[56] D. Lu, E. Dong, C. Liu, M. Xu, J. Yang, Design and development of a leg-wheel hybrid robot "hytro-i", in: 2013 IEEE/RSJ International Conference on Intelligent Robots and Systems, 2013, pp. 6031–6036. doi:10.1109/IROS.2013.6697232.

[57] G. Dudek, M. Jenkin, Computational principles of mobile robotics., 2000.

[58] S. Tarkowski, A. Nieoczym, J. Caban, P. Jilek, M. Sejkorová, The analysis of pneumatic wheel rim deformation while hitting an obstacle, Applied Sciences 12 (13) (2022). doi:10.3390/app12136371.
URL https://www.mdpi.com/2076-3417/12/13/6371

[59] J.-Y. Wong, A. Reece, Prediction of rigid wheel performance based on the analysis of soil-wheel stresses: Part ii. performance of towed rigid wheels, Journal of Terramechanics 4 (2) (1967) 7–25. doi:https://doi.org/10.1016/0022-4898(67)90047-X.
URL https://www.sciencedirect.com/science/article/pii/002248986790047X

[60] G. Thomas, V. Vantsevich, Wheel-terrain-obstacle interaction in vehicle mobility analysis, Vehicle System Dynamics - VEH SYST DYN 48 (2010) 139–156. doi:10.1080/00423111003690496.

[61] W. Wang, H. Xu, X. Xu, F. Zhou, Enhancing the passing ability of unmanned vehicles using a variable-wheelbase driving system, IEEE Access 7 (2019) 115871–115885. doi:10.1109/ACCESS.2019.2936268.

[62] W.-H. Wang, X.-J. Xu, H.-J. Xu, C.-L. Sun, Development of variable-configuration wheeled driving system for enhancing the obstacle-crossing ability of unmanned vehicles, Proceedings of the Institution of Mechanical Engineers, Part C: Journal of Mechanical Engineering Science 235 (9) (2021) 1645–1659. arXiv:https://doi.org/10.1177/0954406220951600, doi:10.1177/0954406220951600.
URL https://doi.org/10.1177/0954406220951600

[63] Y. Uchida, K. Furuichi, S. Hirose, Evaluation of wheel performance on rough terrain and development of hs wheel., Journal of the Robotics Society of Japan 18 (2000) 743–751. doi:10.7210/jrsj.18.743.

[64] G. M. Rocco Galati, Antonio Pappalettera, G. Reina, Rubber tracks and tyres: a detailed insight into force analysis during obstacle negotiation, Vehicle System Dynamics 0 (0) (2024) 1–18. `arXiv:https://doi.org/10.1080/00423114.2024.2366528`, `doi:10.1080/00423114.2024.2366528`.
URL `https://doi.org/10.1080/00423114.2024.2366528`

[65] A. Pappalettera, R. Galati, G. Mantriota, G. Reina, Step-obstacle negotiation: A contact force analysis, in: G. Quaglia, G. Boschetti, G. Carbone (Eds.), Advances in Italian Mechanism Science, Springer Nature Switzerland, Cham, 2024, pp. 206–213.

[66] H. B. Pacejka, E. Bakker, The magic formula tyre model, Vehicle System Dynamics 21 (sup001) (1992) 1–18. `arXiv:https://doi.org/10.1080/00423119208969994`, `doi:10.1080/00423119208969994`.
URL `https://doi.org/10.1080/00423119208969994`

[67] A. Gasmi, P. F. Joseph, T. B. Rhyne, S. M. Cron, Development of a two-dimensional model of a compliant non-pneumatic tire, International Journal of Solids and Structures 49 (13) (2012) 1723–1740. `doi:https://doi.org/10.1016/j.ijsolstr.2012.03.007`.
URL `https://www.sciencedirect.com/science/article/pii/S0020768312000960`

[68] X. Jin, C. Hou, X. Fan, Y. Sun, J. Lv, C. Lu, Investigation on the static and dynamic behaviors of non-pneumatic tires with honeycomb spokes, Composite Structures 187 (2018) 27 – 35, cited by: 86. `doi:10.1016/j.compstruct.2017.12.044`.
URL `https://www.scopus.com/inward/record.uri?eid=2-s2.0-85038843268&doi=10.1016%2fj.compstruct.2017.12.044&partnerID=40&md5=0984daf40c7912a1d83857aafa4fdade`

[69] O. Belluzzi, Scienza delle costruzioni vol. 2 (1963).

[70] A. Gasmi, P. F. Joseph, T. B. Rhyne, S. M. Cron, Closed-form solution of a shear deformable, extensional ring in contact between two rigid surfaces, International Journal of Solids and Structures 48 (5) (2011) 843–853. `doi:https://doi.org/10.1016/j.ijsolstr.2010.11.018`.

[71] Y. Xiong, A. Tuononen, The in-plane deformation of a tire carcass: Analysis and measurement, Case studies in mechanical systems and signal processing 2 (10 2015). `doi:10.1016/j.csmssp.2015.09.001`.

[72] D. Garcia-Pozuelo, O. Olatunbosun, J. Yunta, X. Yang, V. Diaz, A novel strain-based method to estimate tire conditions using fuzzy logic for intelligent tires, Sensors 17 (2) (2017). `doi:10.3390/s17020350`.
URL `https://www.mdpi.com/1424-8220/17/2/350`

[73] D. Kim, H. Hong, H. S. Kim, J. Kim, Optimal design and kinetic analysis of a stair-climbing mobile robot with rocker-bogie mechanism, Mechanism and Machine Theory 50 (2012) 90–108. `doi:https://doi.org/10.1016/j.mechmachtheory.2011.11.013`.
URL `https://www.sciencedirect.com/science/article/pii/S0094114X1100231X`

[74] L. Bruzzone, S. E. Nodehi, P. Fanghella, Tracked locomotion systems for ground mobile robots: A review, Machines 10 (8) (2022). `doi:10.3390/machines10080648`.
URL `https://www.mdpi.com/2075-1702/10/8/648`

[75] W. Lee, S. Kang, M. Kim, M. Park, Robhaz-dt3: teleoperated mobile platform with passively adaptive double-track for hazardous environment applications, in: 2004 IEEE/RSJ International Conference on Intelligent Robots and Systems (IROS) (IEEE Cat. No.04CH37566), Vol. 1, 2004, pp. 33–38 vol.1. `doi:10.1109/IROS.2004.1389325`.

[76] S. A. A. Moosavian, H. Semsarilar, A. Kalantari, Design and manufacturing of a mobile rescue robot, in: 2006 IEEE/RSJ International Conference on Intelligent Robots and Systems, 2006, pp. 3982–3987. `doi:10.1109/IROS.2006.281835`.

[77] Q.-H. Vu, B.-S. Kim, J.-B. Song, Autonomous stair climbing algorithm for a small four-tracked robot, in: 2008 International Conference on Control, Automation and Systems, 2008, pp. 2356–2360. `doi:10.1109/ICCAS.2008.4694199`.

[78] M. Hutter, C. Gehring, D. Jud, A. Lauber, C. D. Bellicoso, V. Tsounis, J. Hwangbo, K. Bodie, P. Fankhauser, M. Bloesch, R. Diethelm, S. Bachmann, A. Melzer, M. Hoepflinger, Anymal - a highly mobile and dynamic quadrupedal robot, in: 2016 IEEE/RSJ International Conference on Intelligent Robots and Systems (IROS), 2016, pp. 38–44. `doi:10.1109/IROS.2016.7758092`.

[79] E. Moore, D. Campbell, F. Grimminger, M. Buehler, Reliable stair climbing in the simple hexapod 'rhex', in: Proceedings 2002 IEEE International Conference on Robotics and Automation (Cat. No.02CH37292), Vol. 3, 2002, pp. 2222–2227 vol.3. `doi:10.1109/ROBOT.2002.1013562`.

[80] A. Ugenti, F. Vulpi, R. Domínguez, F. Cordes, A. Milella, G. Reina, On the role of feature and signal selection for terrain learning in planetary exploration robots, Journal of Field Robotics 39 (4) (2022) 355–370.

[81] G. Quaglia, L. G. Butera, E. Chiapello, L. Bruzzone, Ugv epi.q-mod, in: M. Ceccarelli, V. A. Glazunov (Eds.), Advances on Theory and Practice of Robots and Manipulators, Springer International Publishing, Cham, 2014, pp. 331–339.

[82] V. Klemm, A. Morra, C. Salzmann, F. Tschopp, K. Bodie, L. Gulich, N. Küng, D. Mannhart, C. Pfister, M. Vierneisel, F. Weber, R. Deuber, R. Y. Siegwart, Ascento: A two-wheeled jumping robot, 2019 International Conference on Robotics and Automation (ICRA) (2019) 7515–7521.
URL `https://api.semanticscholar.org/CorpusID:199401923`

[83] S. Hirose, Y. Fukuda, K. Yoneda, A. Nagakubo, H. Tsukagoshi, K. Arikawa, G. Endo, T. Doi, R. Hodoshima, Quadruped walking robots at tokyo institute of technology, IEEE Robotics Automation Magazine 16 (2) (2009) 104–114. `doi:10.1109/MRA.2009.932524`.

[84] L. Bruzzone, M. Baggetta, S. E. Nodehi, P. Bilancia, P. Fanghella, Functional design of a hybrid leg-wheel-track ground mobile robot, Machines 9 (1) (2021). `doi:10.3390/machines9010010`.
URL `https://www.mdpi.com/2075-1702/9/1/10`

[85] Y. Li, M. Li, H. Zhu, E. Hu, C. Tang, P. Li, S. You, Development and applications of rescue robots for explosion accidents in coal mines, Journal of Field Robotics 37 (11 2019). `doi:10.1002/rob.21920`.

[86] B. Sun, X. Jing, A tracked robot with novel bio-inspired passive “legs”, Robotics and Biomimetics 4 (2017) 18. `doi:10.1186/s40638-017-0070-6`.

[87] A. Ugenti, R. Galati, G. Mantriota, G. Reina, Analysis of an all-terrain tracked robot with innovative suspension system, Mechanism and Machine Theory 182 (2023) 105237. `doi:https://doi.org/10.1016/j.mechmachtheory.2023.105237`.
URL `https://www.sciencedirect.com/science/article/pii/S0094114X23000113`